Photonic packaging enabled by three-dimensional micro-printing

Zur Erlangung des akademischen Grades eines

DOKTORS DER INGENIEURWISSENSCHAFTEN (Dr.-Ing.)

von der KIT-Fakultät für Elektrotechnik und Informationstechnik des
Karlsruher Instituts für Technologie (KIT)

genehmigte

Dissertation

von

Matthias Jan Blaicher, M.Sc.

geboren in Karlsruhe, Deutschland

Tag der mündlichen Prüfung: 28.07.2021

Hauptreferent: Prof. Dr.-Ing. Christian Koos
Korreferenten: Prof. Dr. Carsten Rockstuhl
Prof. Dr.-Ing. Dr. h. c. Wolfgang Freude

Contents

Kurzfassung

Seit der Erfindung der elektronischen integrierten Schaltung durch Jack Kilby und Robert Noyce im Jahr 1958 ist mehr als ein halbes Jahrhundert vergangen und "kleiner, schneller, günstiger" ist bis heute das Leitprinzip der weltweiten Halbleiterindustrie. Dieser Siegeszug der Elektronik hat eine Vielzahl von Geräten wie zum Beispiel Smartphones, Computer, Internet und viele weitere Produkte ermöglicht, welche nunmehr dauerhaft Einzug in unser Leben gehalten haben und es damit nachhaltig prägen. All diesen Produkten ist gemein, dass sie vor einem halben Jahrhundert noch fast durchweg als Science-Fiction wahrgenommen worden wären.

Die meisten dieser Geräte kommunizieren heute ununterbrochen untereinander über das Internet, so dass der weltweite Datenverkehr unaufhörlich mit einer durchschnittlichen jährlichen Wachstumsrate von 26 % ansteigt. Es wird erwartet, dass im Jahr 2022 bis zu 4,8 Zettabytes an Daten innerhalb eines Jahres übertragen werden [1]. Die optische Nachrichtentechnik ist die technische Grundlage für die Übertragung dieser enormen Datenmengen. Da die überwiegende Mehrheit dieser Daten jedoch entweder in elektronischer Form erzeugt oder in dieser Form verarbeitet wird, ist die effiziente elektro-optische Wandlung ein bedeutender Forschungsbereich.

Besonders vielversprechend sind hier insbesondere photonische integrierte Schaltungen (eng. photonic integrated circuits, PIC). Diese werden unter Verwendung bewährter Fertigungstechnologien hergestellt, wie sie auch zur Herstellung elektronischer Chips genutzt werden. Dabei ist die Silizium-Photonik (SiP) von besonderem Interesse, da sie eine erprobte Fertigungstechnologie nutzt, welche auch zur Herstellung elektronischer Chips zum Einsatz kommt. Allerdings verhindert der indirekte Bandübergang von Silizium eine effiziente Erzeugung von Licht in-

nerhalb eines SiP-PIC. Zur Überwindung dieser Einschränkung kommen häufig III-V-Verbindungshalbleiter als Lichtquellen zum Einsatz, welche dann mit dem SiP-Chip kombiniert werden müssen. Eine Kombination solcher Halbleiterlaser mit SiP-Chips, wie sie beispielsweise zur Herstellung eines Sendermoduls in Verbindung mit Si-Modulatoren notwendig ist, gestaltet sich jedoch schwierig. Die hierzu notwendige photonische Integration verschiedener Materialplattformen erhöht jedoch die Gesamtkosten solch eines Moduls drastisch und negiert weitestgehend die kosteneffiziente parallele Herstellung der zugrundeliegenden Chips auf einem gemeinsame Wafer.

Im Rahmen dieser Dissertation werden solche planare integrierte Schaltungen in vielfältiger Weise durch dreidimensionale (3D) Mikrostrukturen erweitert, welche mit Hilfe additiver Mehr-Photonen-Lithographie gefertigt werden. Dazu gehören 3D-gedruckte dielektrische Wellenleiter, welche häufig als photonische Wirebonds (PWB) bezeichnet werden, und die eine praktikable Lösung für die Herausforderungen des photonischen Aufbau- und Verbindungstechnik darstellen. Insbesondere wird in dieser Arbeit zum ersten Mal die zuverlässige Herstellung solcher PWB mit minimalen Einfügeverlusten demonstriert und deren Beständigkeit gegenüber rauen Umgebungsbedingungen aufgezeigt. Darüber hinaus werden komplexe Multi-Chip-Sendermodule realisiert, welche durch die Nutzung mehrerer Datenkanäle rekordhohe Datenraten erreichen. Des Weiteren werden zwei neuartige dreidimensional gedruckte photonische Mikrostrukturen demonstriert: Die erste Struktur dient als breitbandiger Polarisationsstrahlteiler mit integrierten Polarisationsdrehern, während es die zweite Struktur ermöglicht, effizient und breitbandig Licht senkrecht zwischen der Bauteileebene eines PIC und einer Einmodenfaser zu koppeln.

In den folgenden Kapiteln dieser Arbeit werden folgende Themen behandelt:

Kapitel 1 gibt eine kurze Einführung in die Mehr-Photonen-Lithographie und erläutert, wie sich diese zur Herstellung von photonischen Wirebonds in photonischen Multi-Chip-Assemblies nutzen lässt.

Kapitel 2 legt die theoretischen und technologischen Grundlagen für die nachfolgenden Kapitel und befasst sich tiefer mit der Mehr-Photonen-Lithographie, mit photonischen Wirebonds, sowie mit Mikrolinsen und deren Simulation.

Kapitel 3 demonstriert den Aufbau von optischen Sendersystemen, die als Multi-Chip-Module mit Hilfe von *in situ* gedruckte photonischen Wirebonds realisiert wurden. Des Weiteren wird die Beständigkeit von photonischen Wirebonds unter thermischen Einflüssen und unter der Einwirkung von Feuchtigkeit demonstriert. Diese Beständigkeit wird durch eine permanente Ummantelung mit einem niedrig-brechenden Kunststoff erreicht.

Kapitel 4 beschreibt einen neuartigen breitbandigen Polarisationsstrahlteiler mit integrierten Polarisationsdrehern, der auf hochgradig doppelbrechenden drei-dimensionalen Wellenleitern basiert.

Kapitel 5 beschreibt eine neuartige Struktur für die breitbandige Kopplung zwischen optischen Fasern und integrierten photonischen Chips. Die Struktur basiert auf einem photonische Wirebond, welcher an einer Seite mit einem integrierten photonischen Chip verbunden ist und an der anderen Seite mit einer Mikrolinse versehen wurde. Sowohl der photonische Wirebond als auch die Mikrolinse werden dabei gemeinsam in einem lithographischen Schritt hergestellt.

Kapitel 6 gibt eine Zusammenfassung der Arbeiten in dieser Dissertation und skizziert mögliche zukünftige Weiterentwicklungen des photonischen Wirebondprozesses und dessen Anwendung.

Preface

It has been more than half a century since the invention of the electronic integrated circuit by Jack Kilby and Robert Noyce in 1958, and 'smaller, faster, cheaper' has been the guiding principle of the whole semiconductor industry ever since. This rise of electronics has enabled an enormous variety of devices to enter and to shape our lives, among them are smartphones, computers, the internet and many more - nearly all of which would have been considered science fiction only half a century ago.

Today, many of these devices constantly communicate with one another over the internet, giving rise to an exponential growth of data traffic. In fact, the global internet traffic is growing at a compound annual growth rate of 26 %, and it is expected to reach 4.8 zettabytes per year by 2022 [1]. Optical data communication provides the technological foundation to transmit these vast amounts of data. However, as most of these data either originate or are used in electronic form, electro-optical conversion is required, and is therefore an important area of research.

A possible solution is the integration of electro-optic converters in photonic integrated circuits (PIC), which can be considered as the optical equivalent to electronic integrated circuits. They can be fabricated using technologies pioneered for the fabrication of electronic integrated chips. In particular, silicon photonics (SiP) utilizes the mature complementary metal-oxide-semiconductor (CMOS) technology to fabricate highly compact PIC. Unfortunately, the indirect bandgap of silicon prevents the efficient generation of light, because a phonon interaction is required for the emission of a photon via a transition of an electron from the valence to the conduction band. To overcome this limitation, direct III-V compound semiconductors are often used as light sources in photonics. It is, however, difficult to combine

such light sources with SiP chips, to realize for example a transmitter module using Si modulators [2]. Photonic integration of multiple material platforms drastically increases the overall module costs and mostly counteracts the efficiency of wafer-scale fabrication.

In the framework of this dissertation, multi-photon lithography (MPL) is used to extend such planar PIC devices by additive manufacturing of three-dimensional (3D) photonic micro-structures in a wide variety of ways. Among these are 3D printed dielectric waveguides, commonly referred to as photonic wire bonds (PWB). Such PWB are an attractive solution to overcome the challenge of photonic packaging in practice. It is shown that PWB can be reliably fabricated with minimal loss, and they withstand harsh environmental conditions when encased in cladding material. The photonic wire bonding technique is used to realize advanced multi-chip modules that combine the advantages of different photonic integration platforms. In particular, multi-chip transmitter modules are realized using multiple data channels, each one transported on an independent optical fibre, and transmitting data at record high data rates. In addition, two novel 3D printed photonic microstructure are demonstrated: One structure can be used as a broadband polarization beam splitter with integrated polarization rotators, while the other structure supplies photonic chips with an efficient method that enables broadband and out-of-plane optical coupling between PIC and single-mode fibres.

The individual chapters of this work cover the following subjects:

Chapter 1 gives a short introduction to multi-photon lithography and its use in fabricating photonic wire bonds to enable photonic multi-chip modules.

Chapter 2 lays the theoretical and technological foundation for the subsequent chapters by introducing multi-photon lithography and its use in the fabrication of photonic wire bonds and micro-lenses.

Chapter 3 demonstrates multi-chip transmitter assemblies enabled by *in situ* printing of photonic wire bonds. For the first time, these photonic wire bonds are permanently over-clad with a low-refractive index material which provides permanent protection against environmental influences. This is verified in experiments exposing the PWB to harsh environmental conditions.

Chapter 4 describes a novel broadband polarization beam splitter with integrated polarization rotators based on highly birefringent 3D freeform waveguides.

Chapter 5 describes a new structure for broadband out-of-plane coupling between an optical fibre and an integrated photonic chip. The structure is based on a PWB which is attached to an integrated photonic chip on one side, and to a micro-lens on the other side. The photonic wire bond and the micro-lens are printed in the same lithography step.

Chapter 6 summarizes the work in this thesis and outlines further research directions on the photonic wire bonding technique to serve future applications.

Achievements of the present work

In this thesis, the concept of photonic wire bonds (PWB) is systematically advanced from a proof-of-principle level [3, 4] to fully automated printing of reliable chip-chip and fiber-chip connections for advanced multi-chip modules [5] that combine the advantages of different photonic integration platforms. Using specially developed software and dedicated lithography hardware, complex multi-chip transmitter modules and other novel photonic devices, such as 3D printed out-of-plane couplers [6] and polarization beam splitters with integrated rotators [7], are demonstrated.

A concise overview of the major achievements is given in the following list:

Demonstration of a fast multi-photon lithography machine with advanced alignment procedures: A multi-photon lithography machine employing fast galvanometric scanners is built. It includes fluorescence and confocal measurement channels which are used to automatically fabricate photonic wire bonds and micro-lenses attached to the facets of integrated optical chips with an estimated alignment accuracy of 100 nm relative to dedicated features or even directly relative to the optical waveguide an of an integrated photonic chip, see Sections 2.2 and Appendix D.2 for details on the hardware and system design. This technology was employed in the journal publications [J7] and [J17].

Of particular importance was the automated and reliable fabrication of optical components on the facet of optical fibres and fibre arrays. Their 3D models were aligned to the fibre core in position and orientation. This has proven to be an enabling technology with a wide range of applications. Among others, it has been demonstrated with great success in the journal contributions [J3], [J4], [J5] , [J9], [J17], and [J18].

First demonstration of multi-chip modules using PWB: Two distinct multi-chip transmitter modules are realized, combining efficient light sources based on indium phosphide (InP) with silicon photonic devices and standard single-mode fibres. In a first set of experiments, an eight-channel transmitter is realized, offering an aggregate line rate of $448\,\text{Gbit s}^{-1}$ by low-complexity intensity modulation. In a second set of experiment, a four-channel coherent transmitter is demonstrated, operating at a net data rate of $732.7\,\text{Gbit s}^{-1}$ – a record for coherent silicon photonic transmitters with co-packaged lasers, see Sections 3.3.2 and 3.3.3 of journal publication [J7] for details. Note that the achievements of this work resulted from equal contributions by the author of the thesis and M. Billah. The author's work was mainly focused on the fabrication technology and design of the photonic wire bonds, while the work of M. Billah concentrated on the fabrication and characterization of the multi-chip transmitters. For more details about individual contributions, see the introductory paragraph of Chapter 3.

First demonstration of reliable ultra-low insertion loss PWB and resilience under harsh environmental testing: Fully automated and high-yield mass production of more than a hundred PWB without any defects is realized for the first time. These PWB, exhibiting ultra-low insertion losses of $(0.7 \pm 0.15)\,\text{dB}$, are shown to endure environmental stability tests without degradation even at high optical power, see Section 3.3.1 and journal publication [J7] for details.

First demonstration of permanent over-cladding of PWB: PWB require a cladding material to adjust their index contrast and to enable single-mode operation. This cladding material was previously emulated using index-matching oil with tailored refractive index. Unfortunately, such oils do not provide protection against environmental influences, and they quickly evaporate. Here, a solid cladding material based on an ultraviolet (UV) light curable adhesive is applied to PWB for the first time, see Section 3.3.1 and journal publication [J7] for details. The local cladding process was developed together with A. Hofmann, who built the experimental setup, whereas the author fabricated and evaluated the test samples. For more details about individual contributions, see the introductory paragraph of Chapter 3.

First demonstration of an ultra-broadband fibre-coupled 3D printed polarization beam splitter with integrated rotators: A 3D printed polarization splitter and rotator was designed and fabricated on the end face of optical fibres. The performance of the fibre-coupled device is verified over a wide spectral range, demonstrating a measured polarization extinction ratio of more than 11 dB over a 350 nm wavelength range. A dual-polarization 16QAM data transmission experiment at a wavelength of 1550 nm and a symbol rate of 80 GBd corresponding to an aggregate line rate of 640 Gbit s^{-1} demonstrates that there is no optical signal-to-noise ratio penalty by polarization cross-talk compared to a commercial fibre-based polarization beam splitter for polarization-division multiplexed data, see Chapter 4 and journal publication [J5] for details. The results of this work have been included in two patent applications. Note that the achievements of this work resulted from equal contributions by the author of the thesis and A. Nesic. The author's work was mainly focused on fabrication and design of the polarization rotator, while the work of A. Nesic was mainly focused on design and optimization of the polarization beam splitter. The experimental characterization was done jointly by the author and A. Nesic. For more details about individual contributions, see the introductory paragraph of Chapter 4.

First demonstration of an ultra-broadband out-of-plane coupler for integrated photonic chips: An ultra-broadband out-of-plane coupler for integrated photonic chips is demonstrated for the first time. The coupler combines a PWB with a micro-lens as an interface to optical fibres. A coupling efficiency of -0.8 dB at $\lambda_0 = 1550$ nm with a 1 dB bandwidth exceeding 200 nm is demonstrated, see Chapter 5 and conference contribution [C16], as well as journal publication [J13] for details.

1 Introduction

Modern electronic integrated devices are nearly exclusively created using planar fabrication technologies. In such a planar process, a thin sheet of material, typically referred to as a wafer and often consisting of high-purity silicon, is subjected to a series of high-resolution optical exposures to define tiny two-dimensional regions of photoresist. These regions represent protected and unprotected areas for subsequent processes such as etching, passivation, or doping to change the semiconductor properties of the material. By executing many of such steps, intricately layered micro- and nanostructures can be fabricated. Integrated photonics leverages these planar fabrication technologies to guide light instead inside integrated chips by using dielectric waveguides. Similar to their electronic counterparts, the high level of miniaturization can enable a multitude of functionalities on a compact millimetre-scale chip. In this work, two-photon lithography is used to augment these traditionally planar devices with three-dimensional micro-structures in a wide variety of ways. These optical chips can be made from very different materials, each having their own strengths and weaknesses. One particularly interesting material is silicon: Silicon photonics (SiP) exploits the mature fabrication technology of the complementary metal oxide semiconductor (CMOS) process which is used in virtually all of today's electronic devices. The high refractive index contrast between the silicon waveguide core and the surrounding silicon-oxide cladding allows strong optical confinement of the guided light and enables tight bend radii of the optical waveguides. As a result, exceptionally high levels of integration can be achieved in SiP devices. In addition, SiP does not only enable integration of passive structures such as waveguides, power splitters and grating couplers, but also allows the fabrication

of germanium-based photodetectors and electro-optic modulators using the plasma dispersion effect. The bandgap of silicon, corresponding to the photon energy of near-infrared (NIR) light of approximately 1.1 µm wavelength, allows low-loss waveguides for the typical communication wavelengths in the range of 1.3 µm to 1.6 µm. The huge need for high-performance optical communication is therefore the most important technology driver of integrated photonics. The first products utilizing integrated photonics are therefore focused on addressing this market and commonly based on SiP devices [8]. On the other hand, the indirect bandgap of bulk silicon prevents efficient light emission in silicon photonic structures. Instead, indium phosphide (InP) is the prevalent III-V compound semiconductor used for diode lasers at these wavelengths (1.3 µm to 1.6 µm). Just as with silicon photonics, InP can also be used to realize complex PIC. However, the fabrication process is far less mature. This is evident when the typical InP wafer sizes of different process technologies are compared to the CMOS process: Currently, wafers of InP are only available up to diameters of 100 mm (commonly referred to as 4 inch), whereas well-established CMOS processes use wafers of up to 300 mm diameter (commonly referred to as 12 inch). The smaller size of InP wafers reduces the advantage of wafer-scale fabrication and indicates the immaturity of the InP fabrication process when compared to SiP. In addition to these previously mentioned materials, there are a multitude of other materials used to realize PIC, among these are silicon nitride [9, 10], lithium niobate [11] or even diamond [12] – each with their own advantages and disadvantages.

This wide variety of materials results in one of the key challenges of integrated optics: Providing efficient and compact optical interfaces between optical chips and from chips to fibres, preferably in such a way that multiple optical connections are efficiently coupled at the same time. For electronic chips, these challenges are largely solved: While interfacing an electronic integrated chip to the outside world comes certainly with a host of intricate details, such as signal integrity or interconnect density, in many cases it is sufficient to 'simply' connect with moderate precision a gold bond wire to a metal pad on the chip surface. This contrasts with integrated

photonics, where low-loss single-mode connections require a perfect overlap of the optical modes and are therefore sensitive to the exact geometrical shape and to misalignment in the form of angular tilt and spatial offset. Achieving perfect modal overlap is especially difficult when joining different integration platforms, as different platforms exhibit vastly different and typically very small intrinsic mode fields. The variation is mostly caused by the significant variation in refractive index contrast between the respective platforms. For devices operating at the communication wavelength of 1550 nm, where erbium doped fibre amplifiers are available, the largest commonly occurring mode field diameter[1] (MFD) amounts to 10 μm and belongs to standard single-mode fibres (SMF) at a wavelength around 1550 nm. Even for these relatively large MFD, passive component assembly is rarely possible: Assuming perfectly matched and axially aligned circular Gaussian modes, their 1 dB lateral alignment tolerance is approximately 0.23 × MFD, i.e., only 2.4 μm for a SMF – far below the 5 μm positioning accuracy of most passive optical assembly techniques [13]. Typical devices such as InP lasers and silicon photonic chips feature edge couplers with even smaller MFD of 3 μm, even if mode expanders are integrated [14], making any kind of passive alignment virtually impossible. Such devices are usually assembled using active alignment, a process wherein the coupling efficiency is continuously monitored and the placement of the component is actively optimized [13]. This process is slow and increasingly complex when several interfaces have to be coupled at the same time. In addition, directly interfacing a SMF of 10 μm MFD to such a small 3 μm mode field will only couple 28 % of the power, which makes some variant of mode field adaption a necessity. When coupling between optical chips, such a mode field adaption is typically achieved by using bulky micro-

---

[1]Defined as the diameter of the $1/e^2$ intensity drop. For Gaussian beams the MFD equals twice the beam waist radius w_0.

optics or lensed optical fibres, which, again, have to be actively aligned. All of these solutions generate overhead and are a significant cost driver in optical packaging [15, 16], thereby counteracting the scaling advantage of parallel wafer-based fabrication of the photonic chips themselves.

Three-dimensional (3D) additive micro-fabrication by multi-photon absorption polymerization, commonly referred to as multi-photon lithography (MPL), is in a unique position to address both these issues at the same time. This technology exploits multi-photon absorption inside the tightly confined volume of a highly focused femtosecond laser beam to initiate a localized polymerization of a precursor material with nanometre scale resolution. By this method, transparent polymer structures with lateral and axial resolution of about 300 nm and 750 nm, respectively, can be created thereby enabling the fabrication of a wide variety of three-dimensional photonic structures, such as photonic crystals [17], dielectric waveguides [3], or diffractive and refractive optical elements [18, 19]. As such, MPL is perfectly suited to realize dielectric waveguides, micro-lenses, or prism elements, which can be used to modify and guide the light emitted by integrated photonic devices and fibres. Because MPL systems share many similarities with nonlinear microscopes, many microscopy technologies can also be transferred to lithography systems. The integration of common microscopic imaging modalities, such as bright field, confocal and even nonlinear fluorescence imaging is straightforward. These imaging modalities provide a perfect foundation to automate the precise detection of physical features, e.g., optical interfaces of photonic devices such as edge couplers or grating couplers, with an accuracy better than 100 nm by computer vision. Once the position and orientation of the optical interface is found, the lithography system can be used to print structures such as waveguides or a micro-lenses precisely aligned to the optical interface. The additive manufacturing of such structures may even be done after the photonic chips are placed at their final position with moderate accuracy, thereby

facilitating highly efficient optical coupling. The previously stated need for expensive active alignment in traditional packaging is thereby moved to the lithography system, which allows for precise fabrication of 3D optical elements exactly at the coupling locations.

Electronic integrated circuits are usually interfaced with other components by thin metal wire bridges which are commonly referred to as electrical wire bonds. In analogy to these electrical wire bonds, photonic wire bonds (PWB) interface photonic devices by 3D printed free-form dielectric waveguides which are adapted to the exact location of the photonic devices, thereby eliminating the need for high-precision positioning of the devices themselves. An illustration of the concept can be found in Figure 1.1. The starting and ending position of each PWB is adjusted to the position of the optical interface. The position and orientation of the interface is found automatically using machine vision on confocal and bright field image taken by the lithography system. In-between the two optical interface positions, the PWB waveguide follows a free-form path through space. At the coupling points on either end of the PWB, the shape of the PWB is adapted to act as a spot size converter (SSC), matching the MFD to each optical interface, thereby maximizing the power transmission between the devices. The pitch between adjacent PWB can be very small; the smallest demonstrated pitch is 25 µm. This technique allows automated assembly and mass production of photonic systems, and is therefore expected to be of great importance for the industrial deployment of photonic integrated circuits. Details on the fabrication process and design of the PWB can be found in the next chapter.
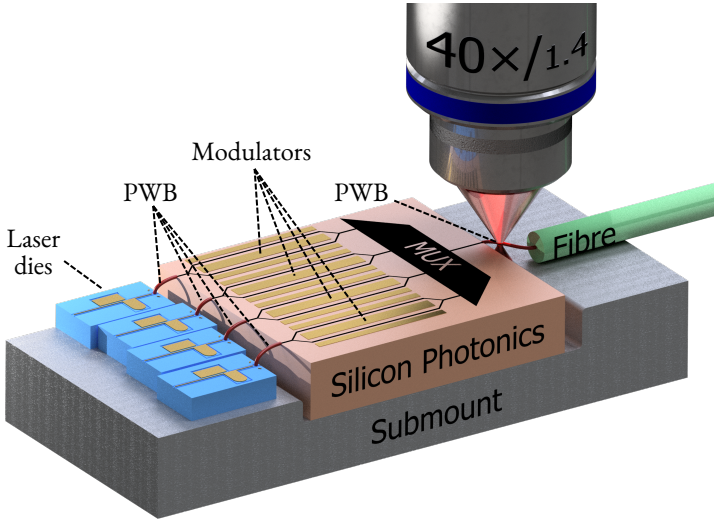
Fig. 1.1: Illustration of a photonic multi-chip module for optical data transmission enabled by photonic wire bonds (PWB). The PWB relax the alignment tolerances of the individual photonic chips and fibres, such that they can be placed without expensive active alignment. The PWB are fabricated by focusing a femtosecond laser beam into a liquid photo-sensitive monomer precursor material (not shown) with the help of a high numerical aperture (NA) objective. At the focal spot of the objective, multi-photon absorption initiates a localized polymerization reaction of the precursor. By moving the focal spot in lateral and axial direction relative to the substrate, the PWB can be defined. The unexposed precursor is washed away by a mild solvent in a follow-up development step. In this example, PWB connect several InP lasers dies emitting light of different wavelengths to a silicon photonic chip. On the SiP chip, the light of each laser is routed to individual modulators for intensity modulation, forming a data signal. Each signal is subsequently multiplexed into a single channel in a wavelength-division multiplexing scheme. The single output channel is then connected to an output fibre via another PWB. The size of the microscope objective is not to scale.

2 Theoretical and technological background

This chapter introduces the theoretical and technological background which is relevant for this work. Section 2.1 introduces multi-photon absorption lithography in general. Section 2.2 describes a multi-photon lithography (MPL) system which was developed in the framework of this dissertation with a particular focus on micro-fabrication aligned to features of photonic integrated circuits (PIC). In Section 2.3, an overview on photon wire bonds (PWB) is given and the typical coupling schemes for interfacing PWB with integrated photonic circuits are described. Section 2.4 describes micro-lenses and gives details on simulating their performance using a recently derived reformulation of the wave propagation method [20].

2.1 Multi-photon three-dimensional lithography

Multi-photon absorption lithography (MPL) has become an enabling technology in the field of micro- and nano-fabrication. Its applications are virtually unlimited and range from photonic meta-materials [21, 22], biological cell cages [23] to micro-robots [24, 25] and compound micro-optical systems [18, 26, 27], to name just a few. This broad range of fabrication capabilities is enabled by the process of multi-photon absorption, which allows the localized initiation of a polymerization process by the simultaneous absorption of two or more photons in the focal spot of

a high-intensity laser. The process of two-photon absorption was first predicted in 1931 by Maria Göppert-Mayer in her doctoral thesis [28]. At this time, the work was highly theoretical since experimental demonstration of multi-photon absorption was thought to be impossible, as it requires tremendously high optical intensities. Her work subsequently remained of little impact. She changed her field of research to atomic physics, where her outstanding work made her the second woman to win a Nobel prize in physics. Thirty years later, in 1960, Theodore Maiman built the first laser, and access to such high light intensities was suddenly possible. Only one year later, the first experimental demonstration of two-photon absorption was performed by Kaiser and Garrett [29] in 1961. Still, it took yet another thirty years until two-photon absorption found practical application when it was first employed for biological microscopy [30]. Nowadays, two-photon-induced fluorescence microscopy is widely employed throughout biology [31]. Many methods from microscopy can also be applied to optical lithography, and multi-photon lithography (MPL) is no exception to this rule. Two-photon polymerization was first demonstrated in 1997 by Shoji Maruo and coworkers, who used a photo-sensitive polymer material [32]. Such materials consist of a monomer precursor material to which a photo-initiator has been added. When exposed to very high intensities, multi-photon absorption occurs in the photo-initiator molecule, triggering a localized cross-linking chain reaction in the monomer, thereby forming a solid polymer. The development of low-cost and compact fibre-based femtosecond laser sources allowed the replacement of the significantly more expensive mode-locked titanium–sapphire lasers and gave rise to the first commercial MPL machines in 2007. Since then, MPL has found widespread adoption by the scientific community and has become the versatile tool of choice [33] for high-resolution 3D lithography.

Nearly all MPL systems employ negative-tone photoresists, where the unexposed resist can be removed by a simple solvent, and only the exposed material remains. These photoresists consist of a monomer precursor material which provides the molecular building blocks that can be cross-linked to form a polymer chain or network. Many possible chemical systems exist, and many have been used for MPL, such as epoxies [34], thiol-ene chemistry [35], methacrylates or acrylates [36].

Today, most photoresists are based on multi-functional acrylates, which are inexpensive, readily available and exhibit high polymerization rates [37]. Typically, acrylates also show significant amounts of undesired shrinkage [38]. They are usually photosensitized by the addition of a photoinitiator [36]. Depending on the required excitation of the photoinitiator, a free radical is generated by the absorption of one or multiple photons (e.g., via cleavage or charge transfer to other molecules), which in turn triggers a chain-growth polymerization. The radical triggers the attachment of one monomer molecule to form a chain, which in turn triggers the generation of a radical. These propagating chains are typically terminated by other radicals or molecular oxygen, which act as inhibitor of the polymerization. An extensive treatment of the subject can be found in Ref. [39]. If a monomer molecule contains multiple polymerizable groups, such as multiple acrylate groups, not only a chain is formed, but rather a cross-linked polymer network. Once the polymer network reaches a degree of polymerization above a certain threshold value, it becomes insoluble to the developer. One can easily imagine that unrestrained propagation of the polymerization reaction would reduce the achievable resolution of the photoresist. Photoresist materials are therefore engineered to only locally cross-link, e.g., by the presence of polymerization inhibitors. In particular, since oxygen can terminate the polymerization reaction, its presence in the resist significantly impacts the polymerization dynamics [40], and has a significant impact on the achievable resolution. Typically, commercial photoresist materials are well optimized such that the polymerization dynamic only plays a minor role in the achievable resolution and the achievable resolution is limited by the optical resolution of the lithography system.

The effect of the lithography system on the polymerization is often expressed in a 'deposited lithography dose'. This dose correlates the locally achieved degree of polymerization with the overall lithography process. Defining such a deposited lithography dose $\mathcal{D}$, experienced by a photoresist in a volume element ('volume pixel', voxel) is non-trivial, and no closed form exists. However, a good approximation is that the deposited lithography dose $\mathcal{D}$ is proportional to the amount of generated radicals [36]. When a radical-based photoinitiator is excited by multiple photons, a radical is generated which subsequently triggers a polymerization chain reaction with a certain likelihood. The average number of photons which are simultaneously absorbed and excite the generation of a radical is commonly referred to as the nonlinearity order N. The deposited lithography dose $\mathcal{D}$ is therefore directly proportional to $\tau\phi^N$, where τ is the exposure time and ϕ local photon flux. Since the photon flux is proportional to the laser power P and the focal volume is approximately constant, the relation is typically expressed as $\mathcal{D} \propto \tau P^N$. The nonlinearity order depends on the photoinitiator used to photosensitize the monomer material of the photoresist, and on the lithography wavelength [41]. There already exists a myriad of known photoinitiators designed for exposure with ultraviolet (UV) light. Many of these UV-sensitive photoinitiators exhibit two-photon absorption ($N = 2$) at half the UV photon energy, i.e., a near infrared (NIR) exposure wavelength of approximately 800 nm. However, more complex absorption processes, such as cascaded absorption via a triplet state, are also known to occur and give rise to nonlinearity orders of $N > 2$ [41].

The behaviour of many photoresists can be described by a threshold model: If the resist was locally exposed to a dose exceeding a threshold value $\mathcal{D}_{\text{th}}$, it becomes insoluble. After exposure, a wash in a mild solvent removes all volumes where $\mathcal{D} < \mathcal{D}_{\text{th}}$, leaving only the parts of the structure where the threshold dose was exceeded. This model is commonly referred to as the 'step-threshold model' [41].
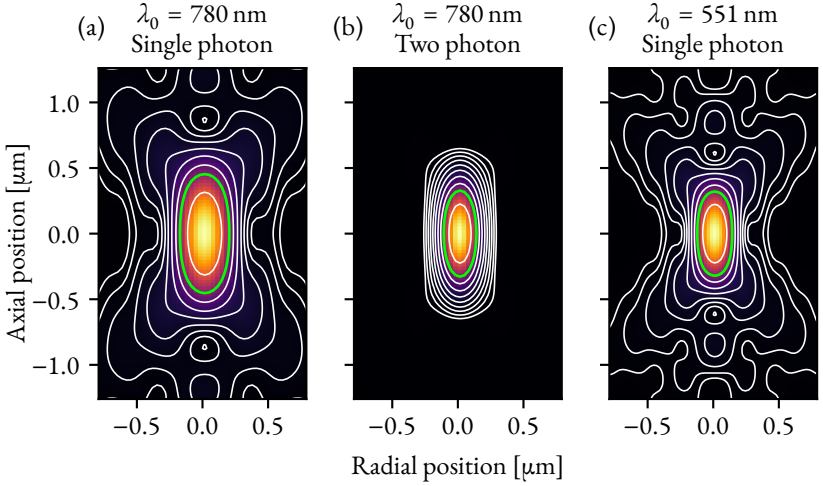
Fig. 2.1: Simulated deposited lithography dose $\mathcal{D}$ in a photoresist (n_{resist} = 1.518) by a microscope objective (NA = 1.4) for different wavelengths λ_0 and absorption orders. Contour lines indicate 2 dB steps of deposited dose. The green contour line indicates the contour at which the deposited dose has dropped by a factor of e^{-1} compared to its peak value. **(a)** Single-photon absorption of 780 nm light shows low resolution and significant axial side lobes which result in dose accumulation when multiple adjacent positions are exposed. **(b)** Two-photon absorption increases the resolution and suppresses the side lobes such that the dose is only deposited locally. **(c)** Single-photon absorption at a wavelength of $2^{-1/2} \times 780$ nm ≈ 551 nm provides nominally identical resolution, while side lobes remain a significant contribution.

Figure 2.1 depicts the deposited dose distribution $\mathcal{D}$ of a laser beam focused by a high numerical aperture (NA) objective for different orders of absorption N and laser vacuum wavelength λ_0. Assuming the step-threshold model, one can arbitrarily adjust the laser power P such that the threshold dose $\mathcal{D}_{th}$ is exceeded at any of the contour line shown in Figure 2.1, thereby forming an solidified volume element if varying volume. As expected, the single-photon dose distribution (λ_0 = 780 nm, N = 1) exhibits a lower resolution than the two-photon (λ_0 = 780 nm, N = 2) dose distribution, see Figures 2.1a and b, respectively. In fact, an N-th order

absorption process will enhance the achieved resolution by a factor of $N^{-1/2}$. It is often wrongly claimed that the advantage of multi-photon absorption lies in this resolution enhancing capabilities. Specifically, as can be seen in Figure 2.1c, the same resolution can be achieved by using a green laser and single-photon absorption (λ_0 = 780 nm, N = 1) . In effect, both the linear and the nonlinear absorption process are able to expose a single volume element at the same resolution. A single exposed volume element (voxel) can even be made as small as a few monomer molecules, by simply choosing a tiny amount of deposited dose which just barely exceeds the polymerization threshold – independently of the laser wavelength or the nonlinearity of the absorption process.

A special case occurs if the incident laser is far below the polymerization threshold. In this case, the dose often fails to accumulate, even if the same voxel volume is illuminated indefinitely. Such a minimum rate of dose, often referred to as the Schwarzschild threshold, is due to the diffusion of the generated radicals and the termination of chain reactions, e.g., by oxygen, diffusing into the voxel volume. It is named after the astronomer Karl Schwarzschild who discovered that light of weak stars fails to expose photographic plates even for long exposures.

The advantage of multi-photon excitation comes into play, once multiple volumes are exposed close to each other such that the deposited doses of each focus overlap and add up. In the case of traditional one-photon absorption (N = 1), the side lobes of the point spread function (PSF) are significant and will add up over all exposed voxels, preventing the fabrication of complex 3D structures. This of special importance when exposing large areas parallel to the focal plane. In this case, the accumulated photon flux along the optical axis is approximately constant, which prevents 3D structuring for single-photon sensitive photoresist, sensitive to the accumulated dose. In contrast, since the side lobes of the optical PSF are suppressed in the deposited dose for nonlinear absorption ($N > 1$), such off-target dose fails to accumulate significantly. The superiority of the multi-photon absorption process over the single-photon process therefore does not lie in the higher spatial resolution, but rather in the suppression of the focus side lobes. However, adjacent features are

always limited by the accumulation of the deposited dose, even if the dose side lobes are suppressed. The finite size of the dose distribution therefore limits the achievable minimal distance between voxels for which individual features can be resolved. This fact that single-point exposures can become virtually arbitrarily small, while the distance between adjacent voxels is limited, is called the multi-photon Sparrow limit[1] [41]. The minimum distance between two separated voxels is commonly referred to as the 'resolution of the lithography system'. While chemical effects in the resist material can certainly play a role, this resolution is primarily given by the optical resolution of the lithography system, typically determined by the numerical aperture (NA) of the objective, the vacuum wavelength λ_0, the nonlinearity N of the absorption process and the refractive index of the resist material n.

There is no closed analytical expression to describe the deposited dose of a single voxel exposed by a high-NA objective, since there is no closed-form expression for the point spread function (PSF) of a high-NA objective. The dose distributions shown in Figure 2.1 are based on numerical simulations of the optical PSF [43]. Fortunately, the side lobes of the PSF are suppressed in the case of a multi-photon absorption process of order N, such that the dose distribution which is generated by the nonlinear absorption of the optical PSF can be well approximated by a 3D normal distribution centred around the focal point:

$$\mathcal{D}\left(x, y, z\right) = \mathcal{D}_0 \times \mathrm{e}^{-\frac{x^2+y^2}{2\sigma_{xy}^2}} \, \mathrm{e}^{-\frac{z^2}{2\sigma_z^2}} \tag{2.1.1}$$

The dose distribution $\mathcal{D}$ is rotationally symmetric around the optical axis (z direction) and only depends on the distance from the optical axis $r = \sqrt{x^2 + y^2}$. The dose $\mathcal{D}$ drops by a factor of $1/\mathrm{e}$ at a distance of $r = \sigma_{xy}$. Similarly, the dose distribution drops by a factor of $1/\mathrm{e}$ at a distance of σ_z from the focal plane located at $z = 0$. An

---

[1]Sparrow originally investigated the resolution of spectroscopes limited by diffraction [42]. He found that spectral lines can still be resolved if there is a local minimum between the two signals. Such a minimum is also required to allow separation of two voxel by choosing the minimum dose to fall just below the polymerization threshold., resulting in separated voxels.

approximation for σ_{xy} and σ_z, based on numerical calculations, is given by Zipfel *et al.* [31] as

$$\sigma_{xy} = \begin{cases} \dfrac{0.155\lambda_0}{\sqrt{N} \times \mathrm{NA}}, & \text{for NA} \le 0.7 \\[4mm] \dfrac{0.230\lambda_0}{\sqrt{N} \times \mathrm{NA}^{0.91}}, & \text{for NA} > 0.7 \end{cases} \qquad \text{and } \sigma_z = \frac{0.376\lambda_0}{\sqrt{N}} \left[\frac{1}{n - \sqrt{n^2 - \mathrm{NA}^2}} \right]$$

$$(2.1.2)$$

and depends on the numerical aperture NA, the nonlinearity order of the photoresist N, as well as the laser vacuum wavelength λ_0 and the refractive index of the resist material n. The parameters σ_{xy} and σ_z of the normal distribution can be directly interpreted as half the voxel size in lateral and axial direction, respectively, when the step-threshold dose $\mathcal{D}_{\mathrm{th}}$ lies at $1/e$ of the peak dose and is indicated by a green contour line in Figure 2.1. Note that the axial size of the dose distribution scales approximately quadratically with NA, while the lateral size scales only linearly with the NA. This explains the necessity of using a high-NA objective for the fabrication of 3D micro-structures, in particular for cases where a high axial resolution is required. Unfortunately, even objectives with the highest numerical aperture only illuminate one half-space of the solid angle from the direction of the objective[2]. Technical implementations usually reach an NA of up to 1.4 using an immersion medium of refractive index $n = 1.518$ and $\lambda_0 = 780\,\mathrm{nm}$, resulting in a deposited dose distributions of lateral dimension $\sigma_{xy} \approx 132\,\mathrm{nm}$ and axial dimension of $\sigma_z \approx 315\,\mathrm{nm}$ for $N = 2$. In such a case, the achievable aspect ratio σ_z/σ_{xy} is 2.4.

---

[2]There are attempts to build lithography machines with full 4π solid angle illumination [44]. These systems usually consist of two high-NA objectives, where the focus of both objectives requires precise spatio-temporal alignment to each other.

It is instructive to realize that only the advent of bright ultra-short pulse lasers enables intensities high enough to reach a meaningful number of excited photoinitiator molecules and to achieve a cross-linked material. Assuming a moderate time averaged power[3] of a mode-locked laser at $\langle P \rangle$ = 100 mW with pulses of duration τ = 100 fs at a central wavelength of λ_0 = 800 nm and repetition rate f_{rep} = 100 MHz, peak power levels of $P_{\mathrm{peak}} \approx \langle P \rangle / (f_{\mathrm{rep}} \tau)$ = 10 kW can be obtained. Focused by an objective with a very high numerical aperture of 1.4, the light gets concentrated to an effective area of approximately $\pi \left(\lambda_0 / (2 \times \mathrm{NA}) \right)^2$ = 2.4×10^{-9} cm^2, resulting in a peak intensity of approximately 4×10^{12} W cm^{-2}. Such a peak intensity is equal to a fifth of the globally generated power focused to an area the size of a thumbnail. Since each photon carries an energy hc/λ_0, a peak photon flux intensity of $I_{\mathrm{peak}} \approx 1.46 \times 10^{31}$ photons/cm^2/s occurs in the focus of the objective. For two photon absorption, the number of absorbed photons per volume and pulse is then approximately $N_{\mathrm{2PA}} \approx C \delta I_{\mathrm{peak}}^2 \tau$, where C is the photoinitiator concentration, typically in the order of 60 mmol/L, or 3.6×10^{19} 1/cm^3, and δ is the two-photon cross-section. The typical absorption cross-section of such a photoinitiator is in the order of 1 GM, a unit named after the aforementioned Maria Göppert-Mayer, where 1 GM = 1×10^{-50} cm^{4}s/photon. Assuming that each absorbed photon excites a photoinitiator molecule, this yields an molecule excitation density of around 10×10^{18} molecules/cm^3, which corresponds to one exited molecule per 5 nm × 5 nm×5 nm of resist volume. While this calculation neglected the quantum efficiency and the efficiency to initiate a polymerization reaction, such effects are compensated by the fact that one voxel is typically exposed to tens of femtosecond laser pulses, thereby exciting a significant percentage of the whole photo-initiator population and making multi-photon 3D lithography possible.

---

[3] Most recent fibre-based femtosecond lasers reach above 1 W average output power, putting them in the realm of traditional titanium–sapphire lasers. Even accounting for loss in the delivery optics, significantly higher doses than assumed here can be delivered and may enable exposure with high voxel deflection velocity.

2.2 Automated lithography machine for aligned fabrication

Multi-photon lithography is capable of fabricating complex micro-structures. However, when it comes to optical assembly, fabricating such structures is not sufficient – it is also required to place them at the correct position and with the correct orientation. Such precise placement was traditionally not required and was hence not a focus of commercial lithography machines. Indeed, a vast majority of applications utilizing MPL rely on simple flat substrates such as glass or unstructured silicon wafers, which are simply used as a carrier for the process. Only recently, a stronger focus on aligned fabrication has emerged: Some notable exceptions include micro-optics directly fabricated on camera chips and on fibre bundles for endoscopic imaging [19], integrated structures on MEMS devices [45], and complex dielectric waveguide devices [46]. All these examples prove the principle applicability of MPL to augment existing devices with optical functionalities. However, a manual alignment process was still used in all of them.

In contrast, this work makes heavy use of automated alignment and fabrication, and it recognizes automation as a prerequisite for reliable and high-yield fabrication. This work mostly builds on a commercial MPL system exploiting galvanometric mirrors for fast beam deflection, complemented by a confocal imaging unit [47]. When used for confocal imaging, the lithography focus is scanned over an area at a power level below the polymerization threshold dose. The backscattered light can then be detected, and a volume image can be reconstructed based on the known focus location. Such confocal imaging allows the acquisition of images which are inherently aligned to the lithographic coordinate system. A core element of this dissertation was to replace the original control software with a new modular software stack, specifically designed to fabricate 3D structures aligned to optical interfaces on chips and fibres.

Because the initially used commercial system was not readily extendable, a second device designed for research and improved process control was developed in this dissertation and used for the results presented in Chapter 4. This system utilizes the same software framework but improves the features of the commercial system, while providing an open platform for experiments. Like the commercial system, the research system incorporates galvanometric mirrors for high-speed beam deflection, and a confocal imaging system. Among other improvements, it also includes a multi-photon fluorescence imaging unit which captures the fluorescence light that is emitted by a fraction of the photoinitiator molecules upon two-photon excitation. This system also provides a higher maximum lithographic dose by employing a high-power laser, optimized optics and shorter femtosecond pulses.

While both lithography systems are capable of fabricating the structures discussed in this dissertation, the following text will mostly focus on the research system, where detailed information on all aspects of the system are available. Additionally, extensions to the lithography system such as the aforementioned multi-photon fluorescence and confocal imaging unit allow novel schemes for alignment and fabrication not found in other systems. In cases where the differences between the lithography systems significantly affect the lithographical process, the differences will be pointed out.

2.2.1 System layout

The system schematic is depicted in Figure 2.2 and will be discussed in the following paragraph. More details on the used components can be found in Appendix D.2.

As previously discussed, high photon fluxes are required to initiate multi-photon absorption inside the UV-sensitized monomer. The excitation wavelength is typically around 800 nm, providing enough energy to initiate polymerization via absorption of two photons by a common UV-sensitive photoinitiator. All systems used in this dissertation employ fibre-based fs-laser systems of either 80 MHz or 100 MHz

repetition rate. After the laser, a prism-based pulse compressor pre-chirps the fs-pulse to compensate the group delay dispersion (GDD) introduced by the downstream optics. The dominant contributors to the GDD are the acousto-optic modulator (AOM) based on tellurium dioxide (TeO_2), and the high-NA microscope objective.

The femtosecond laser light is modulated by an acousto-optic modulator thereby allowing precise control of the deposited dose in the photoresist. The acousto-optic modulator uses a process in which phonon-photon scattering deflects light in proportion to the AOM drive signal. The diffracted first-order light is subsequently guided to a variable beam expander. The magnification of the beam expander can be manually modified to allow optimal illumination of the objective aperture. In forward direction, a 90/10 splitter passes 10 % of the light to a photo diode used to calibrate the AOM power transfer function. In backward direction, scattered light from the sample may pass through the same splitter and is focused through a pinhole onto a photodetector, thereby only allowing the light reflected from the laser focus in the sample to reach the photodetector. Recording a time series of the photodetector signal as well as the position of the laser spot in the sample plane allows confocal imaging with the lithography laser.

The light is finally guided to a high-NA objective mounted in an inverted microscope [48]. The objective focuses the laser beam into liquid photoresist which is also used as the immersion medium for the objective. Its focus spot can be deflected by a pair of galvanometric XY mirrors and thereby positioned anywhere on the intermediate image plane after the $f\theta$ scan lens[4]. While not shown in Figure 2.2, the X and Y axis of the individual galvanometric scanners are optically imaged onto each other using a relay optic [49], which results in virtually zero optical distance between the mirror axes and is a prerequisite to provide constant illumination of the back

---

[4]Scan lenses are typically optimized for a flat field. The focus displacement is often found to be $f \tan \theta$ where f corresponds to the focal length of the lens and θ is the deflection angle of the laser beam imparted by the galvanometric scanning mirrors. The nonlinear dependency of the displacement of the focus spot on the deflection angle can be problematic and requires a non constant velocity of the galvanometric mirrors to achieve a constant displacement velocity of the focus. So-called $f\theta$ lenses include a barrel distortion that yields a displacement that is linear with θ.

aperture of the objective during X/Y deflection. Such an approach provides a good optical performance even at high deflection angles. The intermediate image after the scan lens is projected and de-magnified by the microscope objective and a tube lens. The system is typically used with an 40× 1.4 NA objective in an infinity-corrected optical system configuration. Three-dimensional structures are written by moving the objective relative to the sample in Z direction by means of a dedicated piezoelectric actuator.

The lithography system includes multiple imaging modalities: In addition to traditional bright field imaging, confocal imaging using the lithography laser allows for precise alignment to preexisting objects on the sample in the coordinate system of the laser. Non-destructive imagining without exposure and subsequent polymerization of the photoresist is possible when a lithographic dose below the Schwarzschild threshold is used.

An additional detection modality allows multi-photon fluorescence imaging using the intrinsic fluorescence of the photoinitiator inside the photoresist. The existence of a signal then indicates the presence of photoresist, and a lack of a signal indicates the presence of a structure such as a SMF or other transparent objects. The fluorescence can be collected through the microscope objective and is used for advanced resist-glass interface detection, see Appendix D.1 for details. The fluorescence light is 'descanned' by the beam deflection system[5] and afterwards split off from the main beam by a dichroic mirror. Residual laser light is suppressed by a short-pass filter and focused into a multimode fibre (MMF) to guide the light to a photo multiplier tube (PMT). In contrast to confocal imaging, spatial filtering is not required, since the nonlinear generation of fluorescence photons is already localized to the focal spot. The large acceptance area of the MMF avoids undesired spatial filtering.

---

[5]In a 'descanned' geometry, the emitted light returns along the same path as the excitation light. The detection system basically moves with the deflection of the beam. In a 'non-descanned' system, all emitted fluorescence is directly detected without passing through the beam deflection optic. The drawback of the technically easier 'non-descanned' systems is the decreased sensitivity and the position dependent detection efficiency.

The beam deflection and actuator positions of the microscope, as well as the imaging and AOM transmission, are synchronously controlled by a computer. The sampling rate of the beam deflection, of the AOM and of the imaging channels is 250 kHz.

The schematic of the research system, shown in Figure 2.2, is also a good approximation of the commercial system. However, the commercial system does not include the fluorescence imaging path, the pulse compressor, nor the variable beam expander. A confocal imaging path is also not generally available in commercial systems.
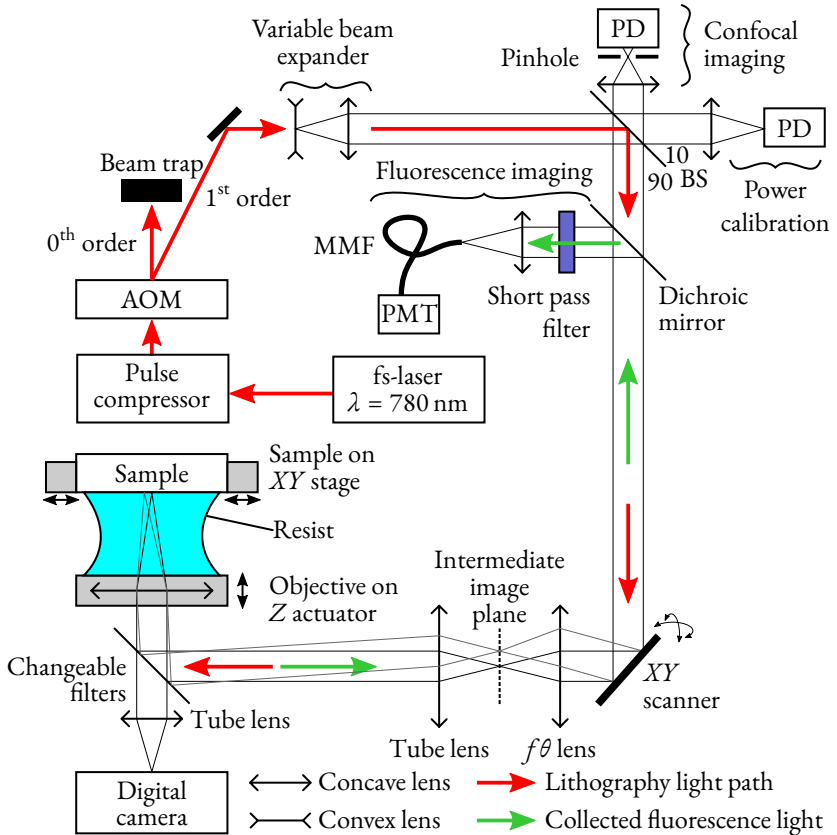
Fig. 2.2: Schematic optical setup of the DLW setup implemented in this dissertation. The femtosecond laser light is deflected by an acousto-optic modulator (AOM) which allows fast modulation of the optical power contained in the first diffraction order. The light is then guided to a high-NA objective which focuses the laser beam into a liquid photoresist which also serves as an immersion medium. Galvanometric XY scanners allow for fast deflection in the image plane. Confocal imaging with the lithography laser allows precise alignment to preexisting objects on the sample. Multi-photon fluorescence of the photoresist can be collected through the microscope objective and used for resist-glass interface detection. The reflection illumination for bright field imaging has been omitted for simplicity. Details on the used components can be found in Appendix D.2.

2.3 Photonic wire bonding

One of the many technologies enabled by multi-photon lithography is the fabrication of dielectric waveguides, commonly referred to as photonic wire bonds (PWB). Such a waveguide follows a free-form path through the space between optical devices, and guides light with low loss between these two devices. This path is usually chosen to be differentiable and be smooth to at least the first derivative, i.e., the path is described by a C^1 continuous function. The concept of photonic wire bonding [3] is exploited throughout this dissertation. It is predominantly applicable to the field of photonic packaging, since it provides a way to guide light between integrated photonic chips [5, 50]. Chapter 3 demonstrates their use for chip-to-chip connections in a series of experiments under technically relevant conditions.

In addition to the waveguides, mode converters may be attached to either or both ends of the PWB waveguide (WG) section. These sections are used to convert the WG mode field to that of the respective device that is to be connected. It can therefore be used to facilitate a connection between components which cannot easily be interfaced due to their vastly different mode fields. One common example is a connection between a single-mode fibre (SMF) with a 10 μm MFD at 1550 nm and a coarsely placed silicon photonic chip with an intrinsic MFD smaller than 500 nm. The PWB will correct any placements errors of chips by adapting the waveguide path to the chip locations just before the fabrication step, allowing a coarse positioning of the fibre and the SiP chip. Mode converters at either end of the PWB WG section are used to adapt the PWB waveguide mode to the SiP chip and fibre interface [3]. A schematic drawing of a possible multi-chip module (MCM) enabled by such a connection is shown in Figure 2.3.

The concept of PWB is, however, not only limited to connecting two individual devices: PWB can also be fabricated on top of a single integrated photonic device, bridging two points by a 3D out-of-plane waveguide. Such a waveguide allows crossings with significantly reduced cross-talk in topologies such as in photonic
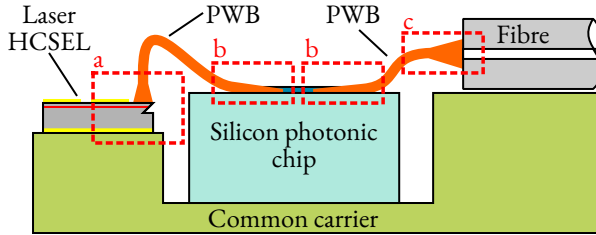
Fig. 2.3: Overview of commonly used photonic wire bond (PWB) interfaces (dashed red boxes). The PWB illustrated here are coupled to different devices: **(a)** Horizontal-cavity surface-emitting laser (HCSEL). **(b)** Silicon photonic chips, and **(c)** bare single mode fibres. The interfaces are standardized and always employ identical coupling schemes which includes mode conversion and the initial routing away from the component. The common carrier compensates differences in die thickness. A precise alignment of the optical component, such as the laser and the Si waveguide, is not required since any offset is compensated by properly routing the PWB. Taper structures are utilized at the interfaces located at both ends of the PWB for low-loss transition between the PWB waveguide (WG) section and the attached components. Localization and measurement of the interface orientation is typically automated. Usually, a PWB connection consists of two PWB taper structures connected by a waveguide, which follows a free-form 3D path to connect the two taper structures.

switches [51]. Another possibility is the customization of a photonic chip in a final low-cost lithographic step, similar to programmable logic devices in electronics [52–54]. Finally, when PWB are terminated by micro-lenses, they can be used to create broadband out-of-plane couplers [6, 55, 56].

This section explores possible design choices for PWB under the constraints of reliable manufacturability. These selected design parameters are subsequently used in all experiments of Chapter 3 and 4.

2.3.1 Core waveguide

Key parameters of PWB are the dimensions and the refractive index of the waveguide core n_{core} and the refractive index of its surrounding cladding material n_{cladd}. In this work, the PWB is used to route light at communication wavelengths $\lambda_0 \approx 1550$ nm between prepositioned chips along the 3D PWB waveguide path. The length of a PWB, i.e., the waveguide section and the optional mode converter sections, is typically limited to around 150 μm to 250 μm by mechanical stability, as well as by the write field of the lithography objective. Since the path of the PWB is also required to be at least C^1 continuous, connecting two components often necessitates waveguide bends with a minimum radius as low as 30 μm [57, 58]. This is especially important when using off-the-shelf components, which might exhibit vastly different substrate heights and directions of light emission, and therefore require complex routing of the PWB. Such complex paths appear for example in connections between horizontal-cavity surface-emitting laser (HCSEL) and Silicon photonic chips, see Figure 2.3 and Ref. [50]. The waveguide should preferably be single-mode to avoid the excitation of higher-order modes, while also being polarization maintaining, which restricts the choice of waveguide cross-sections and the refractive index contrast between the core and surrounding material. Finally, to achieve polarization maintaining operation, the geometry of the waveguide should be asymmetric in such a way that the effective refractive indices of the two orthogonally polarized modes differ strongly.

All these parameters are interdependent, and a possible scheme to find such parameters is shown in Figure 2.4. In the following paragraph, the steps outlined in this scheme will be explained and the requirements will be discussed in detail.

Step 1: Find the lithographic constraints for cross-section and core refractive index n_{core}. The structuring of thin dielectric waveguides is at the very limit of the MPL fabrication capabilities. While sub-micrometre feature sizes are certainly possible, especially when using lithography doses barely about the threshold dose, very long and thereby high-aspect ratio PWB waveguides require

Considerations

- PWB cross-section is constrained by mechanical stability and lithographic resolution.

- Bend radius limited by write field size, component placement and mechanical stability.

- Refractive index is given by photo resist.

Step 1

Find lithographic constraints for cross-section, n_{core} and minimum bend radius R_{min}

$2.0\,\mu m \times 1.8\,\mu m$
$n_{core} = 1.53$
$R_{min} = 30\,\mu m$

- Curved waveguide mode solvers can be used. [59]

Step 2

Find maximum cladding index n_{clad} for which $a_{90°}(R_{min}) \lesssim 0.5\,dB$

$n_{clad} = 1.36$, see Figure 2.5

- Minimize number of guided modes to avoid multimode interference.

- Polarization maintaining PWB require a non degenerate fundamental mode.

Step 3

Find number of guided modes of waveguide

3 modes per polarization, see Figure 2.6

- Required if both components are polarization sensitive or maintaining.

Are polarization maintaining PWB required?

yes

no

- Avoid polarization rotation by using PWB path in one predominant plane.

- Make sure the input and output target polarization of the components are aligned.

Step 4

Constraints on PWB path and component placement

- Freedom to use 3D PWB path within design limits.

3D PWB methodology fully applicable

Fig. 2.4: Design process for photonic wire bond parameters derived from lithographic and process constraints. The lithographic constraints dictate the minimal PWB cross-section and the core refractive index n_{core}. The cladding material refractive index n_{clad} is than chosen such that the minimum required bend radius only incurs acceptable losses. Unfortunately, the resulting geometry still guides three modes per polarization, resulting in a degenerate fundamental mode. PWB between polarization sensitive components hence require further constraints on the waveguide path and placement of the components.

high mechanical stability and therefore a high degree of cross-linking of the polymer. Such mechanically stable structures can only be achieved using doses significantly above the polymerization threshold, thereby sacrificing resolution and limiting the minimally achievable cross-section of the PWB waveguide.

The exploration of the possible design space therefore starts with the physical limits of the lithographic process, which is step one in Figure 2.4. It was shown in Eq. (2.1.2) of Section 2.1 that the axial resolution σ_z of a MPL system is highly depending on the numerical aperture of the objective. To achieve the smallest possible cross-section, such structures have therefore to be fabricated by the highest-NA objectives available, which are typically oil immersion objectives with NA = 1.4. Instead of immersion oil, however, nearly all MPL systems use the resist material as an immersion medium. This trick allows diffraction-limited optical operation while maintaining the full working distance of the objective and dramatically simplifying the lithographic process[6]. To reach a diffraction-limited spot, the refractive index must be higher than the numerical aperture of the objective and well matched to the design of the objective. Typical refractive indices of immersion oils are around n_{oil} = 1.518, which subsequently also applies to the monomer precursor[7] used as an immersion medium. The refractive index of the cross-linked polymerized material is also very similar to its monomer [60], such that the refractive index of the core material of the PWB is around n_{core} = 1.53.

---

[6]Commercial MPL systems typically use objectives originally designed for biological imaging. Such objectives use a stack of immersion oil, 170 μm of cover slip glass, followed by the watery sample. Aberration-free imaging is very often only achieved very close to the glass-sample interface, since focussing deeper into the sample introduces aberrations caused by the refractive index mismatch of the sample. For lithography, the biological sample can also be replaced by resist material. However, the focus quality is also effected and decreases with increasing distance from the glass-resist interface. This effect limits the working distance to a few tens of micrometres. Replacing the stack of oil and glass by a resist of the correct refractive index dramatically simplifies the lithography and allows using the full working distance of the objective. In such a configuration, typical high-NA immersion objectives achieve a high working distance of 300 μm.

[7]Note that such monomers usually contain more than one species of molecule, each exhibiting its own distinct refractive-index. Only the effective media of the monomer blend exhibits the correct refractive index. Polymers derived from multiple species of monomer are often referred to as copolymers.

PWB typically bridge a gap 'horizontally', predominantly describing a path in the focal plane of the objective, i.e., orthogonal to the axis of the objective. This is significant, since the axial direction is the direction of lowest resolution and therefore the hardest to manufacture. Using a state-of-the-art MPL system and an objective of NA = 1.4, the smallest voxel height is in the order of $2\sigma_z \approx 630$ nm, putting a lower limit on the waveguide height. However, a high lithography dose $\mathcal{D}$ is required to create densely cross-linked and therefore mechanically stable dielectric waveguide.

In this work, the smallest stable PWB cross-section was found to be a rectangular cross-section 2.0 μm × 1.8 μm in width and height, respectively, and is used in all experiments if not stated otherwise. This cross-section is smaller than the cross-sections reported by other research groups, who have reported rectangular cross-sections of 3.0 μm×1.2 μm (design) [46], (4.4±0.5) μm×(3.0±0.1) μm (measured) [61], as well as circular cross-section of design diameter of 4.0 μm [62] and 2.0 μm [63]. Note that design cross-sections do not include the voxel size and tend to be around 600 nm to 800 nm larger in axial direction when fabricated.

This cross-section limit naturally holds only for predominantly horizontal waveguides parallel to the focal plane of the lithography objective. If the waveguide is oriented along the axis of the objective, far smaller waveguides are possible, since the lateral resolution of the system is better by at least a factor of two. In fact, cross-sections down to 0.4 μm × 1.2 μm have been shown and are used to realize a polarisation beam splitter and rotator in Chapter 4. This fact also explains why the waveguide cross-section was chosen to be rectangular: The high lateral resolution allows precise definitions of the waveguide corners, while the low axial resolution and the resulting elongated form of the writing voxel makes other WG cross-section shapes hard to achieve.

Step 2: Find maximum cladding refractive index n_{clad} where radiation loss is still acceptable.   As initially mentioned, a bend radius down to 30 μm should be achieved with a radiation loss below 0.5 dB per 90° arc, see step two in Figure 2.4. Given the aforementioned lithographic limits on the smallest PWB cross-
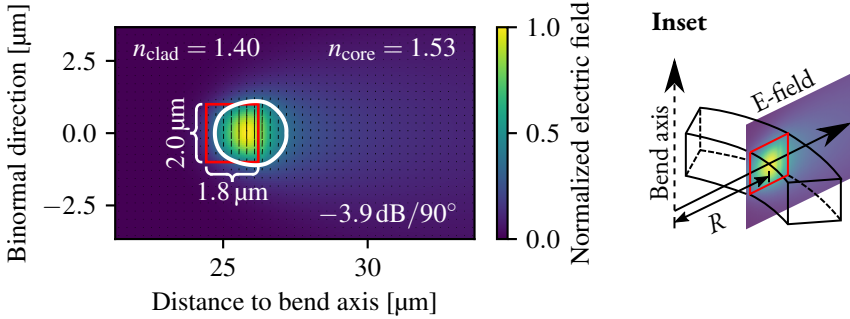
(a) Electric field distribution of the fundamental mode of a bent waveguide. The waveguide, indicated by the red outline, is embedded in a cladding material of $n_{clad} = 1.40$. The waveguide is bent in a circle of radius $R = 25\,\mu m$, see inset.. The electric field, indicated by the black dashed lines, is oriented predominantly along the long side of the waveguide cross-section and indicated by the black lines. The mode is only weakly confined to the waveguide core and extends far outside the waveguide in radial direction. The radiation loss of the mode is 3.9 dB per 90° bend and clearly exceeding the acceptable loss of a PWB. The white line indicates the contour at which the field has dropped by a factor of e^{-1} compared to its peak value in the waveguide core.
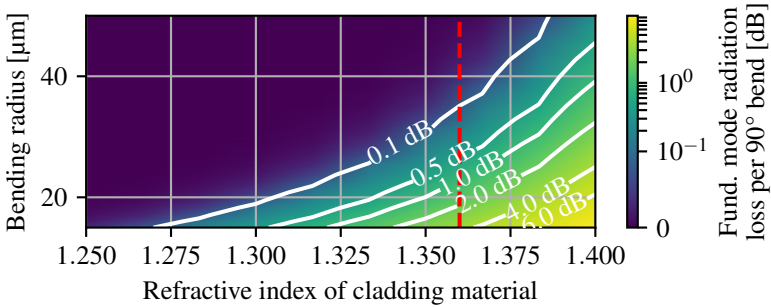
(b) Radiation loss of the fundamental mode for combinations of refractive index cladding material and bend radius. For each combination, the fundamental mode and its radiation loss is found as shown in Subfigure (a). The targeted design loss is 0.5 dB for a 90° bend of 30 μm radius. The maximum cladding refractive index fulfilling this condition is found to be $n_{clad} = 1.36$.

Fig. 2.5: Study on the radiation loss of the fundamental mode of a bent dielectric waveguide for different combinations of refractive index cladding material and bend radius. The waveguide features a cross-section of 2.0 μm × 1.8 μm and a core refractive index of $n_{core} = 1.53$. The axis of rotation is chosen to be parallel to the longer waveguide side and parallel to the dominant electric field direction.

section of 2.0 μm × 1.8 μm and a core refractive index n_{core} = 1.53 determined by the resist material, the only remaining free parameters are the refractive index of the cladding material n_{clad} which surrounds the PWB, and the minimal allowed bend radius of the waveguide. The refractive index of the cladding material should be chosen as high as possible to allow single-mode operation, while being low enough to provide sufficient index contrast to minimize radiative losses in narrow bends. Figure 2.5 depicts the loss encountered for a fundamental mode in a curved waveguide [59] per 90° arc length for varying combinations of bend radius and cladding material.

Most PIC operate with an electrical field polarized parallel to the chip surface and are bridged by a PWB parallel to the PIC surface. In most cases, PWB therefore guide light with the electric field oriented parallel to the longer side of the PWB waveguide cross-section. This analysis of the PWB radiation loss is hence focused on this orientation of the electric field. The results are depicted in Figure 2.5b, indicating that a cladding refractive index of n_{clad} = 1.36 is the highest possible cladding material with acceptable losses for a 30 μm bend radius.

In commercial applications of PWB, it may be possible to further increase the minimum bend radius by moving away from off-the-shelf components and switching to carefully designed custom PIC, placed on a well-designed submount. For example, InP laser chips can be placed into pockets which are precisely etched into the top surface of a SiP chip [63]. In such cases, the emission direction and interface height difference can be chosen such that the optical interfaces line up perfectly, and a minimum radius of curvature above 100 μm is achieved.

Step 3: Find number of guided modes. In step three of the design process outlined in Figure 2.4, we analyse if the chosen parameters (2.0 μm × 1.8 μm, n_{core} = 1.53, n_{clad} = 1.36, λ_0 = 1550 nm) result in a single-moded waveguide. Unfortunately, it turns out that this is not the case. As shown in Figure 2.6, a straight waveguide with the chosen parameters guides up to three horizontally polarized modes. Single-mode operation would require significantly smaller cross-sections in
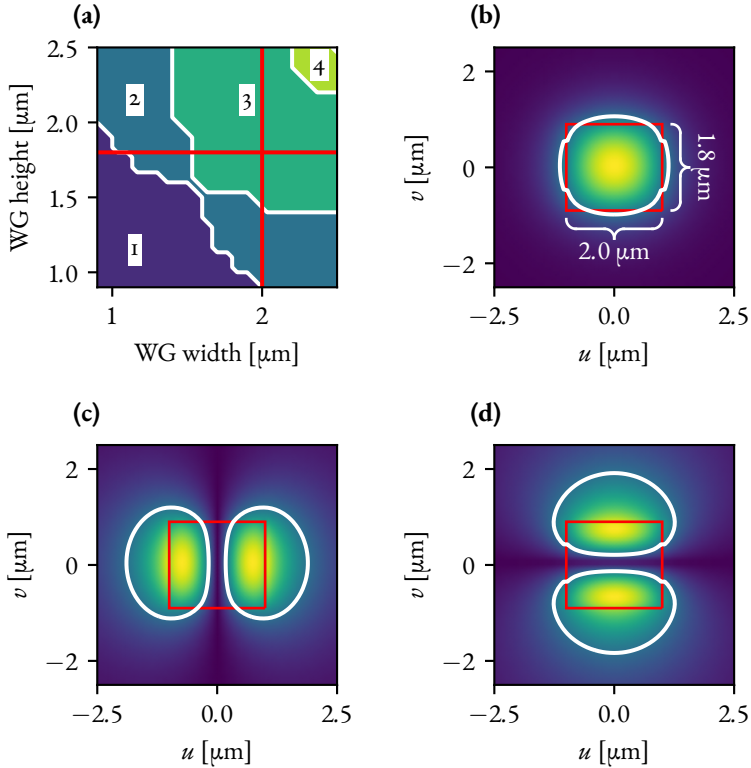
Fig. 2.6: Number of guided modes with horizontally (parallel to u-axis) oriented electric field and associated exemplary electrical fields. **(a)** Number of guided horizontal modes for different PWB cross-sections (n_{core} = 1.53, n_{clad} = 1.36, λ_0 = 1550 nm). The minimal cross-section which still remains mechanically stable (2.0 µm × 1.8 µm) is indicated by red lines. **(b)-(d)** Dominant electric field for all guided modes of a waveguide with 2.0 µm × 1.8 µm cross-section. The white line indicates the contour at which the field has dropped by a factor of e^{-1} compared to its peak value in the waveguide core.

the order of 1.4 µm × 1.4 µm. Due to the axial elongation of the voxel, horizontal waveguides with such small cross-sections cannot be reliably fabricated using current technology. It is conceivable that future materials or lithographic advances such as stimulated emission depletion (STED) inspired lithography [41, 64] will enable such small dimensions. If the chosen cross-section is kept, it only becomes single-moded if the cladding refractive index is above $n_{\text{clad}} = 1.43$. However, then only bends above 80 µm bend radius would exhibits less then 0.5 dB radiation loss per 90° arc for such a high refractive index of the cladding material. Narrower bends such as a 50 µm bend would incur radiative losses of 3 dB per 90° bend arc. Unless smaller waveguides can be fabricated, or the minimum bend radius can be increased, few-moded PWB have to be preferred over single-mode PWB with strong radiative losses even in relatively weak bends. In any case, care has to be taken to avoid exciting these higher-order modes by adiabatic transition towards these bends.

Step 4: Constraints on waveguide path.   One particular design freedom of PWB is the path the PWB waveguide follows. Virtually any free-form path may be chosen, if it does not exceed the limit on the waveguide curvature imposed by the radiation losses in the waveguide bends or overly excites higher-order modes. In planar PIC design, the waveguides are typically composed of straight sections and arc sections, all conforming to the photonic design rules of the PIC platform. The same principle can be employed in the design of PWB. In addition to the aforementioned straight and arc segments, basis splines [65] are of particular interest, since they can be used to connect two points in 3D space by a smooth line. The position of the spline control points can be used as straightforward parameters in a numerical optimization. If possible, such an optimization should minimize the expected loss of the PWB. Unfortunately, the optimization process can only be run once the position of the coarsely position PIC is found and just before printing the PWB. Any time spent on optimization prolongs the total fabrication time of the PWB. The prediction of the PWB loss for a given path is hence desirable. Efficient loss estimators are still an active field of research which is currently being explored by the

Department of Mathematics and the Department of Physics at KIT. One possible solution for loss estimation, published in [J16], is the segmentation of the PWB in small arc segments of constant curvature. For each arc segment, the radiation loss is numerically estimated by a mode solver, similar to the result shown in Figure 2.5.

However, even the best path optimization is of not use if the path is not followed by the fabricated PWB. It turns out that the shrinkage of acrylate-based polymer material is significant and distorts the PWB path. Since the PWB is fixed at both ends, it will be deformed. There is currently no known model to predict the PWB deformations. Therefore, even if a precise loss estimator were available, it is not of much direct use. In this dissertation, direct optimization of the estimated PWB loss was therefore not employed. Instead, a very simple optimization strategy was chosen, where the trajectory was optimized such that the smallest local bend radius over the PWB path was maximized. More details on previous attempts on PWB path optimization can be found in [66].

Once the path $\mathbf{r}\left(t\right) = \left[x\left(t\right), y\left(t\right), z(t)\right]^{\mathrm{T}}$ of the PWB has been decided on, the waveguide cross-section is swept along the path to define the 3D shape of the PWB. The cross-section may be variable along the path to allow for mode converters at the beginning and ending of the PWB path. Note that the orientation of the moving coordinate system frame along the PWB path can be freely chosen. The coordinate system is often described by the normal basis vectors $\mathbf{u}\left(t\right)$, $\mathbf{v}\left(t\right)$ and $\mathbf{t}\left(t\right)$, where $\mathbf{t}$ is tangential to the curve at $\mathbf{r}\left(t\right)$ and the vectors $\mathbf{u}\left(t\right)$ and $\mathbf{v}\left(t\right)$ describe the cross-section orientation. One popular choice is to select the local frame such that $\mathbf{u}$ is always parallel to the xy plane. However, such a choice of local coordinate systems does not result in a rotation minimized PWB and is ill-defined for vertical bonds, such as the one encountered for HCSEL-to-SiP connections. Throughout this thesis, all bonds therefore employ rotation-minimizing coordinate systems, generated by the double reflection method [67]. This method also allows to constrain the start and end rotation of the coordinate system, such that the wirebond is perfectly oriented relative to tilted devices. By convention, the $\mathbf{u}$ vector points predominantly parallel to the xy plane.
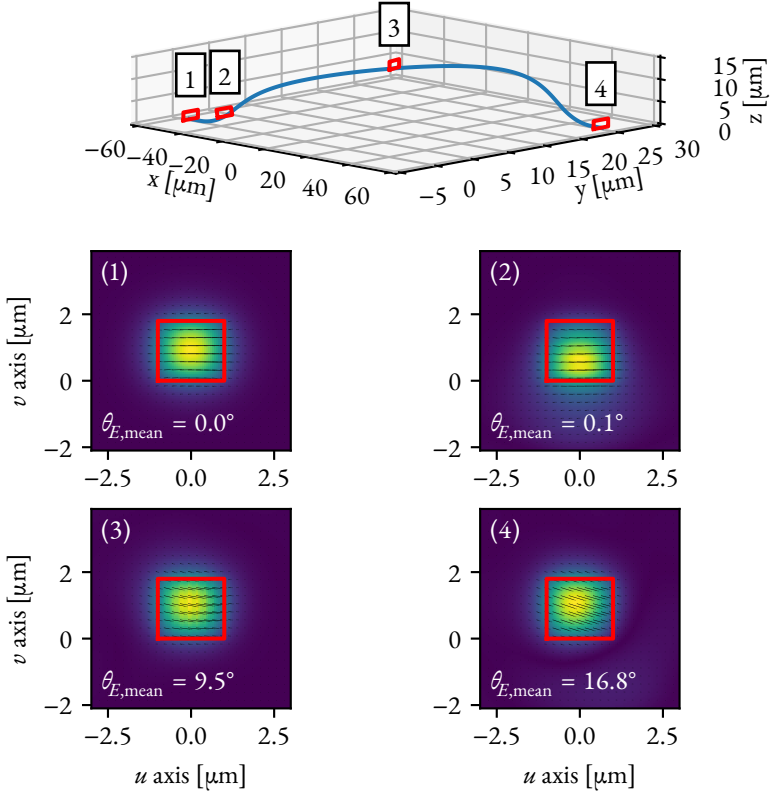
Fig. 2.7: Complex 3D PWB path and the vectorial electric fields at different positions in the local coordinate system of the PWB along the path. The PWB connects two points separated by $\Delta x = 100\,\mu\text{m}$ and $\Delta y = 25\,\mu\text{m}$. No substrate material was included in the simulation. The minimal occurring bend radius of the PWB path is $29.3\,\mu\text{m}$. The fundamental mode is injected in the waveguide at **(1)**. The PWB first follows an upward bend to leave the substrate plane ($z = 0$), where the field is pushed to the bottom of the waveguide cross-section **(2)**. Afterwards, the PWB follows a full 3D path to the target location. At the end of the segment, a slight polarization rotation is observed **(3)**. Finally, the PWB follows a downward bend to move back to the substrate plane. The final field **(4)** shows considerable polarization rotation compared to the initial state amounting to $\Delta\theta_{E,\text{mean}} = 16.8°$. Assuming that only the horizontal field of the initially injected mode is acceptable, only approximately $\left|\cos\Delta\theta_{E,\text{mean}}\right|^2 = 0.957$ are transmitted, corresponding to $-0.43\,\text{dB}$. The simulated overall total transmission of the PWB to the horizontal mode is $-1.6\,\text{dB}$. The total transmitted power ratio over all modes is $-0.87\,\text{dB}$, dominated by radiation loss.

One of the initially stated requirements for PWB connections was that the polarization should be maintained even if the PWB follows a 3D path. Just as with SMF, the polarization of a waveguide with degenerate fundamental modes is not maintained when subjected to bends. Such a bend will introduce mechanical stress and adds a small amount of birefringence along the axis of the bend which is usually not parallel or orthogonal to the injected polarization state. While in the bend, the modes will experience a difference in phase velocity, rotating the state of polarization. This principle is commonly exploited in fibre-based polarization controllers, but is not desired in a PWB. Polarization maintaining (PM) fibres solve this problem by employing a strongly asymmetric waveguide structure such that the birefringence overcomes the effects of the bend[8]. The chosen PWB parameters only result a slightly asymmetric waveguide, and therefore only a small difference in effective refractive index between the two orthogonally polarized fundamental modes exist. Any PWB of the chosen parameters which exhibits a path with bends neither orthogonal nor parallel to the local polarization will rotate the polarization state of light. It is instructive to visualize the effect for a PWB which follows a full 3D path with tight bends. Figure 2.7 depicts such a path of a PWB bridging two points separated by a 100 μm axial offset and a 30 μm lateral offset. Such offsets represent worst-case conditions for manually assembled multi-chip modules. The PWB cross-section was chosen to correspond to the aforementioned parameters of 2.0 μm × 1.8 μm with a refractive index of $n_{core} = 1.53$, $n_{clad} = 1.36$ and at a central wavelength of $\lambda_0 = 1550$ nm. Figure 2.7 depicts the electric field strength and orientation at four positions along the PWB. Initially, the injected field is in a horizontally polarized fundamental mode. As the

---

[8]Note that different designs can be used to create birefringence in a fibre. The fibre waveguide may be geometrically asymmetric, or have an asymmetric refractive index profile. Often, mechanical stress is used to induce permanent stress birefringence using 'rods' of another material within the cladding material.

light follows the waveguide, it is pushed to the outside of the waveguide at the bends, and a portion of the field is radiated away, incurring 0.87 dB radiation loss in total. At the exit, the field ends up rotated by $\Delta\theta_{E,\text{mean}}$ = 16.8°. The total transmitted power loss to the horizontal fundamental mode at the output is 1.6 dB.

In practice, many PWB paths predominantly lie in a single plane which is parallel or orthogonal to the electric field orientation, such that the effect of polarization rotation will be less significant. Furthermore, it is also often the case that at least one device is connected by a PWB that does not require careful control over polarization, e.g., when connecting to a SMF or a photodetector. In such a case, the insertion loss of the simulation in Figure 2.7 is only 0.87 dB, and is dominated by radiative losses due to the narrow waveguide bends.

2.3.2 Inverse taper for broadband coupling to SiP devices

A common approach to couple light from an integrated optical circuit to a PWB employs a double taper approach [3] where the integrated waveguide is embedded into a polymer taper structure, see also Figure 2.8. This approach is primarily chosen for its ability to interface to chips using high index contrast photonic integration platforms such as silicon photonics (SiP). For such platforms, the extremely small intrinsic mode field diameters often pose a significant challenge when interfacing PIC with the outside world optically. Today, commercial SiP chips are usually fabricated using multiple patterning lithography on a 248-nm KrF excimer laser CMOS line. As a result, minimum allowed taper tip sizes are typically around 130 nm. In case of an adiabatic taper, the overlap integral between the mode at the silicon tip and the fundamental mode of the polymer waveguide into which the Si waveguide is incorporated defines the transition loss into the PWB. Figure 2.9 shows the waveguide mode of the PWB on silicon oxide, and the effect of the taper tip widths and its effect on the overlap integral. It can be seen that smaller tip widths are strongly preferred. SiP foundries [68] are currently moving to higher resolution nodes using ArF 193-nm excimer laser immersion lithography, and therefore tip

Side view

$R \geq 30\ \mu m$

Overlapping inverse taper

Silicon nanowire

$0.22\ \mu m$

$1.8\ \mu m$

$0.5\ \mu m$

$2.0\ \mu m$

Silicon oxide

Top view

Overlapping inverse taper

$0.8\ \mu m$

$0.5\ \mu m$

$60\ \mu m$

$2.0\ \mu m$

marker

Silicon oxide
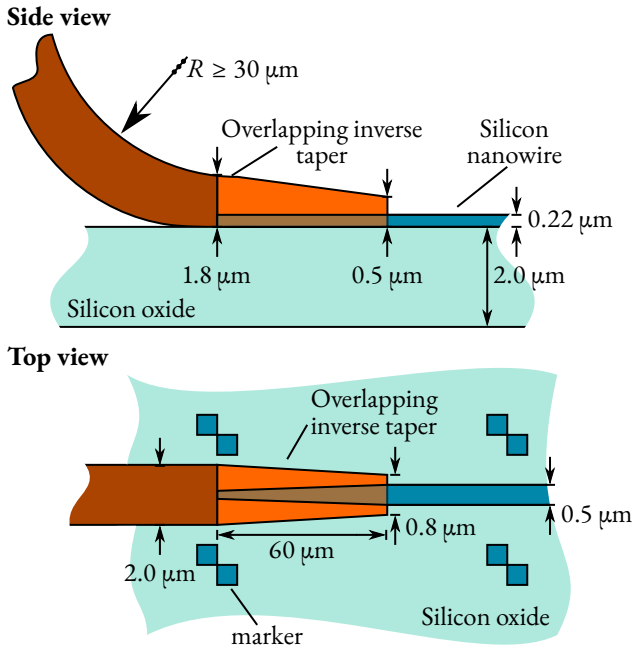
Fig. 2.8: Photonic wire bond interface to tapered silicon waveguide. Side and top views of the transition to the SiP waveguide. The polymer PWB taper starts with a rectangular $2.0\ \mu m \times 1.8\ \mu m$ cross-section of the PWB WG section, which is linearly converted to a final width of $0.8\ \mu m$ and a height of $0.5\ \mu m$ along a length of $60\ \mu m$. Alignment markers are used to exactly locate the position of the coupling interface.

sizes down to 90 nm should pose no problems. In fact, the research organization *CEA-Leti* is currently advertising feature sizes down to 90 nm. Also note that over-etching of the tips often results in smaller than designed tip width, which helps to increase the coupling efficiency. This is in stark contrast to edge couplers, where any deviation from the designed mode field diameter will result in excess loss. A comprehensive treatment of coupling PWB to inverse tapers can be found in [69].

When PWB are attached to SiP inverse tapers, they are directly placed on top of the buried silicon oxide (BOX) surface of the chip, see Figure 2.8. However, the PWB is usually routed away from the chip plane and therefore has to detach from the chip surface, see also Figure 2.8. When the PWB is detached from the silicon oxide chip surface, some light may leak into the BOX due to its higher refractive index of $n_{\text{BOX}} = 1.44$ compared to the cladding refractive index of $n_{\text{clad}} = 1.36$. Figure 2.10a displays the loss encountered by the PWB waveguide section which is routed away from the surface of the silicon photonic chip in a 90° arc. For small arc radii the encountered losses are predominantly caused by radiation loss in the tight bends, while a larger bend radius reduces the encountered loss for a standard 2.0 μm wide waveguide, as indicated by a red rectangle, to below 0.3 dB. The excess losses caused by the leakage into the BOX are readily determined by comparing two similar simulations – one where the BOX is included, and another where the BOX is replaced by a homogeneous cladding material. The excess loss caused by BOX leakage is shown in Figure 2.10b and amounts to approximately 0.2 dB – independent of the arc radius. Additionally, the width of the waveguide might be increased locally to reduce the amount of field inside the BOX substrate and subsequent leakage. However, it can be seen in Figure 2.10 that no significant improvements can be achieved over the already chosen standard width.

One detail specifically concerns the fabrication of PWB on silicon waveguides: The high intensity of the lithography laser allows free carrier absorption in the silicon and subsequent heating when hit by the lithography laser beam. The heating of the silicon waveguide causes local vaporisation of the resist material directly surrounding it, and results in small voids and subsequent excess loss in the coupling structure.
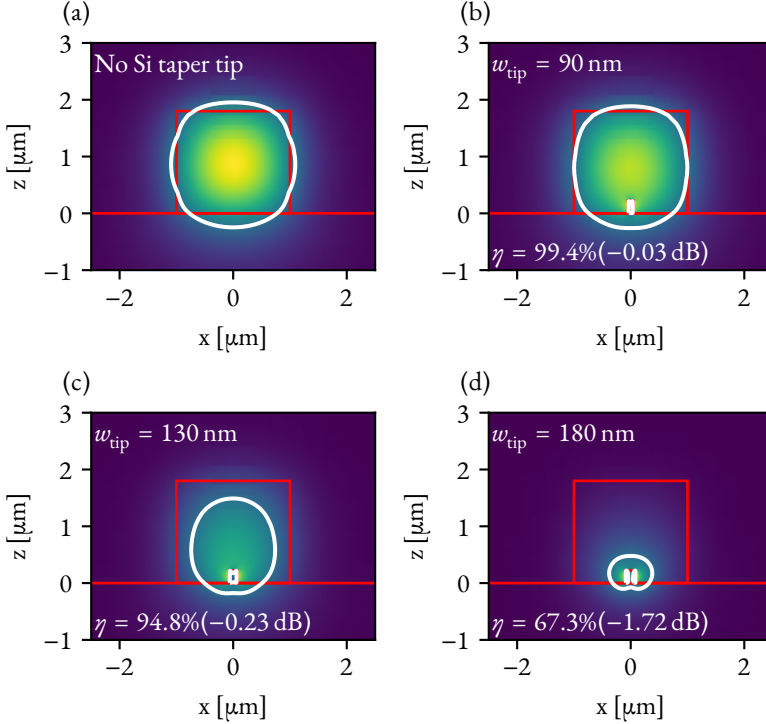
Fig. 2.9: Electrical field of the guided modes of the tip of the inverse taper section and their respective coupling efficiency. **(a)** Undisturbed eigenmode of $2.0\,\mu\text{m} \times 1.8\,\mu\text{m}$ PWB on silicon oxide for $\lambda_0 = 1550\,\text{nm}$. The waveguide is single-moded due to the higher refractive index of the oxide relative to the cladding material. **(b)-(d)** Electric field of the mode at the silicon taper tip for different tip widths and a tip height of $h_{\text{tip}} = 220\,\text{nm}$. In case of adiabatic tapering and negligible side wall roughness, the overlap integral η with the undisturbed mode field represents the loss of the silicon waveguide to PWB transmission. Additional losses my arise from the PWB leaving the silicon oxide surface of the chip. The white line indicates the contour at which the field has dropped by a factor of e^{-1} compared to its peak value.
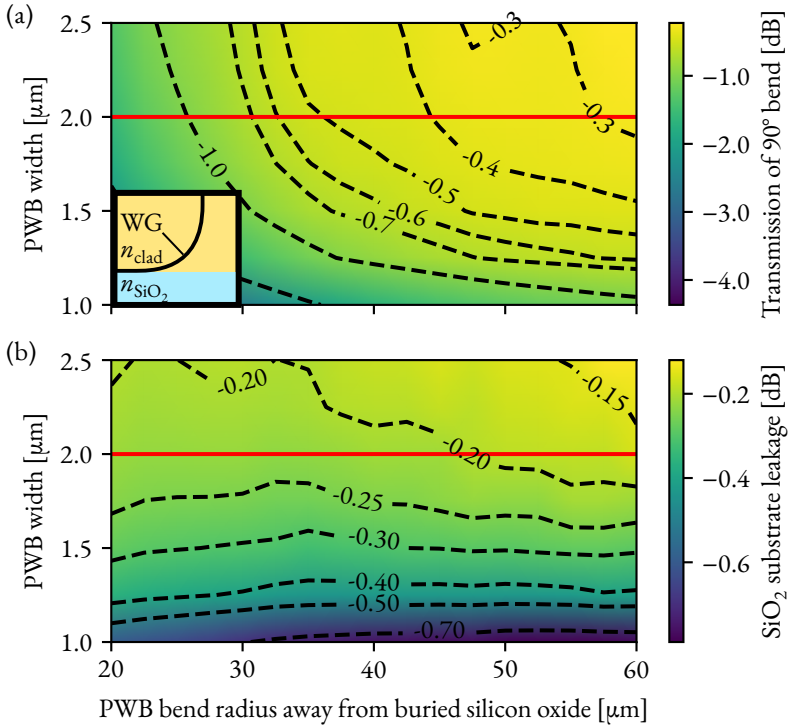
Fig. 2.10: Loss analysis for PWB routed away from a silicon oxide (n_{SiO_2} = 1.44) chip surface in a 90° arc. Apart from the oxide layer, the PWB is surrounded by cladding material (n_{clad} = 1.36). The width w of the PWB is swept while the height is kept constant at 1.8 μm. **(a)** Total losses including radiation due to bends, leakage into the silicon oxide layer, multimode excitation and modal mismatch at the straight waveguide sections adjacent to the bent section. For the default PWB width of 2.0 μm, a minimal arc radius of 50 μm should be kept to avoid excessive losses. **(b)** Excess loss compared to homogeneous cladding caused by field leakage into the buried silicon. Note that the excess loss is mostly independent of the bend radius and further increasing the PWB width beyond the standard 2.0 μm only marginally decreases the leakage into the oxide layer.

In our experiments, we therefore reduce the lithography dose whenever the voxel overlaps with the silicon waveguide. Coupling to a PWB by an inverse taper of other material, such as silicon nitride [46] does not require any such precautions, since silicon nitride is a wide-bandgap ceramic [70].

2.3.3 Coupling to surface- and edge-emitted mode fields

Many integrated photonic devices emit light normal to their top surface or to the edge faces of the chip. The latter is usually referred to as edge coupling or edge emitters in case of light sources [13, 15]. PWB can be directly attached to such devices but may require mechanical support structures to increase adhesion to the device facet. Of particular interest are InGaAsP distributed feedback (DFB) lasers which can be used as an efficient single-frequency light sources at standard optical communication wavelengths to supply silicon photonic devices. Figure 2.11 depicts schematic side views of the employed PWB coupling schemes to edge- and surface-emitting lasers. Horizontal-cavity surface emitting lasers (HCSEL) are similar in operation to their more common edge-emitting counterparts and include an additional etched redirection mirror. The mirror uses total-internal-reflection (TIR) to redirect the light such that it exits in normal direction to the chip surface. This mirror can be etched by a wafer-level process, thereby adding TIR mirrors to many lasers at the same time. A PWB can be connected to either type of laser. In both cases, the laser chips used in this dissertation feature on-chip mode converters which emit circular mode fields in the order of 3 µm, which is larger than the mode field size of a PWB. Mode converters in the form of tapered waveguides provide adiabatic conversion. At the laser side, the taper cross-section is matched to the mode of the laser edge coupler. The PWB cross-section is then adiabatically tapered to the size of the PWB waveguide cross-section. Both approaches were successfully demonstrated, see Ref. [4] and [50] for further details. Both publications employ the methods developed in this dissertation, using confocal imaging in conjunction with computer vision to detect the coupling interfaces of the laser.
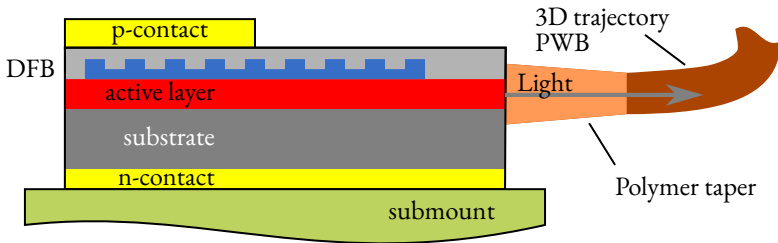
(a) Side view drawing of an edge emitting DFB laser diode connected to a PWB. A polymer taper structure converts the emitted mode to a mode guided by the PWB waveguide section, see also [4] for more details.
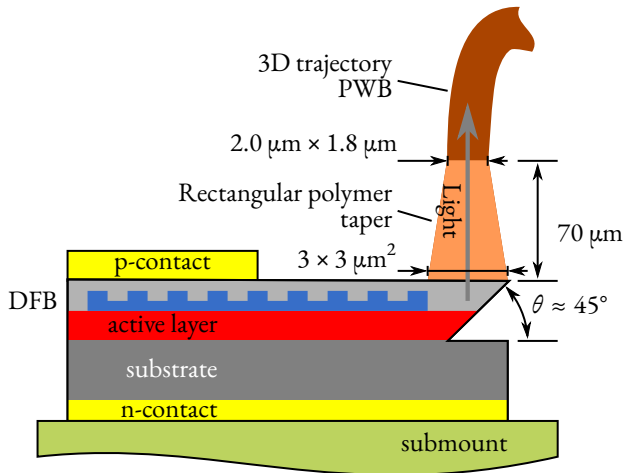
(b) Side view of the photonic wire bond interface to horizontal-cavity surface-emitting laser (HCSEL) lasers. In contrast to the above realization, the HCSEL includes of an etched 45° total-internal-reflection (TIR) mirror to deflect the light to the surface-normal direction at the end of the in-plane InGaAsP DFB laser cavity. The light is then captured and converted by a rectangular polymer PWB taper. The polymer taper structure adiabatically converts the mode by tapering the cross-section from a 3 μm × 3 μm square at the HCSEL emission window to the rectangular cross-section of the PWB of 2.0 μm × 1.8 μm over the length of 70 μm. More details on the HCSEL-PWB interface can be found in [50].

Fig. 2.11: Schematic side views of PWB to edge and surface connecting laser chips.
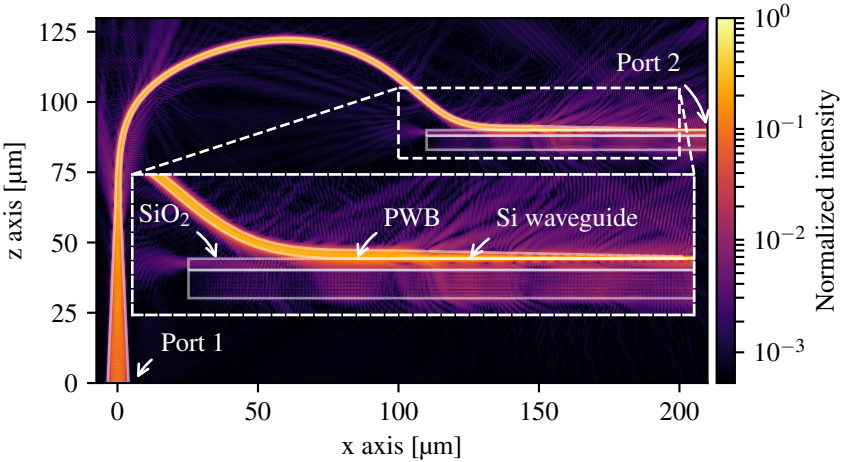
Fig. 2.12: Numerical verification of a HCSEL-to-SiP PWB connection. Calculated normalized intensity of the PWB. Simulations were performed using a vectorial finite-integration technique [71]. Light is launched into Port 1, which is located at the bottom of the PWB input taper connected to the HCSEL, and Port 2 extracts the power guided by the fundamental mode of the SiP WG. Losses are mainly caused by the transition between the PWB and the Si waveguide, indicated by field portions that are radiated away from the waveguide structure (see inset). The insertion loss amounts to approximately 0.49 dB and is flat over the entire simulated vacuum wavelength range from 1530 nm to 1580 nm, see also [50] for further details.

The coupling between such a laser and a silicon photonic device can be simulated using a commercially available numerical solver [71], see Figure 2.12. The simulation includes a complete HCSEL-to-SiP chip connection. The PWB follows a planar path with the electric field oriented orthogonal to the symmetry plane (zx-plane in Figure 2.12). This allows the simulation to exploit the mirror symmetry, thereby reducing the simulation complexity. The simulation uses the refractive indices and waveguide dimensions described in Section 2.3 (i.e., 2.0 µm × 1.8 µm, n_{core} = 1.53, n_{clad} = 1.36, λ_0 = 1550 nm). Port 1 is located at the start of the PWB input taper connected in place of the HCSEL. The fundamental mode of the input taper is launched at Port 1, emulating the output of a HCSEL. Port 2 is placed at the end of Si strip waveguide and the optical power transferred to the intrinsic quasi-TE mode of the silicon strip waveguide is extracted to determine the coupling efficiency. Note that this simulation does not consider any scattering loss caused by surface roughness or any modal mismatch between the mode field at the HCSEL facet and the launched excitation field. The size of the input taper was chosen such that it matches the measured MFD of 3 µm for HCSEL emission. The plot in Figure 2.12 shows the normalized intensity distribution obtained from the simulation at a vacuum wavelength of 1553 nm. The simulated insertion loss from Port 1 to Port 2 amounts to approximately 0.49 dB and is flat over the entire simulated vacuum wavelength range from 1530 nm to 1580 nm. The dominant contribution to the loss originates from the transition from the PWB to the Si waveguide, indicated by radiated field patterns that propagate away from the Si waveguide, see inset of Figure 2.12. In contrast to this, the bends of the PWB waveguide section do not cause much loss.

2.4 Micro-lenses

Another optical element which can be directly fabricated using multi-photon lithography are micro-optical elements, in particular micro-lenses. Complex objectives with multiple optical surfaces for imaging, directly printed on camera sensors were shown by Gissibl and coworkers [19]. Recently, the same technology was demonstrated [18] to dramatically simplify optical assembly, where the technologies originally designed for PWB in this dissertation were applied to the aligned *in situ* fabrication of micro-optical elements to optical chips and devices. In optical assemblies, micro-lenses are typically used to collimate highly divergent beams exiting integrated photonic devices. Assuming that the micro-lens can be fabricated directly to optical interfaces with high precision, the collimated beam enables significantly larger lateral alignment tolerances. It goes without saying that relaxing translational tolerances will tighten the angular tolerances, such that a good compromise must be found. This aspect is further investigated in Appendix C.1. The 1 dB lateral alignment tolerance of a rotational symmetric Gaussian beam is given[9] by $d_{1\,\mathrm{dB}} = \sqrt{1/10 \times \ln 10} \times w_0 \approx 0.24 \times \mathrm{MFD}$. In practice, passive lateral alignment tolerances down to 5 μm are typically stated as an optimum [13], below which the mechanical requirements on the alignment machine significantly increase, whereas angular errors typically play only a minor role. Passive optical assembly therefore requires beams of MFD above 30 μm. When printed directly onto device facets, such micro-lenses typically feature one optical surface only. Appendix C.2 investigates an analytical solution for such simple collimating lenses using transfer matrix analysis [72] for Gaussian beams, which can be used as a starting point for optimizations.

Micro-optical elements typically collimate highly divergent beams, or are used to focus beams to small spots for coupling into integrated devices, see [J5], [J13] and [J17] for details on 3D printed lenses for optical coupling. While ray-optical methods are of limited use, wave-optical modelling beyond the approximation of thin phase

---

[9]A comprehensive treatment on the coupling efficiency of Gaussian beams can be found in the appendix, see Appendix C.1 and especially Eqs. (C.1.26) and (C.1.19).

elements and paraxial approximation is often required. Fully vectorial rigorous methods [71] can provide very exact simulation results, but they are typically very slow, and allow only the simulation of very small optical systems. Simulation volumes of a few tens of micrometres can already take days to simulate, such that these methods can be used for verification, but not for the optimization of optical systems. Given that MPL can be used to produce millimetre scale optical systems with sub-micrometre precision, other simulation methods are required.

A possible candidate for the efficient simulation of optical elements is the wave propagation method (WPM), first proposed by Brenner in 1993 [73]. It overcomes the limitations, namely the paraxial approximation, of the standard beam propagation method (BPM), and has also been extended to include vectorial components [74]. Given a monochromatic field of the form

$$\mathcal{E}\left(x, y, z\right) = E\left(x, y, z\right) \mathrm{e}^{i\omega t}, \tag{2.4.1}$$

it can be propagated along the z direction in a small slice of length Δz through an inhomogeneous medium $n(x, y, z)$ such that the wave $E\left(x, y, z + \Delta z\right)$ after the slice is given by:

$$E\left(x, y, z + \Delta z\right) = \frac{1}{2\pi} \int \tilde{E}\left(k_x, k_y, k_z\right) e^{-ik_z\left(k_x, k_y, x, y\right)\Delta z} \mathrm{e}^{-i\left(k_x x + k_y y\right)} \mathrm{d}k_x \mathrm{d}k_y \tag{2.4.2}$$

$$k_z\left(k_x, k_y, x, y\right) = \sqrt{k_0^2 n^2\left(x, y, z + \Delta z/2\right) - k_x^2 - k_y^2} \tag{2.4.3}$$

$$\tilde{E}\left(k_x, k_y, z\right) = \mathcal{F}_{x,y}\left\{E\left(x, y, z\right)\right\} = \frac{1}{2\pi} \int E\left(x, y, z\right) \mathrm{e}^{i\left(k_x x + k_y y\right)} \mathrm{d}x \mathrm{d}y \tag{2.4.4}$$

where $\mathcal{F}_{x,y}$ indicates a two-dimensional Fourier transform. For each slice, the refractive index distribution is assumed to be constant along the propagation direction. The evaluation of the integral for the whole wave is expensive, since k_z depends on x and y position.

Micro-optical systems usually only feature a limited set of refractive indices, such that $n(x, y, z)$ can be decomposed into a finite number M of pairwise disjoint and homogeneous subregions of refractive index n_m. The stencil function $\Theta_{m,z}$ of subregion m at axial position z can then be defined as

$$\Theta_{m,z}\left(x, y\right) = \begin{cases} 1 & \text{if } n_z\left(x, y\right) = n_m \\ 0 & \text{else} \end{cases}.$$
(2.4.5)

The refractive index distribution n_z at position z is then described by the sum over all subregions of homogeneous refractive index n_m weighted by the corresponding stencil function such that

$$n_z\left(x, y\right) = \sum_{m=1}^{M} n_m \Theta_{m,z}\left(x, y\right).$$
(2.4.6)

In this case, it was recently found by Schmidt [75] that Eq. (2.4.2) can be simplified to

$$E\left(x, y, z + \Delta z\right) = \sum_{m=1}^{M} \Theta_{m,z}\left(x, y\right) \mathcal{F}_{x,y}^{-1}\left\{e^{ik_{z,m}\left(k_x, k_y\right)\Delta z} \mathcal{F}_{x,y}\left\{E\left(x, y, z\right)\right\}\right\}$$
$$k_{z,m}\left(k_x, k_y\right) = \sqrt{k_0^2 n_m^2 - k_x^2 - k_y^2},$$

replacing the computationally expensive integral in Eq. (2.4.2) with a Fourier transform which can be quickly evaluated using, e.g., the fast-Fourier-transform (FFT). A derivation of the algorithm can be found in Ref. [76]. For this work, the modified WPM algorithm was implemented using a graphics processing unit (GPU) acceleration which allows massively parallel evaluation of the stencil function $\Theta_{m,z}$ based on an algebraic lens equation. In addition, the Fourier transforms can also be very efficiently evaluated on a GPU [77]. The *arrayfire* software library [78] was used to implement the algorithm.
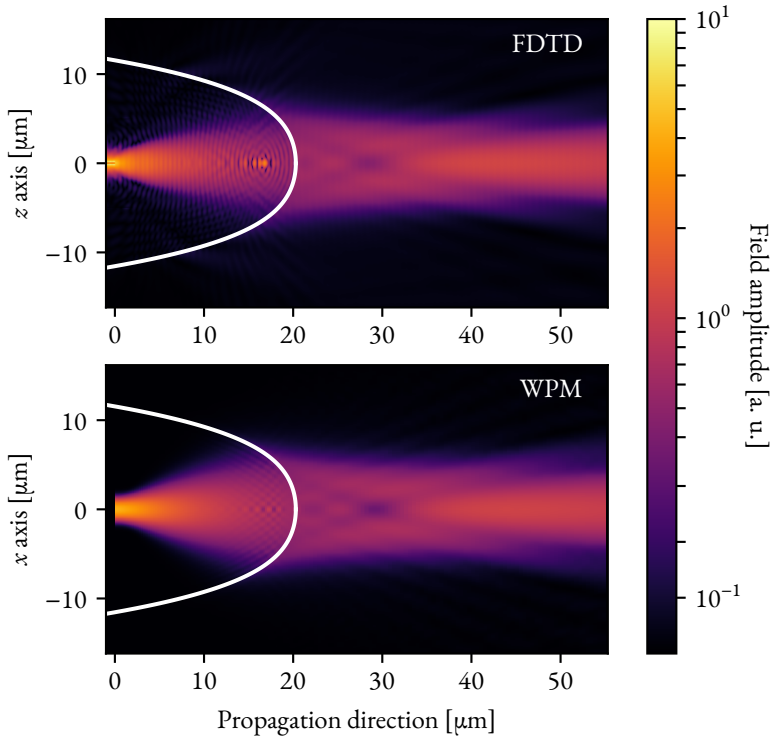
Fig. 2.13: Comparison between a rigorous FDTD simulation and scalar wide-angle wave propagation method (WPM). Highly divergent light is emitted by a silicon taper tip, and collimated by a polymer lens. The WPM simulation took 5 seconds using GPU-based acceleration, while the FDTD simulation took 6 days on 16 CPU cores. Despite this high divergence, the WPM simulations show excellent agreement of the collimated beam with the rigorous FDTD simulation. Note how a standing wave is formed inside the polymer lens due to back-reflection, which is not included in the forward-only direction WPM.

Figure 2.13 shows a comparison between a rigorous finite-difference time domain (FDTD) simulation and the scalar wide-angle wave propagation method (WPM). In the simulation, 1550 nm light is emitted by a silicon taper tip featuring a cross-section of 200 nm × 220 nm. It enters a 3D-printed micro-lens (n_{poly} = 1.56, outline indicated in white) which collimates the light into a free-space beam. The relatively wide silicon tip results in a small and slightly asymmetric mode field diameter of 1.38 μm × 1.55 μm, and consequently results in a highly divergent beam. Despite this high divergence, the WPM simulations show excellent agreement of the propagated beam with the rigorous simulation. Note how a standing wave is formed inside the polymer lens due to back-reflection, which is not included in the forward-only direction WPM. The WPM simulation took 5 seconds using GPU-based acceleration, while the FDTD simulation took 6 days on 16 CPU cores. The simulation speed of the WPM method is so high that it can be directly used for automatic optimization of the lens surface. In this work, it was therefore extensively used to optimize micro-lenses, such a lens attached to PWB, as described in Chapter 5, but was also used in the journal publications [J1], [J2], [J4],[J5] and [J17].

3 Hybrid Multi-Chip Assembly of Optical Communication Engines by In-Situ 3D Nano-Lithography

This chapter reports on optical communication engines realized as hybrid multi-chip assemblies by *in situ* printing of photonic wire bonds. It was first published in *Light: Science & Applications*. The material from the publication was adapted to comply with the layout and structure of this thesis. Associated supplementary information can be found in Appendix A.

Note that Muhammad Billah and the author of this dissertation contributed equally to this publication. Building a multi-chip module (MCM) exceeding the current state-of-the-art performance is a substantial task, requiring contributions of many different people. The experiments were jointly conceived by Muhammad Billah, Tobias Hoose, Christian Koos and the author. The main contribution of the author is the development of the advanced lithography tools required for precise fabrication of the PWB at device facets and the advancement of these processes to a level where MCM with many PWB connections become possible. This includes the automated detection of the photonic chips, the generation of the PWB model based on the detection results, and the eventual conversion of the 3D model to machine commands executed on the lithography system. In addition, it includes the heavy modification of a commercial lithography system for PWB processing. The author

conceived and fabricated the low-loss PWB test structures, evaluated the PWB reliability experiment and developed a fully automated chip characterization setup to characterize the samples efficiently. Sebastian Skacel provided additional data on long term environmental tests of commercially fabricated PWB. The localized protective cladding process was developed by Andreas Hofmann. The physical assembly of the MCM was predominantly done by Muhammad Billah and Tobias Hoose with minor support by the author during fabrication. Muhammad Billah and Tobias Hoose also pre- and post-characterized the modules. The SiP chip design was done by Matthias Lauermann based on schematics jointly developed by Muhammad Billah, Tobias Hoose, and the author. The SiP designs were integrated in a multi-project wafer run by Florian Merget who also discussed process flow related issues with the fabrication facility. The transmission experiment using the IM/DD transmitter module was executed by Muhammad Billah and Juned Kemal, and jointly evaluated by the author who reimplemented a full DSP software stack for direct detection, inspired by code provided by Sebastian Randel. The high-performance SiP modulator design was developed and provided by Florian Merget and Jeremy Witzens. The silicon-organic hybrid modulators of the coherent transmitter module where fabricated by Yasar Kutuvantavida and Clemens Kieninger. The coherent transmission experiment was executed by Muhammad Billah, Juned Kemal and Pablo Marin-Palomo, who also evaluated the data. Ute Troppenz and Martin Möhrle contributed the InP-based components. The author wrote the manuscript of the paper with support by Christian Koos and Wolfgang Freude. The manuscript is partially based on the postdeadline conference contributions [C18] and [C21], accepted by OFC and ECOC 2017, respectively. All authors discussed the data.

[Beginning of Paper [J7].]

Hybrid Multi-Chip Assembly of Optical Communication Engines by In-Situ 3D Nano-Lithography

Matthias Blaicher[1,2,†], **Muhammad Rodlin Billah**[1,2,†], **Juned Kemal**[1], **Tobias Hoose**[1,2], **Pablo Marin-Palomo**[1], **Andreas Hofmann**[3], **Yasar Kutuvantavida**[1,2], **Clemens Kieninger**[1,2], **Philipp-Immanuel Dietrich**[1,2,4], **Matthias Lauermann**[1,4], **Stefan Wolf**[1], **Ute Troppenz**[5], **Martin Möhrle**[5], **Florian Merget**[6], **Sebastian Skacel**[4], **Jeremy Witzens**[6], **Sebastian Randel**[1], **Wolfgang Freude**[1], **Christian Koos**[1,2,4]

[1] *Institute of Photonics and Quantum Electronics (IPQ), Karlsruhe Institute of Technology (KIT), 76131 Karlsruhe, Germany.*

[2] *Institute for Microstructure Technology (IMT), KIT, 76344 Eggenstein-Leopoldshafen, Germany.*

[3] *Institute for Automation and Applied Informatics (IAI), KIT, 76344 Eggenstein-Leopoldshafen, Germany.*

[4] *Vanguard Automation GmbH, 76185 Karlsruhe, Germany.*

[5] *Fraunhofer Institute for Telecommunications, Heinrich Hertz Institute (HHI), 10587 Berlin, Germany.*

[5] *Institute of Integrated Photonics (IPH), RWTH Aachen, 52074 Aachen, Germany.*

[†] *both authors contributed equally to this work*

Three-dimensional (3D) nano-printing of freeform optical waveguides, also referred to as photonic wire bonding, allows for efficient coupling between photonic chips and can greatly simplify optical system assembly. As a key advantage, the shape and the trajectory of photonic wire bonds can be adapted to the mode field profiles and the positions of the chips, thereby offering an attractive alternative to conventional optical assembly techniques that rely on technically complex and costly high-precision alignment. However, while the fundamental advantages of the photonic wire bonding concept have been shown in proof-of-concept experiments, it has so far been unclear whether the technique can also be leveraged for practically relevant use cases with stringent reproducibility and reliability requirements. In this paper, we demonstrate optical communication engines that rely on photonic wire bonding for connecting arrays of silicon photonic modulators to InP lasers and single-mode fibres. In a first experiment, we show an eight-channel transmitter offering an aggregate line rate of $448\,\mathrm{Gbit\,s^{-1}}$ by low-complexity intensity modulation. A second experiment is dedicated to a four-channel coherent transmitter, operating at a net data rate of $732.7\,\mathrm{Gbit\,s^{-1}}$ – a record for coherent silicon photonic transmitters with co-packaged lasers. Using dedicated test chips, we further demonstrate automated mass production of photonic wire bonds with insertion losses of (0.7 ± 0.15) dB, and we show their resilience in environmental-stability tests and at high optical power. These results might form the basis for the simplified assembly of advanced photonic multi-chip systems that combine the distinct advantages of different integration platforms.

3.1 Introduction

Photonic integration is a key technology that has the potential to transform a wide variety of applications, ranging from high-speed communications [79] and ultra-fast signal processing [80] to optical metrology and sensing [81] and further to quantum information processing [82, 83]. At present, most commercial products in the field of integrated optics still rely on discrete assemblies of photonic chips and require

additional coupling elements such as on-chip mode field adapters [84] or rather bulky micro-lenses and redirecting mirrors [85]. Assembling such systems from discrete chips allows combining the complementary advantages of different photonic integration platforms but requires technically complex active alignment techniques, which rely on continuous monitoring of the coupling efficiency while positioning and mounting the devices [86]. These techniques are hence characterized by high cost and low throughput, thereby nullifying most of the inherent advantages offered by wafer-scale mass production of photonic integrated circuits (PIC) [13]. These challenges may be overcome by monolithic integration [87], leading to PIC that combine all elements on a common substrate. However, while monolithic integration minimizes the number of costly inter-chip connections and thus provides the utmost scalability, the functionality and performance of the resulting PIC are often limited by the optical properties of the underlying material system. A prime example in this context is the silicon photonic (SiP) platform [88], which exploits advanced CMOS processing to provide unparalleled scalability but suffers from an indirect bandgap that inhibits efficient light emission in addition to a lack of second-order nonlinearities, which limits the performance of its electro-optic modulators. Moreover, monolithic co-integration of multiple devices on a single die requires complex fabrication processes and thus crucially relies on tight process control to achieve acceptable yield levels. This leads to significant technological overhead, which, in many cases, is in conflict with the heterogeneous and highly fragmented application space of photonic integrated circuits [89].

In this paper, we show that the performance and flexibility of conventional discrete-die systems can be combined with the compactness and scalability of monolithically integrated circuits by exploiting advanced additive nanofabrication techniques. Our approach relies on direct-write two-photon lithography [33] for *in situ* fabrication of three-dimensional (3D) freeform polymer waveguides between coarsely pre-positioned photonic devices. This technique, also referred to as photonic wire bonding [3, 50, 69], does not require active alignment and allows for highly efficient optical coupling between a broad range of waveguide types with vastly different
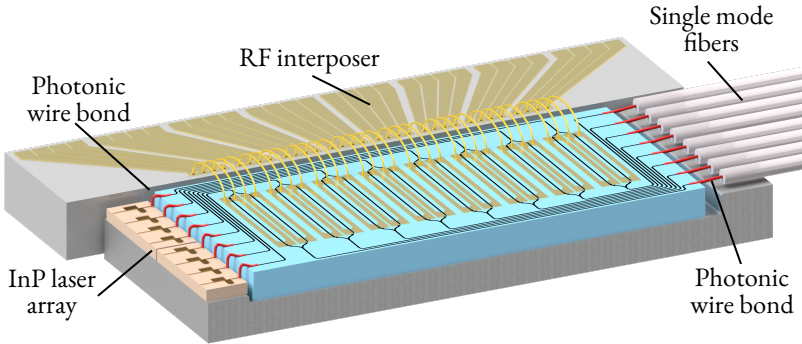
Fig. 3.1: Concept and implementation of hybrid multi-chip modules (MCM) by 3D nano-printing of photonic wire bonds (PWB**).** Illustration of an eight-channel transmitter, realized as a hybrid MCM comprising 3D printed PWB shown in red. PWB allow efficiently connections between photonic integrated circuits (PIC) that are realized on different integration platforms, thereby combining the complementary strengths of the underlying material system. The illustrated transmitter combines efficient InP lasers with electro-optic modulators on a silicon photonic chip. The modulator array is electrically driven via an RF fan-in and connected to an array of single-mode fibres.

mode field profiles in a fully automated process. Building upon previous proof-of-concept experiments that verify the basic applicability of the approach to chip-chip [50] and fibre-chip [3] interfaces, we systematically investigate and demonstrate the reproducibility, reliability, and scalability of the concept. In our experiments, we fabricated 100 densely spaced PWB with an average total insertion loss of 0.7 dB and a standard deviation of 0.15 dB, and we demonstrate their reliability in temperature cycling and damp-heat tests. To prove the practical applicability of our approach, we further realize two different optical transmitter engines that combine arrays of direct-bandgap InP-based light sources with SiP modulators. As a first demonstration, we show an eight-channel intensity modulation/direct detection (IM/DD) transmitter engine that comprises an individual InP laser, a SiP modulator and a fibre pigtail for each channel. This hybrid multi-chip module allows transmission of an aggregate line rate of 488 Gbit s^{-1} over a 10 km-long unamplified optical link [90].

As a second demonstration, we realize a four-channel coherent transmitter module utilizing highly efficient silicon-organic hybrid (SOH) modulators to overcome the intrinsic lack of second-order nonlinearities of the SiP integration platform [91]. Transmitting 56 GBd QPSK and 16QAM signals at a line rate of 784 Gbit s^{-1} over a distance of 75 km, this module provides the highest data rate demonstrated by a SiP transmitter module with co-integrated lasers to date. We believe that these experiments mark an important step towards exploiting the flexibility and design freedom offered by additive 3D nanofabrication in the field of photonic integration.

3.2 Hybrid multi-chip integration by photonic wire bonding

The concept of a hybrid multi-chip module (MCM) using photonic wire bonds is illustrated in Figure 3.1 using an optical transmitter engine as an example. The module combines multiple photonic dies based on different material systems, such as indium phosphide (InP) or silicon-on-insulator (SOI). In the first step, these chips are fixed to a common submount together with an array of single-mode fibres (SMF). This step does not require any high-precision alignment such that cost-efficient high-throughput pick-and-place equipment with rather coarse positioning tolerances of 10 μm or more can be used. Chip-to-chip and fibre-to-chip connections are then realized by 3D freeform photonic wire bonds, the cross-section and trajectory of which can be flexibly adapted to the mode profile and location of the respective optical interfaces. For fabrication of the PWB, on-chip alignment markers are detected by high-resolution 3D imaging and computer vision techniques to extract the exact position and orientation of the various optical components and their interfaces. This information is used for designing the PWB trajectories, thus replacing costly chip alignment by the intrinsic sub-100 nm accuracy of the lithography and imaging system. The PWB are then fabricated by two-photon lithography, offering sub-μm resolution in all spatial directions; see the Methods section for details

of the fabrication process. In our experiments, the PWB feature a core refractive index of n_{core} = 1.52 and a waveguide cross-section of 2.0 μm × 1.6 μm such that the structure is mechanically stable and still small enough for single-mode operation when embedded into a protective low-index cladding material (n_{clad} = 1.36). This configuration allows for sharp bends with radii down to 35 μm, thus enabling flexible waveguide routing in compact multi-chip assemblies [3, 50]. Note that photonic wire bonding allows placing the optical chips side by side, which permits efficient thermal connection to the submount and the underlying heatsink and thus prevents thermal bottlenecks that may arise in stacked-chip assemblies, e.g., when light sources are mounted on top of thick substrates with low thermal conductivity.

The MCM illustrated in Figure 3.1 crucially relies on efficient connections of the SiP chip to both the InP light source and the output transmission fibre, which are shown in more detail in Figures 3.4 and 3.5. The light sources are realized as horizontal-cavity surface emitting lasers (HCSELs), which comprise an InGaAsP-based distributed-feedback cavity in the substrate plane and an etched 45°-mirror that redirects the light towards the substrate normal [92]. Both ends of the PWB feature mode field converters for low-loss coupling to the connected devices, see Figure 3.4. On the laser side, the PWB cross-section is increased to match the larger mode field diameter (3.5 μm) of the HCSEL [50]. A similar structure is used at the fibre-chip interface, as shown in Figure 3.5. Coupling to the SiP chip is accomplished by a double taper structure that consists of a SiP nanowire embedded in a polymer waveguide; see the Methods section and Ref. [50] for details. For low-loss coupling to the SMF, the PWB is tapered to a 14 μm × 14 μm cross-section to match the mode field diameter to that of the fibre. The PWB shown in Figure 3.5 were designed to compensate for a lateral offset of 25 μm between the axes of the optical fibres and the corresponding SiP waveguides. Note that the density of photonic wire bonds along the circumference of the chip can be greatly increased by abandoning the industry-standard pitches of 250 μm that were used for the lasers and the fibres in

our experiments. As shown in the following section, PWB can be realized with pitches of 25 μm, and this could be reduced even further to 10 μm, allowing for 100 PWB per millimetre of chip edge. When combined with micro-lenses, PWB can also be used for optical out-of-plane connections to the chip surface [6].

3.3 Experimental demonstration and discussion

3.3.1 Scalability and stability of photonic wire bonds

In the first experiment, we demonstrate that PWB can provide low-loss optical connections. To this end, we use dedicated test chips that allow for efficient fabrication and testing of statistically relevant numbers of PWB connections using automated fabrication and characterization tools. These test chips consist of pairs of down-tapered SiP strip waveguides [69] that can be connected by on-chip PWB bridges; see Figure 3.2 and Supplementary Fig. S1. The taper tips having a nominal width of 130 nm are spaced by a 100 μm-wide gap, which emulates a typical configuration of a chip-chip interface and is bridged by a free-form PWB. The SiP strip waveguides are 500 nm wide and 220 nm high and are equipped with grating couplers for measuring the transmission spectrum in an automated setup. The test chips were fabricated by deep-UV lithography in a standard CMOS line. Each test chip contains 100 test structures along with reference structures that consist of uninterrupted SiP waveguides without PWB bridges or tapers and that allow for separating the PWB loss from the fibre-chip coupling loss; see Appendix A.1.

The *in situ* fabrication of a PWB is fully automated and took approximately 30 s per connection, where 15 s were spent for interface detection and trajectory routing, and 15 s were used for exposure of the resist. This process can be further accelerated; see the Methods section for details. In the experiment, we fabricated a total of 100 densely spaced PWB bridges with a pitch of 25 μm on a single chip. To extract the insertion loss (IL) of the PWB bridges, we first measure the end-to-end transmission through grating couplers of the connected SiP waveguides at a wavelength of
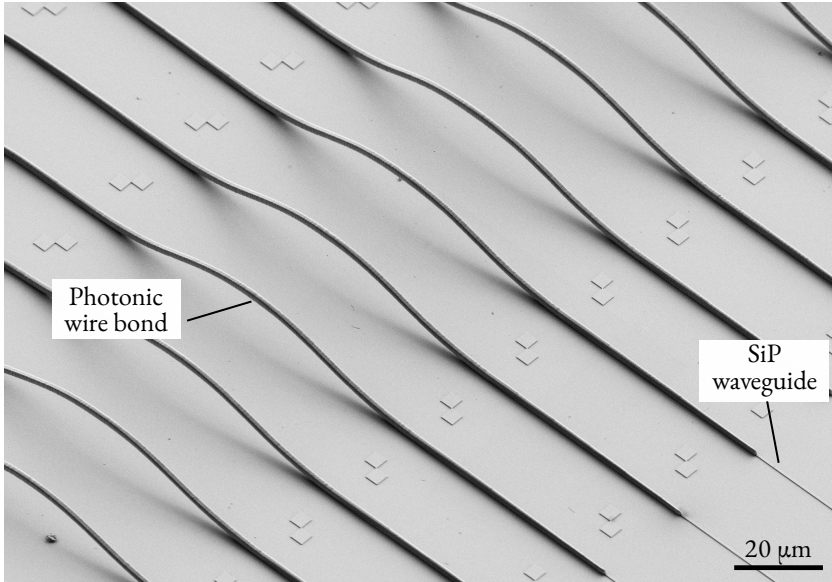
Fig. 3.2: Automated fabrication and environmental stability. (a) Array of densely spaced on-chip PWB test structures. The scanning electron microscope (SEM) image depicts a subset of an array of 100 PWB realized on a dedicated a silicon photonic (SiP) test chip. The PWB bridges connect tapered ends of SiP strip waveguides, separated by 100 nm. High-resolution 3D imaging in combination with computer vision is used for automated detection of the optical coupling with high precision (better than 100 nm) and enables highly reproducible lithographic definition of the freeform structures. The waveguides are finally embedded into a UV-curable low-index polymer (not shown), which acts as a protective cladding and allows adjustment of the refractive-index contrast.

1550 nm and then compare this result to the transmission of the reference structures. We thus obtain the total loss of the PWB connection, comprising the propagation loss in the freeform polymer waveguide as well as the loss of both double-taper interfaces. To achieve single-mode operation of the PWB bridges and to protect the structures, we locally deposit a polymer cladding (n_{clad} = 1.36); see the Methods section for details. The measured ensemble of 100 PWB bridges exhibits an average
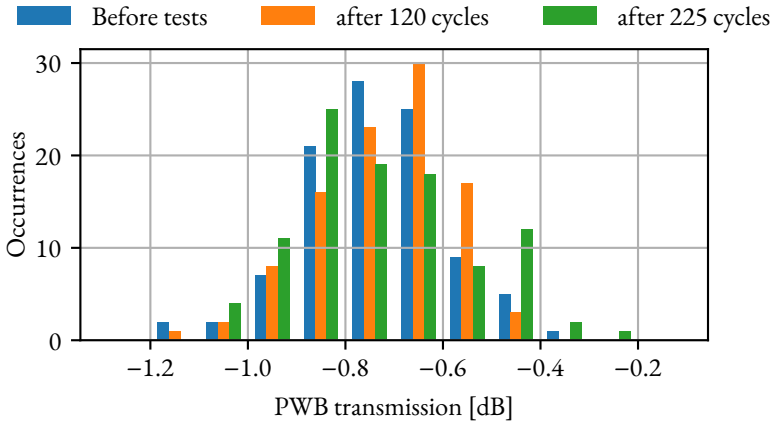
Fig. 3.3: Histogram showing measured insertion losses of 100 on-chip PWB bridges directly after fabrication (blue) as well as after temperature cycling tests, comprising 120 (orange) and 225 (green) cycles. The indicated transmission comprises the propagation loss in the freeform polymer waveguide of the PWB as well as the overall loss of both double-taper interfaces to the adjacent SiP strip waveguides. After fabrication, the PWB bridges exhibits an average insertion loss of 0.73 dB and a standard deviation of 0.15 dB, and the loss of the worst structure was 1.2 dB. These figures are essentially unaffected by the temperature cycles. The slightly different shapes of the histograms are attributed to the fact that the samples had to be removed from the measurement setup for temperature cycling, leading to small changes in fibre-chip coupling efficiency.

IL of 0.73 dB and a standard deviation of 0.15 dB, and the loss of the worst structure was 1.2 dB. Comparable results were obtained by repeating the experiment on other test chips. This clearly demonstrates the excellent reproducibility and yield of fully automated photonic wire bonding processes.

To prove the reliability of the structures under technically relevant environmental conditions [93], the sample is subsequently exposed to multiple temperature cycles, switching between 40 °C and 85 °C. Within the accuracy of our measurements, no performance degradation is found even after 225 cycles, see Figure 3.2. Moreover, the samples do not reveal any signs of degradation, such as delamination of the

cladding material (see Appendix A.1). These findings confirm results from investigations of earlier samples, which we exposed to 600 temperature cycles as well as to damp-heat at 85 °C and 85% relative humidity for more than 3000 h, where we did not observe any degradation either. To test the high-power handling capabilities of the PWB structures, we further subject a different sample of PWB bridges to continuous laser radiation at 1550 nm with increasing optical power levels. In all five tested connections, the SiP waveguides were destroyed by nonlinear absorption at approximately 19 dBm of on-chip power before any damage was observed at the PWB bridges (see Appendix A.1 for details). From these experiments, we conclude that PWB lend themselves to automated large-scale packaging of chips using low-loss connections and that the structures perform well in industrially relevant environments and under power levels that are realistically achieved in silicon photonic assemblies.

3.3.2 Demonstration 1: Eight-channel multi-chip transmitter module for intensity modulation and direct detection

To demonstrate the technical viability of the PWB approach beyond fundamental proof-of-concept demonstrations, we realize a functional photonic multi-chip transmitter (Tx) engine that combines InP-based laser arrays and SiP modulator arrays. In a first demonstration experiment [90], we implement the eight-channel transmitter (Tx) depicted in the conceptual drawing in Figure 3.1, providing line rates of up to 56 Gbit s^{-1} per channel. The module is geared towards transmission in data-centre and campus-area networks with maximum distances of up to 10 km, using technically simple intensity modulation and direct detection techniques.

An optical microscope image of the Tx assembly is shown in Figure 3.6. The assembly contains two arrays of four HCSEL [92], which are connected via PWB to an array of travelling-wave depletion-type Mach-Zehnder modulators [94] (MZMs). A second array of PWB is used to connect the modulator outputs to an array of
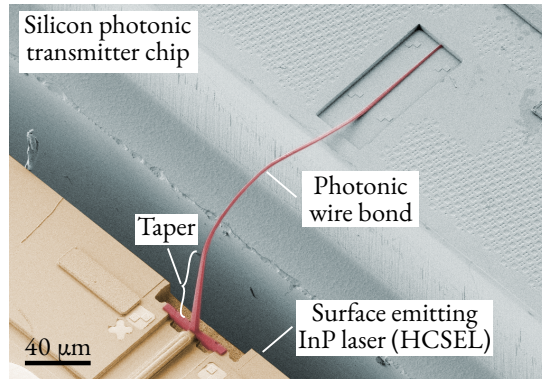
Fig. 3.4: Interface between an InP laser chip and the silicon photonic transmitter chip. The light source is realized as a horizontal-cavity surface emitting laser (HCSEL), consisting of a waveguide-based optical cavity in the substrate plane and an etched 45° mirror that redirects the light towards the substrate-normal direction [50].
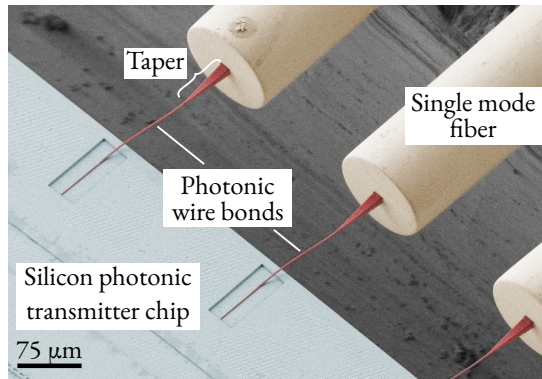
Fig. 3.5: Fibre-to-chip interface. For efficient coupling to the large mode field of the SMF, the PWB are designed to have a larger cross-section towards the fibre facet. The 3D free-form trajectory of the PWB is adapted to the exact position of the corresponding interfaces and thereby replaces high-precision active alignment of the chips.

eight 30 cm-long SMF with connectors at their remote ends. Representative images of the PWB structures are shown in Figures 3.4 and 3.5. The experimental setup for
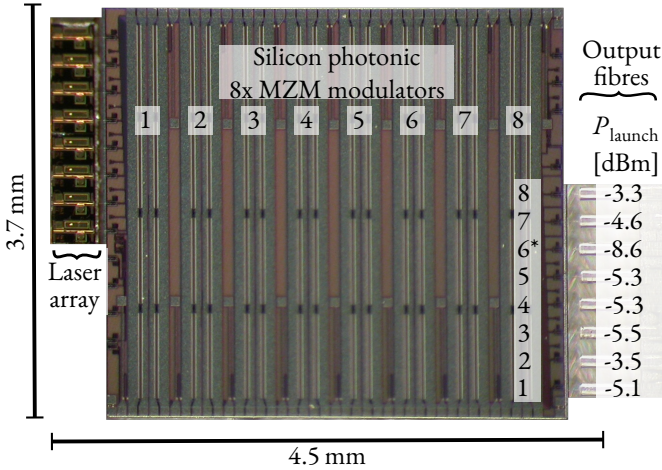
Fig. 3.6: Eight-channel multi-chip transmitter (Tx) module combining InP laser arrays and SiP modulator arrays. The module is geared towards transmission in data-centre and campus-area networks with maximum distances of 10 km, using simple intensity modulation and direct detection techniques. Light microscope image of the Tx assembly, realized according to the concept shown in Figure 3.1. The array of Mach-Zehnder modulators (MZMs) is connected to an array InP-based HCSEL ('Laser array') and to an array of single-mode fibres by PWB (not visible here); see Figures 3.4 and 3.5. The launch powers, measured in the single-mode fibre for maximum transmission of the modulators, are sufficient for transmission over distances typical for data centre and campus area networks, without the need of optical amplifiers. Launch power variations are mainly attributed to non-ideal coupling to and from the SiP chip; see the Methods section for details. Channel 6* contains an additional on-chip 3 dB splitter for testing, which leads to additional loss; see the Methods section.

testing the Tx module is shown in Figure 3.7. The modulators are sequentially driven via microwave probes using a benchtop-type arbitrary waveform generator (AWG) that provides either two-level on-off-keying (OOK) or four-level pulse amplitude modulated (PAM-4) signals. Pre-emphasis is used to compensate for the frequency response of the AWG and the attached RF components. The modulated optical signals are sent either directly to the receiver (Rx) in a back-to-back (b2b) configuration or through 2 km- or 10 km-long SMF. The receiver consists of a photodetector with
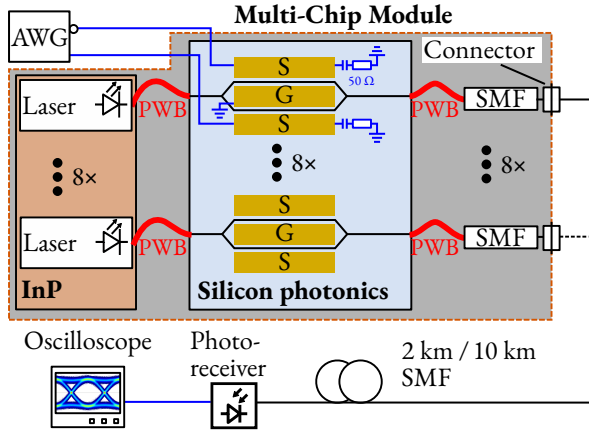
Fig. 3.7: Experimental setup for transmission demonstrations using different modulation formats and distances. An arbitrary-waveform generator (AWG) is used to drive the Mach-Zehnder modulators (MZMs). In our demonstration, the modulators are operated sequentially via an RF probe delivering the drive signal at the input and another RF probe to provide 50 Ω termination at the output. The optical signal is sent through up to 10 km of standard SMF and is detected with a photoreceiver that contains a photodetector along with a high-speed transimpedance amplifier. A real-time oscilloscope is used to capture the electric signals for subsequent offline processing.

an integrated transimpedance amplifier connected to a high-speed oscilloscope that records the electric signal for subsequent offline digital signal processing (DSP). Note that in our experiment, we did not use an RF interposer board that would allow for simultaneous operation of all MZMs, and various channels could hence only be tested sequentially. To confirm that simultaneous operation of all devices would lead to similar results, we measured the electrical cross-talk among unterminated MZMs; see Appendix A.2.1 for details. More details on the transmission experiment and the data processing can be found in the Methods section.

* Extra on-chip 3-dB coupler (MMI) in Ch. 6
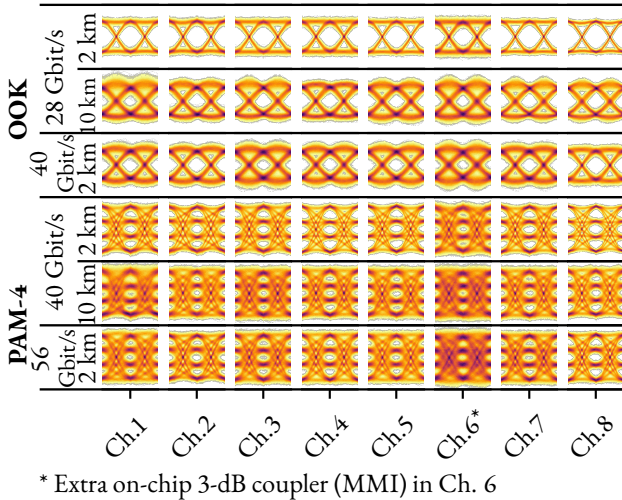
Fig. 3.8: Eye diagrams for transmission over various distances, with different modulation formats and symbol rates. As expected from the launch powers, Channel 8 shows the widest-open eyes, whereas Channel 6 is distorted by noise.

For both modulation formats, OOK and PAM-4, the eye diagrams of each channel in various combinations of line rates and transmission distances of up to 10 km are shown in Figure 3.8, and the associated estimated bit error ratios (BERs) are depicted in Figure 3.9. All observed BERs are below the 7% hard decision forward error correction [95] (HD-FEC) limit. Note that BER < 10^{-5} cannot be reliably measured within our maximum symbol recording length. We therefore estimate the BER based on the measured variances of a Gaussian probability density function at each symbol level; see Supplementary Information S2.2 for details. For PAM-4, simultaneous operation of all channels would result in an aggregate line rate of 488 Gbit s^{-1} and a net data rate of 416 Gbit s^{-1}. The concept would hence lend itself to compact high-speed 400 Gbit s^{-1} modules as specified in various standards and multi-source agreements [96, 97]. For the case of OOK, we demonstrate an aggregate line rate of 320 Gbit s^{-1} over a transmission distance of 2 km with an es-
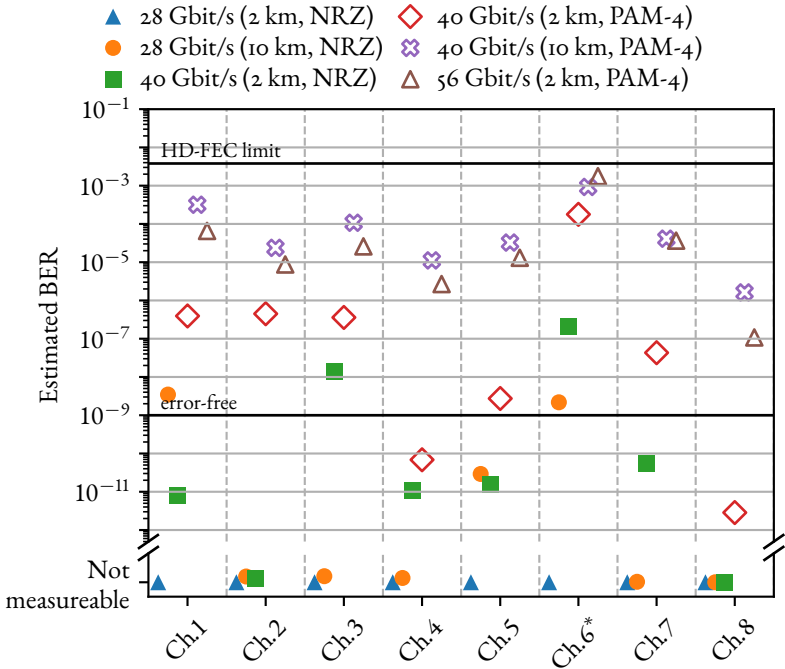
Fig. 3.9: Estimated bit error ratios (BER) for transmission over various distances, with different modulation formats and symbol rates. For all experiments, the BER stays below the 7% HD-FEC threshold. The aggregate module line rate amounts to a 448 Gbit s^{-1}. Results from back-to-back transmission experiments as well as measured BER can be found in Appendix A.2.

timated BER $< 1.0 \cdot 10^{-9}$ for all channels. Note that the current demonstration is a proof-of-concept experiment that leaves room for optimization. As an example, the optical launch power levels measured in the single-mode transmission fibres for full transmission of the MZMs vary between -3.3 dBm and -5.5 dBm, disregarding Channel 6, which is subject to an additional on-chip 3 dB tap; see the Methods section for details. From these results, we estimate insertion losses between 3.6 dB and

5.3 dB per PWB. These loss figures are significantly larger than the numbers found in the scalability experiment shown in Figure 3.3 or in more recent demonstrations of chip-to-chip connections [50]. This is mainly caused by a non-optimum etching process of the SiP chip, which is required to open the oxide windows for providing access to the tapered sections of the silicon waveguides; see the Methods section. The transmission rate could be further increased by replacing the SiP depletion-type MZMs with faster devices based on organic electro-optic materials, which have been demonstrated to support data rates of more than $100\,\mathrm{Gbit\,s^{-1}}$ per wavelength [98] for OOK and $120\,\mathrm{Gbit\,s^{-1}}$ for PAM-4 [99]. In our experiment, the emission frequencies of the HCSEL light sources in each array are spaced by 100 GHz. Instead of using eight separate SMF, a hybrid co-integrated arrayed-waveguide grating (AWG) could extend the functionality of the module to dense WDM transmission through only one SMF. Note that PWB have been demonstrated [69] to exhibit broadband transmission between 1300 nm and 1600 nm such that the concept can be readily transferred to other wavelength bands.

3.3.3 Demonstration 2: Four-channel multi-chip transmitter module for coherent communications

In a second demonstration, we realize and test a hybrid multi-chip transmitter module for coherent communications in metropolitan-area networks and data-centre interconnects. In this module, hybrid multi-chip integration with PWB is combined with hybrid on-chip integration of electro-optic modulators that combine SiP nanowire waveguides with highly efficient electro-optic materials. This so-called silicon-organic hybrid (SOH) [101] approach allows us to overcome the intrinsic lack of second-order optical nonlinearities in the inversion-symmetric diamond crystal lattice of silicon. SOH devices offer voltage-length products $U_\pi L$ of less than [102] 0.5 V mm – more than an order of magnitude below that of conventional depletion-
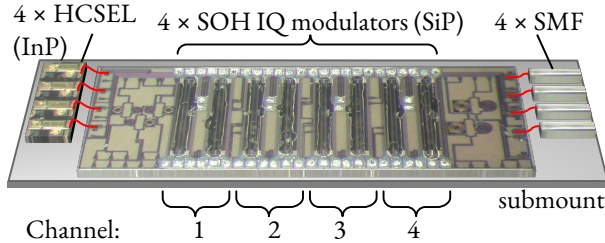
(a) Artist's impression of the multi-chip-module (MCM) consisting of four InP-based HCSEL light sources, an array of four silicon-organic hybrid (SOH) modulators, and four transmission fibres, all connected by photonic wire bonds (PWB). The overall footprint of the complete Tx module amounts to 4 mm × 1.5 mm.
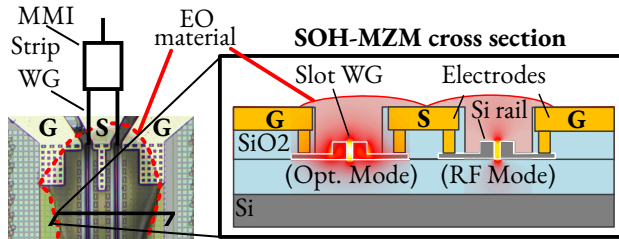
(b) Top view and cross-section of an SOH Mach-Zehnder modulator (MZM). The organic electro-optic (EO) material (red contour) is micro-dispensed after fabrication of the PWB. The MZM consists of two slot-waveguide (WG) phase modulators, driven in push-pull mode by a single coplanar transmission line in ground-signal-ground (GSG) configuration. Within the slot-waveguide phase shifters, the dominant electrical component of the optical quasi-TE mode exhibits a strong overlap with the electrical RF-mode field, resulting in a high modulation efficiency [100].

Fig. 3.10: Four-channel coherent transmitter module combining hybrid integration concepts on chip and package levels.

type devices [103] – and have been shown to support line rates [99] of 100 Gbit s^{-1} for a simple OOK modulation format and symbol rates of up to 100 GBd for 16-state quadrature amplitude modulation [100] (16QAM) at fJ bit^{-1} energy consumption [100].
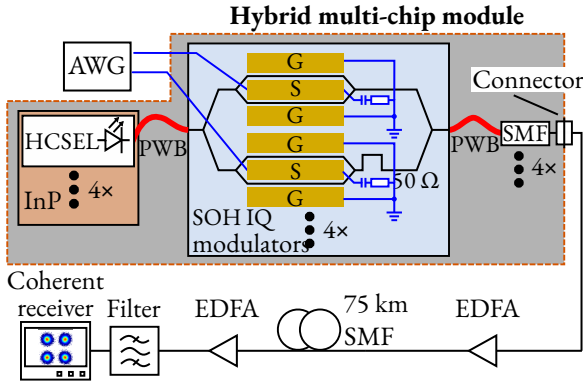
Fig. 3.11: Experimental setup. Each HCSEL feeds an IQ modulator. Electric drive signals for the modulators are provided by an arbitrary-waveform generator (AWG). The optical signal is then amplified, sent through 75 km of standard SMF, and detected by a coherent receiver. A real-time oscilloscope captures the signal for subsequent offline processing; see the Methods section for details.

An illustration of the Tx module is shown in Figure 3.10. The module consists of a SiP chip that comprises four SOH IQ modulators along with the associated optical coupling interfaces and RF contact pads. These modulators are again optically fed by an array of InP-based HCSEL light sources that are placed adjacent to the SiP chip on the same submount. At the output, the SOH modulators are connected to an array of four single-mode fibres for transmission over 75 km. As in the first demonstration, the emission frequencies of the HCSEL are spaced by 100 GHz, and instead of using four separate SMF, hybrid co-integration with an arrayed waveguide grating could extend the functionality of the module to dense WDM transmission through a single SMF.

The IQ modulators are built from pairs of nested SOH MZMs A top view and a schematic cross-section of one MZM are illustrated in Figure 3.10b. Each MZM comprises two SOH phase modulators that are driven in push-pull mode by a single coplanar transmission line in a ground-signal-ground (GSG) configuration. The phase modulators consist of slot waveguides clad with an organic electro-optic (EO)
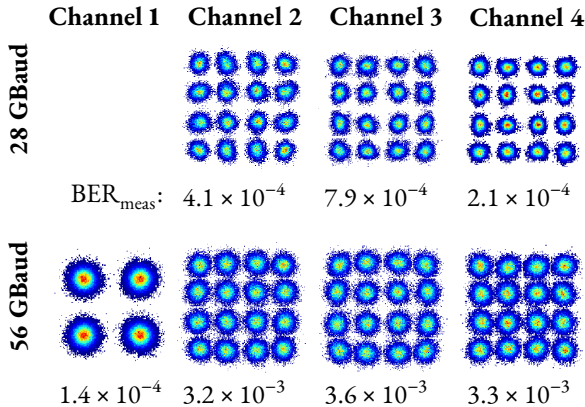
Fig. 3.12: Constellation diagrams and associated measured bit error ratios (BERs) for signalling with 16QAM at symbol rates of 28 GBd and 56 GBd. The performance of Channel 1 was impaired by lower launch power such that only QPSK transmission could be used. All BER values stay below the threshold for hard-decision forward-error correction FEC with 7% coding overhead. The aggregate module line rate amounts to 784 Gbit s^{-1}.

material; see the cross-section in the inset of Figure 3.10b. The slot-waveguide configuration leads to a strong overlap of the fundamental optical quasi-TE mode with the modulating RF field, which is applied via the Si rails of the slot waveguide and the adjacent conductive Si slabs [101]. In combination with the strong electro-optic activity, this effect results in highly efficient devices with low power consumption. The basic SiP waveguide structures are fabricated by a CMOS process, and the organic EO material is deposited in a post-processing step; see the Methods section for details. The π-voltage-length product measured for this module amounts to $U_{\pi}L = 1.3$ V mm. This is larger than the values published in earlier-work [102] since the EO material (SEO100) was chosen for good thermal stability for operation at 80 °C rather than to maximize efficiency.

In our demonstration experiment, the PWB were operated contrary to their design without protective cladding to avoid the risk of covering the electrical on-chip contact pads. This leads to rather high insertion PWB losses, both for the laser and the fibre interface; see Methods for details. Regarding the launch power, Channels 2, 3, and 4 feature similar performance with power levels of up to −11.6 dBm. In Channel 1, the PWB on the HCSEL side is impaired by a dirt particle that permanently attached to the PWB during the fabrication process, which is partially accomplished outside in a normal laboratory environment outside a clean room. This leads to a reduced launch power of only −19.9 dBm and hence to lower transmission performance. Such problems can be avoided by performing all fabrication steps in a clean-room environment as done for samples used in the reliability tests; see Figure 3.2. On these chips, the PWB were directly encapsulated after fabrication and did not show any dirt-related defects. We believe that once the whole transmitter module is assembled and encapsulated under clean-room conditions, contamination by dirt particles will not be an issue. Nevertheless, we demonstrate the functionality of the module in a coherent transmission experiment. To this end, we use the setup shown in Figure 3.11. An AWG is used to drive the IQ modulators through two GSG probes. For each channel, the modulated optical carrier is sent through a 75 km-long SMF. At the receiver, the signal is boosted by an optical pre-amplifier and then coherently detected by an optical modulation analyser and an external-cavity laser (ECL) serving as a local oscillator. Details of the transmission experiment can be found in the Methods section. A summary of the recorded constellation diagrams and the associated BER is shown in Figure 3.12. Channel 4 has the cleanest constellation diagrams, whereas Channel 1 supports QPSK only due to its lower launch power. All BERs are directly measured and fall below the limit of 3.8×10^{-3} for second-generation hard-decision forward-error correction (FEC) with 7% overhead [104]. Details on signal processing and results from back-to-back measurements can be found in the Methods section auf Seite 72 and Appendix A.3. The coherent transmission experiments lead to an aggregate line rate of 784 Gbit s^{-1} and a net data rate of 732.7 Gbit s^{-1}. To the best of our knowledge, this corresponds to the highest values so far demonstrated

with a SiP transmitter module having hybrid integrated lasers. In our transmission experiments, we did not observe any distortions due to frequency fluctuations or excessive phase noise of the optical carriers, although our assembly did not contain any optical isolator between the SiP modulator chip and the InP HCSEL. This is in accordance with previous demonstrations, where the optical linewidths of HCSEL with low-loss PWB connections to SiP chips was investigated [50]. The footprint of the four-channel coherent Tx module is below 4 mm × 1.5 mm, including the SOH chip, the InP light sources and the PWB to the transmission fibre. This corresponds to an on-chip area of only 1.5 mm^2 per coherent transmitter and is comparable to that of monolithically integrated InP-based transmitters [105, 106].

3.4 Summary and outlook

We have shown that *in situ* 3D nanofabrication of photonic wire bonds (PWB) overcomes the limitations of current hybrid photonic integration approaches, namely, the high placement accuracy of elements required during assembly and the necessity to match vastly different mode field sizes. In the first experiment, we used SiP test structures to demonstrate highly efficient and reproducible coupling losses of (0.73 ± 0.15) dB measured from 100 PWB. The PWB were fabricated in a fully automated process and tested under technically relevant environmental conditions without failures or degradation. We further demonstrate the viability of the PWB by realizing two different hybrid multi-chip transmitter engines. A first module is built from eight independent InP lasers connected to arrays of eight SiP modulators and single-mode fibres. The module offers an aggregate line rate of 448 Gbit s^{-1} over distances that are typically found in data-centre and campus-area networks. In a second module, we combine four InP lasers with silicon-based IQ modulators, demonstrating energy-efficient coherent data transmission at an aggregate line rate of 784 Gbit s^{-1} over a distance of 75 km. To the best of our knowledge, this represents the highest data rate thus far demonstrated by a SiP transmitter module with hybrid integrated lasers while maintaining a per-channel footprint comparable

to that of monolithically integrated InP-based systems. While our demonstrations were focused on transmitter modules for high-speed optical telecommunications, the technology may unlock a wide variety of novel applications that benefit from the advantages of hybrid photonic integration.

3.5 Methods

Fabrication: All PWB structures were fabricated using a modified commercial two-photon lithography system (Nanoscribe, Photonic Professional GT) equipped with a 40× microscope objective lens (numerical aperture 1.4, field number 25 mm, write field diameter > 500 μm) as well as galvanometer mirrors for rapid beam movement in the lateral directions. Note that PWB usually fit completely into the accessible write field area. For larger structures, stitch-less lithography based on galvanometric mirrors that are synchronized to sample stage movement could be beneficial [107]. As a lithography light source, we use a fs-laser with a pulse length of 100 fs (FemtoFibre pro NIR, Toptica) and a repetition rate of 80 MHz. The lithography system is equipped with a proprietary control software that allows for precise localization of coupling interfaces as well as for automated PWB fabrication with high shape fidelity. In the lithography process, coarse localization of the chips is typically accomplished by marker detection based on a calibrated bright-field image of the system. Additionally, the system is equipped with a confocal imaging unit using the lithography laser and its beam deflectors for the acquisition of 3D images that are perfectly aligned to the lithography coordinate system and hence to any lithographically fabricated structures. For confocal imaging, the laser power is reduced to avoid any unwanted polymerization.

In our current experiments, we use standard writing techniques without taking any measures for process acceleration, leading to fabrication times of typically 30 s ... 5 min per PWB, depending on the PWB volume. Currently, the exposure time is dominated by the settling time (100 ms) of the piezo-electric actuator that is used for axial movement of the objective between exposure layers, as well as by

the exposure speed. By using the full capacity of current high-speed galvanometer scanners (5000 lines/s for a line length of 40 µm) as well as continuous movement of the piezo-electric actuator, writing times well below 30 s seem reasonable even for large PWB connections.

In the lithography process, the liquid negative-tone photoresist (Nanoscribe IP-Dip, refractive index $n = 1.52$ at 790 nm, see also Ref. [60]) simultaneously acts as an immersion medium for the objective lens. Unexposed photoresist is removed in a two-step development process using propylene-glycol-methyl-ether-acetate (PGMEA) as a developer for 20 min, followed by rinsing in isopropyl alcohol (isopropanol).

Low refractive index cladding: In most cases, a low-refractive index liquid (Cargille Laser Liquid 3421; $n = 1.30$) is drop-cast onto the assembly to emulate a low-refractive-index cladding. For more permanent structures, the low-refractive-index liquid can be replaced with a long-term protective coating. The on-chip PWB connections exposed to climate chamber tests were encapsulated by a low-refractive-index $n = 1.36$ adhesive.

Trajectory planning of the PWB: Each PWB needs to be precisely adapted to the position and the emission direction of the optical coupling interfaces that are to be connected. This requires on-the-fly generation of the corresponding 3D PWB geometry during the fabrication process – another key functionality of our software. In the first step of the PWB design, we calculate a trajectory that is optimized for low curvature and hence low radiation loss. Along this trajectory, the waveguide cross-section is extruded to form a 3D model for subsequent fabrication.

SiP-to-PWB interface: The performance of photonic MCM crucially relies on broadband and efficient coupling between silicon strip waveguides and 3D freeform PWB. For coupling to SiP circuits, we use down-tapered silicon waveguide cores that are embedded into up-tapered PWB waveguides; see Ref. [50] for details. We detected the location of the Si taper by camera-based identification in combination with a local 3D confocal scan.

In our experiments, the SiP chips for the 8-channel IM/DD and the four-channel coherent transmitter originate from the same wafer. To provide direct access to the waveguides for PWB coupling and to enable over-cladding of the SOH slot-waveguide, the top oxide layer covering the photonic devices must be removed. For the transceiver chips, over-etching occurred during the oxide opening due to a non-optimized process. This led to partial damage of the silicon tapers with tip widths of approximately 200 nm rather than the designed 130 nm, and hence caused increased insertion losses of these PWB interfaces. Note that the passive test chip used for our reliability experiment was not subject to such defects; see Figure 3.2 and 3.3. Using defect-free tips, we recently demonstrated [50] PWB connections of HCSEL to passive SiP chips with losses down to 0.4 dB.

Fibre-to-PWB interface: Photonic wire bonds were connected to standard single-mode fibres (Corning SMF-28) with a mode field diameter of $(10.3 \pm 0.4)\,\mu m$, defined as the diameter where the intensity is e^{-2} of its maximum value. Details for fibre-chip interfaces can be found in Ref. [3].

IM/DD transmitter module: For characterization of the IM/DD transmitter, an arbitrary-waveform generator (AWG, Keysight M8196A) is used to provide the bipolar data signals for the two arms of the MZM. The signals are coupled to the chip using a microwave probe in a signal-ground-ground-signal (SGGS) configuration. A 50 Ω resistor terminates the transmission lines. We bias the MZM at the quadrature point for modulating the light intensity either with on-off-keying (OOK) or with four-level pulse amplitude modulated (PAM-4) signals. We apply pre-equalization to compensate for the AWG frequency response. For the transmission experiments based on PAM-4 signalling, we use pulses with cosine shapes in the time domain. The length of the pseudo-random bit sequence (PRBS) amounts to $2^{15} - 1$. As a receiver, we use a *p-i-n*-photodiode with an integrated trans-impedance amplifier (Finisar XPRV2022A-VF-FP). The optical signal is sent either directly to the receiver (back-to-back, B2B), through a 2 km-long SMF (Siecor 1528, attenuation α_{dB} = 0.25 dB km, dispersion coefficient D = 18.5 ps nm^{-1} km^{-1} at 1550 nm), or through a 10 km-long SMF (Corning SMF-28, α_{dB} = 0.18 dB km, D = 18.0 ps nm^{-1} km^{-1}

at 1550 nm). A high-speed oscilloscope (Keysight DSO-X 93204A, 80 GSa/s) is used to record the received signals for offline analysis. The received waveforms were analysed by signal processing routines implemented in Python, which comprise filtering, clock recovery, equalization and resampling.

In the experiment, we measure the launch powers at the respective SMF outputs by adjusting the MZMs to full transmission. For Channel 6 of the IM/DD transmitter, the launch power is reduced by an additional 3 dB multimode interference coupler (MMI) coupler on the silicon chip. To estimate the losses of the PWB connections, we use the total output power P_{las} of the HCSEL prior to photonic wire bonding as a reference and compare it to the power P_{out} at the output connector of the MCM. With P_{las}, P_{out}, and the measured on-chip device loss of the MZM of typically 5 dB, we estimate the compound insertion loss for the pair of cascaded PWB in each channel, leading to an average value of 3.6 dB per PWB in the best case and to 5.3 dB per PWB for the case in which one of the structures was affected by a residual dirt particle. This problem, however, is not fundamental and should disappear if all fabrication steps can be performed under clean-room conditions. For the demonstration of the IM/DD transmitter module, the low-index over-cladding was emulated by an index-matching liquid (Cargille Laser Liquid 3421)

Coherent transmitter module: The losses of the PWB interfaces are estimated by measuring the power levels P_{launch} at the output SMF and by comparing them to the emission power P_{las} of the HCSEL prior to photonic wire bonding, as well as to the power coupled out of additional on-chip taps (not drawn in Figure 3.11) that are connected to grating couplers; see Appendix A.3 for details. For the best PWB connecting the HCSEL to the SiP chip, we estimate a loss of 4.5 dB; the lowest PWB loss on the fibre side amounts to 5.4 dB. These relatively high losses are mainly caused by the fact that the PWB are operated without a protective top cladding or index-matching liquid that would reduce the index contrast and hence allow for single-mode operation of the PWB. Moreover, the efficiency of the coupling

interface to the SiP waveguides is impaired by the non-optimum etching of the top-oxide openings applied to the wafer from which both SiP chips used for the system experiments originate; see the discussion of the SiP-to-PWB interface above. Details on the loss estimation technique can be found in Appendix A.3.

For characterization of the coherent transmitter, we again use an AWG (Keysight M8196A) to generate the drive signals for the optical IQ modulators. The signals are derived from PRBSs with length $2^{11} - 1$ that are pre-equalized to compensate for the measured frequency response of each modulator. At the receiver, the signals are detected by an optical modulation analyser (OMA, Keysight N4391A) acting as a coherent receiver with a built-in external-cavity laser as a local oscillator (LO). The output of the coherent receiver is digitized by a two-channel 80 GSa/s real-time oscilloscope (Keysight DSO-X 93204A) and recorded for offline digital signal processing (DSP), comprising timing recovery, equalization, frequency offset compensation, carrier phase compensation and decoding. The receiver further comprises an erbium-doped fibre amplifier (EDFA) followed by a bandpass filter (full width at half maximum of 0.6 nm) to suppress out-of-band amplified spontaneous emission (ASE) noise.

SOH modulator post-processing: For the SOH electro-optic modulators, the organic cladding material is deposited onto the slot waveguides after photonic wire bonding see Figure 3.10b. To avoid contact of the organic EO cladding with the PWB, we used a high-precision dispensing technique that allows deposition of traces with less than 20 μm width via a thin glass needle. To induce macroscopic EO activity, the material in the SOH MZM is poled in a one-time process, enabling efficient push-pull operation of the devices by a single drive signal; see Ref. [98] for details.

[End of paper [J7].]

4 Ultra-broadband polarization beam splitter and rotator based on 3D-printed waveguides

This chapter reports on a design and experimental realization of a 3D-printed polarization beam splitter / polarization rotator assembly. The chapter was taken from the manuscript [J3] that is being prepared for submission. It was adapted to comply with the layout and structure of this thesis. The Methods and Supplementary Information related to this chapter that are also part of the aforementioned manuscript can be found in Appendix B.

Note that Aleksandar Nesic and the author of this thesis contributed equally to this work. The experiments were conceived by Aleksandar Nesic, Christian Koos and the author. Aleksandar Nesic proposed the polarization beam splitter (PBS) concept, and developed the PBS design. The author developed the design of the polarization rotators, mode-field adapters, connecting waveguides, the fanout, and the structures for mechanical support. He further fabricated all structures using the lithography system described in Section 2.2. The first two authors jointly conducted the experiments based on a infra-red-sensitive microscope and a polarization scrambler and analyser. For these experiments, the present author contributed the evaluation code for the microscope images and proposed algorithms to measure the PER using a polarization scrambler and a polarimeter. Aleksandar Nesic and Pablo Marin-Palomo performed the data transmission experiment with support of Christoph Füllner and Sebastian Randel, who conceived and implemented the signal

processing tools. Pablo Marin-Palomo analysed the results of the data-transmission experiment. The figures were jointly made, and the manuscript was jointly written by the Aleksandar Nesic, the author, Christian Koos and Wolfgang Freude. The work was jointly supervised by Wolfgang Freude and Christian Koos. All authors discussed the data.

[Beginning of Paper [J3].]

Ultra-broadband polarization beam splitter and rotator based on 3D-printed waveguides

ALEKSANDAR NESIC[1,†], MATTHIAS BLAICHER[1,2,†], PABLO MARIN-PALOMO[1], CHRISTOPH FÜLLNER[1], SEBASTIAN RANDEL[1], WOLFGANG FREUDE[1], CHRISTIAN KOOS[1,2]

[1] *Institute of Photonics and Quantum Electronics (IPQ), Karlsruhe Institute of Technology (KIT), 76131 Karlsruhe, Germany.*
[2] *Institute for Microstructure Technology (IMT), KIT, 76344 Eggenstein-Leopoldshafen, Germany.*
[†] *both authors contributed equally to this work*

Multi-photon lithography [33, 108, 109] has emerged as a powerful tool for photonic integration, allowing to complement planar photonic circuits by 3D-printed free-form structures such as waveguides [5, 50] or micro-optical elements [18, 19]. These structures can be fabricated with high precision on the facets of optical devices and lend themselves to highly efficient package-level chip-chip-connections in photonic assemblies [5]. However, plain light transport and efficient coupling is far from exploiting the full geometrical design freedom that is offered by 3D laser lithography. Here, we extend the functionality of 3D-printed optical structures to manipulation of optical polarization states. We demonstrate compact ultra-broadband polarization beam splitters (PBS) that can be combined with polarization rotators (PR) and mode-field adapters into a monolithic 3D-printed structure, fabricated directly on the facets of optical devices. In a proof-of-concept experiment, we demonstrate measured polarization extinction ratios beyond 11 dB over a bandwidth of 350 nm at near-infrared (NIR) telecommunication wavelengths around 1550 nm. We demon-

strate the viability of the device by receiving a 640 Gbit s^{-1} dual-polarization data signal using 16-state quadrature amplitude modulation (16QAM), without any measurable optical-signal-to-noise-ratio (OSNR) penalty compared to a commercial PBS.

4.1 Introduction
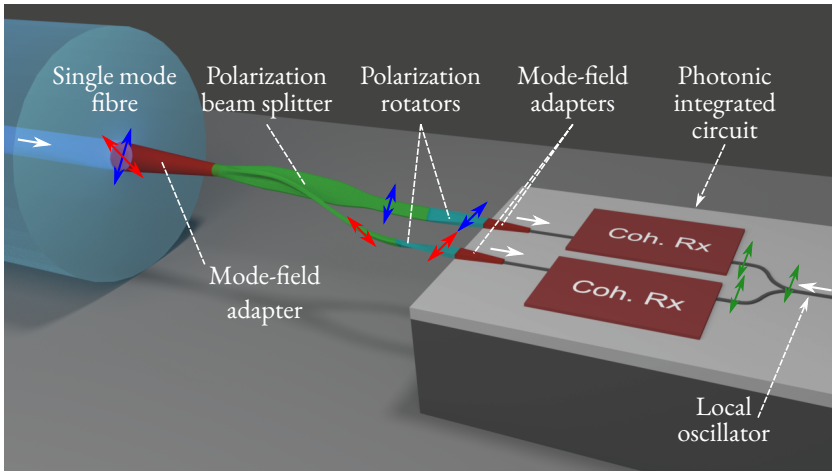
Fig. 4.1: Concept of a 3D-printed polarization beam splitter and rotator in an integrated optical assembly (not drawn to scale). The device connects a rotationally symmetric single-mode fibre (SMF) with degenerate polarization states (red and blue arrows) to a photonic integrated circuit (PIC) with highly polarization-sensitive waveguides. As an example of high practical interest, we illustrate a dual-polarization receiver for coherent communications, in which data signals in orthogonal polarization states are split and independently detected using a pair of coherent optical receivers (Coh. Rx) which are fed by a joint local oscillator (LO). The polarization beam splitter (PBS) and the polarization rotators (PR) can be merged with additional 3D freeform waveguide elements such as mode-field adapters to form a single monolithic structure. This structure can be fabricated in a single exposure step by high-resolution 3D-laser lithography, thereby offering the freedom to adapt the geometry of the 3D-printed structure to the positions of the various optical device facets.

Polarization manipulation is of great importance for integrated optical systems, in particular when it comes to interfacing rotationally symmetric optical fibres with degenerate polarization states to highly polarization-sensitive on-chip waveguides. In conventional optical systems, polarization manipulation usually relies on discrete optical elements such as polarization beam splitters (PBS) or waveplates made from birefringent materials. These devices offer high polarization extinction ratios and low insertion loss over a large spectral range. When used in integrated photonic systems, however, the viability of discrete polarization-manipulating elements is limited, e.g., by the required footprint and by the need for high-precision alignment of these elements with respect to on-chip optical circuits [110]. Alternatively, functionalities manipulating polarization can be integrated into waveguide-based planar photonic circuits, exploiting, e.g., mode-selective directional or multimode interference (MMI) couplers [111–114], polarization mode converters [115, 116], waveguide gratings [117], waveguide structures with multi-layer cores [118, 119], or more complicated structures obtained by inverse design techniques [120]. These devices can be efficiently realized in large quantities, but often require special fabrication steps [118, 119] and are subject to limitations of the device geometry, dictated by conventional layer-by-layer microstructuring through 2D lithography and dry etching. Moreover, polarization manipulation in on-chip structures often relies on efficient coupling of light to the associated waveguides in the first place. In silicon photonics, grating-based polarization beam splitters can be directly integrated into the fibre-chip interface [121]. However, these structures are subject to limited bandwidth and still rely on high-precision active alignment of the single-mode fibre with respect to the on-chip grating coupler. More recently, 3D-printing based on multi-photon lithography has been exploited to realize PBS structures on the facets of single-mode fibres, exploiting polarization-sensitive diffraction gratings [122] and directional couplers within photonic-bandgap waveguides [123]. While these

demonstrations already show the potential of 3D-printing for fabrication of PBS structures, the split signals are simply emitted into free space – without polarization rotation or coupling to further waveguide-based devices. In addition, the underlying physical effects employed in these structures fundamentally limit their bandwidth.

In this paper, we demonstrate that ultra-broadband 3D-printed waveguide-based polarization beam splitters and rotators open an attractive path towards polarization-manipulation in integrated optics. In our structures, polarization splitting is accomplished through adiabatic Y-branches of geometrically birefringent polymer waveguides with high-aspect-ratio cross sections and complemented by polarization rotation in waveguides that are twisted along the propagation direction. The structures can be directly incorporated into freeform chip-chip and fibre-chip connections [5, 124], so-called photonic wire bonds. In our proof-of-concept experiments, we show monolithic structures that are 3D-printed on facets of SMF comprising ultra-broadband polarization beam splitters, polarization rotators, and mode-field adapters. Our prototypes feature more than 11 dB polarization extinction ratios in a wavelength range between 1260 nm and 1660 nm, with vast potential for further improvement. To demonstrate the practical viability of the structures, we use them in a dual-polarization data-transmission experiment, in which we receive a dual-polarization 16-state quadrature amplitude modulation (16QAM) data stream at a symbol rate of 80 GBd and an aggregate data rate of 640 Gbit s^{-1}. We find that our 3D-printed PBS do not introduce any measurable optical-signal-to-noise-ratio (OSNR) penalty when compared to a commercially available fibre-coupled PBS. We believe that 3D-printed optical structures for polarization manipulation can replace costly assemblies of discrete micro-optical elements, thereby paving the path towards optical systems with unprecedented compactness and scalability.

4.1.1 Device concept and design

The basic concept of 3D-printed polarization beam splitters (PBS) and polarization rotators (PR) in integrated optical assemblies is illustrated in Figure 4.1. The device connects a rotationally symmetric single-mode fibre (SMF) with degenerate polarization states to a highly polarization-sensitive photonic integrated circuit (PIC). The illustrated assembly acts as a dual-polarization receiver for coherent communications, in which data signals in orthogonal polarization states of the SMF are split and independently detected using a pair of coherent optical receivers (Coh. Rx), which are fed by a joint local oscillator (LO). The PBS/PR can be merged with additional 3D freeform waveguide elements such as mode-field adapters into a single monolithic structure. This structure can be fabricated in a single exposure step by high-resolution 3D-laser lithography that exploits multi-photon polymerization in the focus of a pulsed femtosecond laser beam [109]. This offers the freedom to adapt the geometry of the 3D-printed structure to the positions of the adjacent optical device facets, thereby overcoming the need for high-precision mechanical alignment of the fibre with respect to the chip [5, 124]. Note that the assembly illustrated in Figure 4.1 represents only one example how 3D-printed polarization-manipulating elements can be used in integrated optics. In general, the structures can be printed on a wide range of optical devices, covering applications from optical communications and signal processing [125, 126] to optical metrology [81] , imaging [127], and quantum optics [128].

The working principle of our 3D freeform waveguide-based PBS is illustrated in Figure 4.2. Figure 4.2 depicts a 3D rendering of the three-port device, comprising an input waveguide port with a circular cross section and a pair of output waveguide ports with rectangular cross sections of high aspect ratio. In the following, the input port is denoted by a superscript (I), whereas superscripts (H) and (V) refer to the

output ports with horizontally and vertically oriented rectangular cross section, see Figure 4.2. Note that the device is fully bidirectional and can also be used as a polarization beam combiner, where the two rectangular waveguide ports H and V are used as inputs, whereas the circular port I acts as output.

The PBS consists of three segments, denoted by A, B, and C, where Segment A is directly adjacent to the input port. Due to its circular cross section, the input port has two degenerate fundamental modes of orthogonal polarizations with identical effective refractive indices n_{eff}. Without loss of generality, we select the two basis modes at the input with the dominant transverse component of the electric field aligned in the vertical and horizontal direction as defined by the two output ports, and we denote them as $E_H^{(I)}$ and $E_V^{(I)}$ respectively, see first row of Figure 4.3 for the associated mode-field distributions. Within Segment A, the circular cross section at the input port is adiabatically morphed into a cross-shaped cross section at the transition to Segment B. At the transition between Segment A and Segment B the waveguide can be represented by two spatially overlapping partial waveguides $\mathrm{WG_H}$ and $\mathrm{WG_V}$ with high-aspect-ratio rectangular cross-sections. Due to the adiabatic transition from a circular cross section to a cross-shaped one in Segment A, the two degenerate basis modes denoted as $E_H^{(I)}$ and $E_V^{(I)}$ are transformed to the strongly guided modes of these rectangular partial waveguides. In this context, the term 'strongly guided' denotes a mode of a rectangular waveguide which is polarized along the long side of the rectangle. This mode exhibits a higher effective refractive index than its weakly guided counterpart that is polarized along the short side of the rectangular waveguide core. In Segment B, the partial waveguides $\mathrm{WG_H}$ and $\mathrm{WG_V}$ are gradually separated, thereby dragging the corresponding strongly guided eigenmodes into the two distinct waveguides at the input of Segment C.

Within Segment C, the two distinct output waveguides can be adiabatically tapered and bent to suppress unwanted higher-order modes and to route the waveguides to the two output ports V and H. Further 3D-printed freeform waveguide structures can be directly connected to these output ports, e.g., for polarization rotation, see Figure 4.1. The second and the third row of Figure 4.3 show the various mode-field

profiles at the output, where $E_H^{(V)}$ refers to the horizontally and $E_V^{(V)}$ to the vertically polarized mode at the vertical output V, whereas $E_V^{(H)}$ denotes the vertically and $E_H^{(H)}$ the horizontally polarized mode at horizontal output H. In an ideal device, the power of the degenerate $E_H^{(I)}$ and $E_V^{(I)}$ is completely coupled to the strongly guided modes $E_H^{(H)}$ and $E_V^{(V)}$, whereas the weakly guided modes $E_H^{(V)}$ and $E_V^{(H)}$ are not excited.

To estimate the performance of the proposed PBS, we perform numerical simulations of the full 3D structure, see Methods for details. For good performance, the aspect ratio of the rectangular waveguide cross sections should be as high as possible while staying compatible with the resolution of the 3D printing system. In the simulated structure, the short side of the rectangle was chosen to $w_{sh} = 400$ nm, whereas the long side w_{lo} varied in the range between 1.2 μm and 2.2 μm. The length of the structure including all three segments amounts to $L = 21$ μm. The PBS features full geometrical symmetry, see inset of Figure 4.2, which results in symmetrical relationships between the port modes. In Figure 4.2, we illustrate the magnitude of the E-field at a wavelength of 1550 nm for horizontal polarization at the input – the E-field distribution for vertical input polarization is obtained by reflection about the symmetry plane. To describe the coupling between the various modes at the input and the output ports, we use complex-valued scattering parameters (S-parameters) S_{IJ}. In this description, S_{IJ} refers to the amplitude transmission from J to I where $I, J \in \left\{ E_H^{(I)}, E_V^{(I)}, E_H^{(H)}, E_V^{(H)}, E_H^{(V)}, E_V^{(V)} \right\}$ denote the various modes at the ports of the device. The results for the various simulated power coupling coefficients, which are obtained by squaring the magnitudes of the corresponding S-parameters are shown in Figure 4.4. Evaluating the power transmission $\left| S_{E_H^{(H)} E_H^{(I)}} \right|^2 = \left| S_{E_V^{(V)} E_V^{(I)}} \right|^2$ from the input to the desired mode of the respective output port, we find an insertion loss of less than 2 dB over the entire wavelength range between 1250 nm and 1650 nm, with a minimum of 1.6 dB near 1550 nm, see green line in Figure 4.4. For each polarization at the input port, we further extract the power that is coupled to the undesired mode at the corresponding ("correct") output port,

which is quantified by the crosstalk $\left|S_{E_V^{(H)} E_H^{(I)}}\right|^2 = \left|S_{E_H^{(V)} E_V^{(I)}}\right|^2$, and which is below $-22\,\text{dB}$ throughout the simulated wavelength range, see blue line in Figure 4.4. Note that this crosstalk can be suppressed by subsequent polarization filtering. We further calculate the power that is coupled to the desired output modes $E_H^{(H)}$ and $E_V^{(V)}$, from the 'wrong' input modes $E_V^{(I)}$ and $E_H^{(I)}$, respectively, and that cannot be suppressed by subsequent polarization filters. This unfilterable crosstalk $\left|S_{E_H^{(H)} E_V^{(I)}}\right|^2 = \left|S_{E_V^{(V)} E_H^{(I)}}\right|^2$ is represented by the red line in Figure 4.4 and is below $-25\,\text{dB}$ throughout the 400 nm-wide wavelength range of interest. We also extract the polarization leakage $\left|S_{E_H^{(V)} E_H^{(I)}}\right|^2 = \left|S_{E_V^{(H)} E_V^{(I)}}\right|^2$, which, for a given polarization at the input port quantifies the power coupled to undesired polarization at the "wrong" output port, thereby maintaining its polarization direction. For our structure, the polarization leakage is below $-17\,\text{dB}$ throughout the simulated wavelength range, see orange line in Figure 4.4, and can be further suppressed by subsequent polarization filters. Finally, we extract the polarization extinction ratio (PER), i.e., the ratio of the maximum and the minimum power observed in both modes of an output port when varying the excitation at the input over all possible polarization states. For each of the output ports, the PER can be obtained from a singular-value decomposition of the corresponding Jones matrix, see Appendix B.1 for details. We find that the PER is better than 16 dB within the investigated wavelength range and shows a strong increase towards longer wavelengths. Note that the PER and polarization leakage are better than 30 dB over the wavelength range between 1250 nm and 1365 nm, and that this wavelength range of high performance can be shifted by adapting the design of the structure.
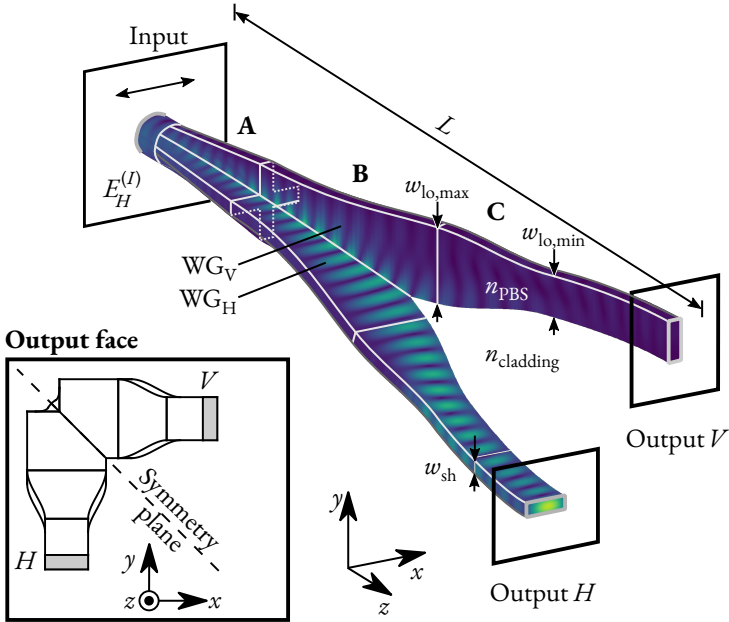
Fig. 4.2: Concept and design of 3D-printed waveguide-based PBS. 3D model of the PBS, comprising an input waveguide port with a circular cross-section and a pair of output waveguide ports with rectangular cross sections of high aspect ratio. The two orthogonally polarized modes at the input port are denoted as $E_H^{(I)}$ and $E_V^{(I)}$, whereas $E_H^{(V)}$ refers to the horizontally and $E_V^{(V)}$ to the vertically polarized mode at the vertical output V, while $E_V^{(H)}$ denotes the vertically and $E_H^{(H)}$ the horizontally polarized mode at the horizontal output H. The PBS consists of three segments denoted by A, B, and C. Within Segment A, the circular cross section at the input port is adiabatically morphed into a cross-shaped cross section. Within Segment B, the structure can be represented by two spatially overlapping partial waveguides WG_H and WG_V with high-aspect-ratio rectangular cross-sections, which are gradually separated to drag the strongly guided eigenmodes into the two distinct waveguides at the input of Segment C. The 3D rendering of the structure also depicts the simulated electric field distribution for a horizontally polarized excitation $E_H^{(I)}$ at the input port. The PBS exhibits full geometrical symmetry, with respect to a plane that is oriented at 45° between the horizontal and the vertical direction, see Inset. The refractive index of the 3D-printed PBS core region amounts to $n_{PBS} = 1.53$, and the cladding material is air, $n_{cladding} = 1.0$.
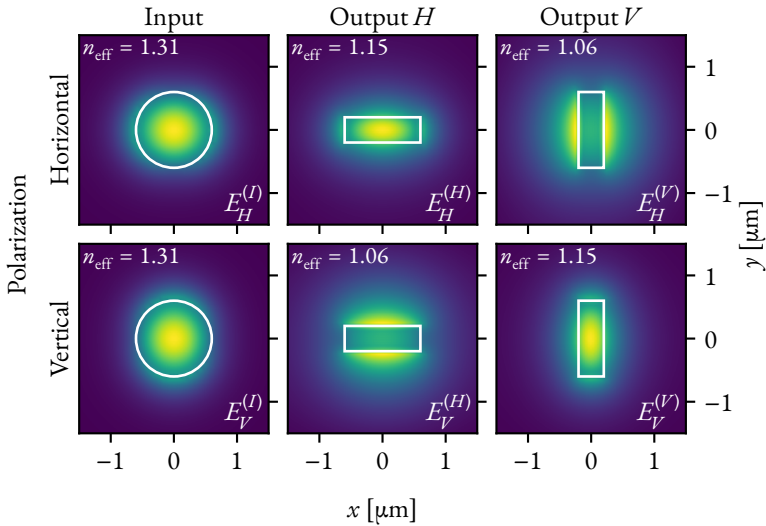
Fig. 4.3: Electric field plots (|E|) of the fundamental modes for both polarizations at all three ports of the PBS. The strongly guided target modes $E_H^{(H)}$ and $E_V^{(V)}$ at the horizontal and vertical output exhibit a higher effective index and a stronger confinement to the rectangular core than the undesired modes $E_V^{(H)}$ and $E_H^{(V)}$
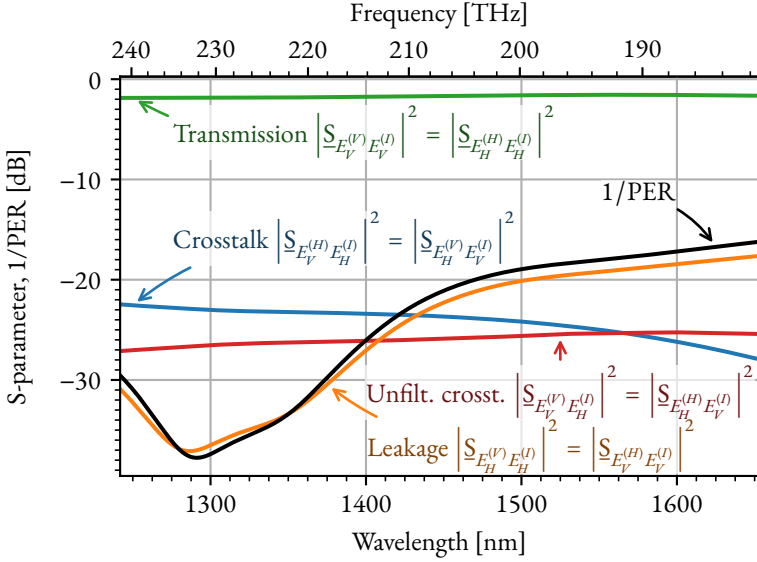
Fig. 4.4: Simulated wavelength dependence of the squared magnitudes of complex scattering parameters (S-parameters) and the reciprocal of the polarization extinction ratio (1/PER) of the PBS on a logarithmic scale. The transmission is better than -2.0 dB with a maximum of approximately -1.6 dB near $\lambda_0 = 1550$ nm. The reciprocal of the polarization extinction ratio (1/PER), and spurious coupling $\left|S_{E_V^{(H)} E_H^{(I)}}\right|^2 = \left|S_{E_H^{(V)} E_V^{(I)}}\right|^2$, $\left|S_{E_H^{(H)} E_V^{(I)}}\right|^2 = \left|S_{E_V^{(V)} E_H^{(I)}}\right|^2$, and $\left|S_{E_H^{(V)} E_H^{(I)}}\right|^2 = \left|S_{E_V^{(H)} E_V^{(I)}}\right|^2$ between input and output modes are below -16 dB over the 400 nm wide wavelength range. These parameters can be further reduced for smaller wavelength ranges. Details on extracting the PER from the simulations can be found in Appendix B.1.

89

4.2 Experimental verification

To experimentally prove the viability of our concept, we fabricate a series of 3D-printed PBS that are directly connected to the cores of single-mode fibres (SMF). We characterize the performance of these devices and finally use them as part of a receiver in polarization-division multiplexing (PDM) data transmission experiment.
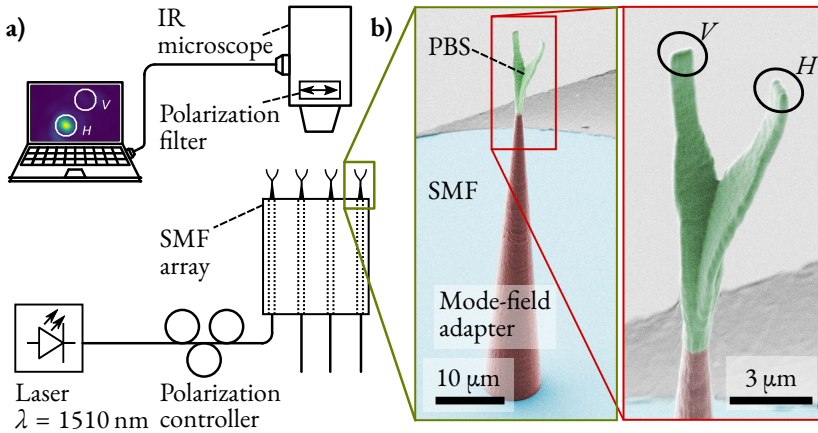
Fig. 4.5: Characterization of 3D-printed PBS using an infra-red-sensitive (IR) microscope. a) Experimental setup: As test structures, we use a series of PBS that are 3D-printed on the facets of a single-mode fibre (SMF) array. Light at a wavelength of 1510 nm is fed to the devices by a laser and a subsequent polarization controller. Light emitted from the PBS is characterized by an IR microscope equipped with polarization filter, (PF). **b)** Scanning-electron microscopy (SEM) images of a fabricated structure on the fibre array. A linear taper structure, shaded in red, is used at the input of the PBS to adapt the mode-field diameter of the SMF to the one of the PBS input. Within the PBS, which is illustrated in green, the light is split into two orthogonal polarizations and emitted from the outputs (V and H) towards the IR microscope. Colors were added by image processing.

4.2.1 Characterization of basic performance parameters

In a first experiment, we fabricate a series of free-standing PBS on the facets of an SMF array and measure the performance through an infra-red-sensitive microscope (IR microscope), see Figure 4.5a. To ensure low-loss coupling to the SMF core, the structures are equipped with adiabatic mode-field adapters that are attached to Segment A of the PBS. A scanning-electron microscope (SEM) image of the PBS and the mode-field adapter are shown in Figure 4.5b. Light is fed to the SMF by a laser emitting at a wavelength of λ_0 = 1510 nm, and subsequent polarization controller. At the two PBS outputs, the light is radiated into free space and picked up by the IR microscope. The centres of the white circles in the images of Figure 4.6 match the centres of corresponding PBS output ports, and the areas of the circles denote the areas that have been considered in calculating the corresponding power levels. In a first set of measurements we show that radiated light can be switched between the two output ports of the PBS by varying the polarization at the input, see Column 1 of Figure 4.6. Specifically, Subfigures 1.1 and 2.1 refer to the cases where the polarization controller was adjusted for maximum radiation from output port V and H, having vertically and horizontally oriented waveguide cross sections, respectively. In both cases, we measure the ratio Γ of the optical power at the targeted output port to the residual power emitted at the respective other port, which amounts to 9.8 dB and 9.7 dB, respectively. We also adjust the input polarization to yield equal power at both ports, see Subfigure 3.1 in Figure 4.6. To check the polarization states of the light radiated from the two outputs, we repeat the experiment with a vertically and horizontally oriented polarization filter (PF) between the microscope objective and the IR camera, see Columns 2 and 3 of Figure 4.6. The PF has an extinction ratio of more than 34 dB. Assuming an excitation with pure vertical polarization in Row 1 of Figure 4.6, the vertically oriented PF in Subfigure 1.2 suppresses the spurious horizontal polarization at Port V, which corresponds to the crosstalk $S_{E_H^{(V)} E_V^{(I)}}$, as well the spurious horizontal polarization at Port H, which represents the unfilterable crosstalk $S_{E_H^{(H)} E_V^{(I)}}$. The measured power ratio Γ of the emitted light after the

PF amounts to 12.1 dB and corresponds to the ratio $\left|S_{E_V^{(V)}E_V^{(I)}}\right|^2 / \left|S_{E_V^{(H)}E_V^{(I)}}\right|^2$ of the power transmission at Port V and the leakage at Port H. The measured ratio is smaller than the approximately 18 dB that would be expected from the simulation results, see Figure 4.4. We attribute the deviations to geometrical inaccuracies of the fabricated structure. In Subfigure 2.2, the polarization controller is adjusted for maximum radiation from output H, but the PF is oriented vertically, such that only spurious horizontal polarizations at both outputs, $\left|S_{E_H^{(H)}E_V^{(I)}}\right|^2$ and $\left|S_{E_H^{(V)}E_V^{(I)}}\right|^2$ can be seen on the IR camera. As expected, the camera image does not show any significant power. In Subfigure 3.2, where light exits both output arms of the PBS, the light radiated from Port H is completely suppressed by the vertically oriented PF, whereas the light radiated from Port V does not experience a significant attenuation. The same experiment is repeated with a horizontally oriented PF, see Column 3 of Figure 4.6, thereby essentially reproducing the findings described for the data in the second column. This simple experiment demonstrates that the device qualitatively works as expected.

4.2.2 Measurement of polarization extinction ratio (PER)

In a second experiment, we further test our PBS structures by measuring the PER over a broad range of wavelengths. To this end, the polarization at the input of the structure is varied randomly by a polarization scrambler, while the Stokes vector and the power at the device output are continuously recorded by a polarimeter, see Appendices B.1, B.2, B.3 for details. The measurement is repeated for each of the output ports, thereby revealing the output polarization state of maximum and minimum power transmission as well as the associated PER. The PBS test structure used in this experiment is again 3D-printed on the facet of an SMF array, which is connected to the polarization scrambler. At the output, the structure is equipped with a pair of polarization rotators (PR), realized by rectangular waveguides that are twisted by 45° along the propagation direction [46, 118], thus providing identical polarizations at both ports, see Figure 4.1 and Figure 4.7. For better probing of

the output, the structure is equipped with adiabatic mode-field adapters that are held by a table-like mechanical support structure, see Figure 4.7. The output ports can hence be individually read out by an SMF, see Supplementary Information Section S1 for details of the experiment. We find a measured PER better than 11 dB in the wavelength range of 1260 nm to 1620 nm, which was only limited by the tuning range of the underlying laser sources, see Figure 4.8a. The measured insertion losses at 1550 nm for Output I and Output II correspond to 4.4 dB and 3.8 dB, respectively, including the loss of the PBS, of the subsequent PR, and of the adiabatic mode-field adapters at the input and the output of the device, see Appendix B.1 for details.

4.2.3 Data transmission experiment

To demonstrate the technical viability of 3D-printed PBS, we finally perform a polarization division multiplexing (PDM) data-transmission experiment that emulates the application scenario illustrated in Figure 4.1. The experimental setup and the results are shown in Figures 4.7 and Figures 4.8. Details of the experimental setup can be found in the Supplementary Information Section S4. The experiment relies on a PBS/PR combination as used in the previous experiment, complemented by an additional fan-out structure, see Figure 4.7. This fan-out structure is 3D-printed on a second fibre array and allows to simultaneously couple both PBS outputs to a pair of outgoing SMF with a standard pitch of 127 μm, see Figure 4.7. The fan-out structure is equipped with two lenses with a pitch of 25 μm that pick-up light from the two PBS outputs, followed by a pair of total-internal-reflection (TIR) mirrors in each path to adjust the lateral offset of the beams at the output. At λ_0 = 1550 nm, the measured insertion losses of the two channels of the fan-out are 1.2 dB and 1.9 dB, with a crosstalk between channels below −46 dB.

In the transmission experiment, we launch a 16QAM PDM signal at a symbol rate of 80 GBd and a center wavelength of λ_0 = 1550 nm to the PBS, and we feed the two output signals of the PBS/PR assembly to a pair of coherent receivers, see Appendix B.3 for details. We perform the experiment both with our 3D-printed PBS assembly and with a commercially available fibre-coupled PBS having a PER in excess of 30 dB. In both cases, we sweep the optical signal-to-noise ratio (OSNR) at the input of the PBS and record the constellation diagrams along with the bit error ratios (BER), see Figure 4.8. At a BER of 1.25×10^{-2}, our transmission setup exhibits an OSNR penalty of approximately 3 dB, see Figure 4.8c, which is in accordance with values in literature for similar modulation formats and symbol rates [129]. We find that the 3D-printed PBS/PR assembly does not introduce any additional OSNR penalty with respect to the commercial PBS, although the PER differ vastly. This may be attributed to the fact that the polarization-sensitive mixing of the data signals with the local oscillator of the coherent optical receiver in combination with the digital polarization demultiplexing algorithms of the PDM receiver can easily compensate for the finite PER of our 3D-printed PBS. Hence, even though there is still room for improving the performance of our 3D-printed PBS/PR assemblies, the current devices already offer an attractive route towards highly scalable ultra-compact dual-polarization receivers as shown in Figure 4.1.

Orientation of polarization filter
in imaging path
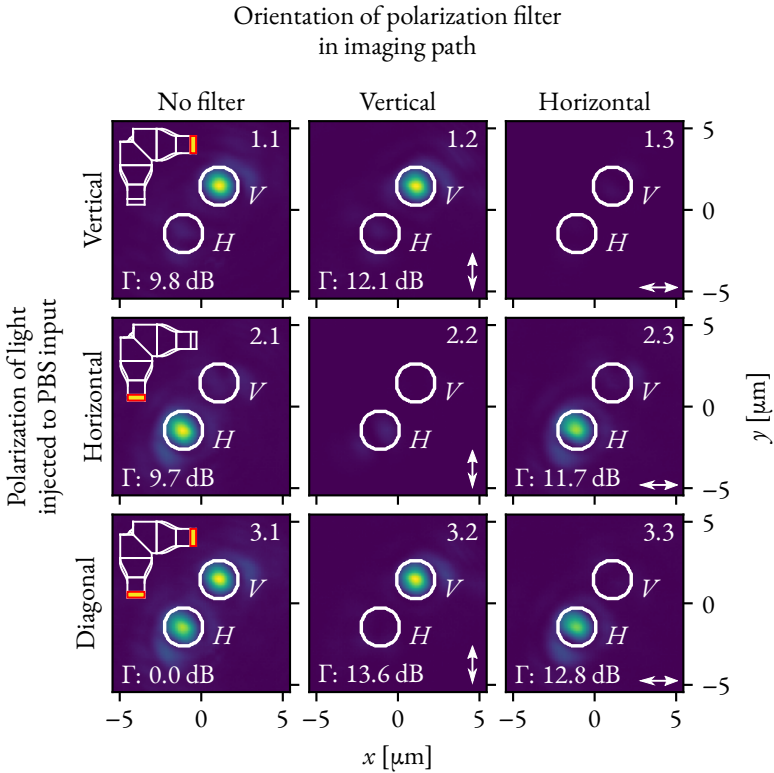
Fig. 4.6: Characterization of 3D-printed PBS using an infra-red-sensitive (IR) microscope. Recordings on the IR microscope for different combinations of input polarization states, indicated by the different rows: Row 1 – vertical input polarization only, Row 2 – horizontal input polarization only, and Row 3 – both vertical and horizontal input polarizations. The columns correspond to the measurement of the radiated power without (Column 1) and with vertically and horizontally oriented polarization filter (Columns 2 and 3, respectively) in the imaging path of the IR microscope. The output power of each port is estimated by integrating the measured intensity over the areas within the white circles, and a power ratio Γ in dB is calculated by dividing the larger by the smaller power. A top view of the PBS structure and the respective "active" output port for each row is additionally illustrated in Column 1. The orientation of the polarization axis of the PF is illustrated by the double arrows in the lower right-hand corner of the displays in Columns 2 and 3.

95
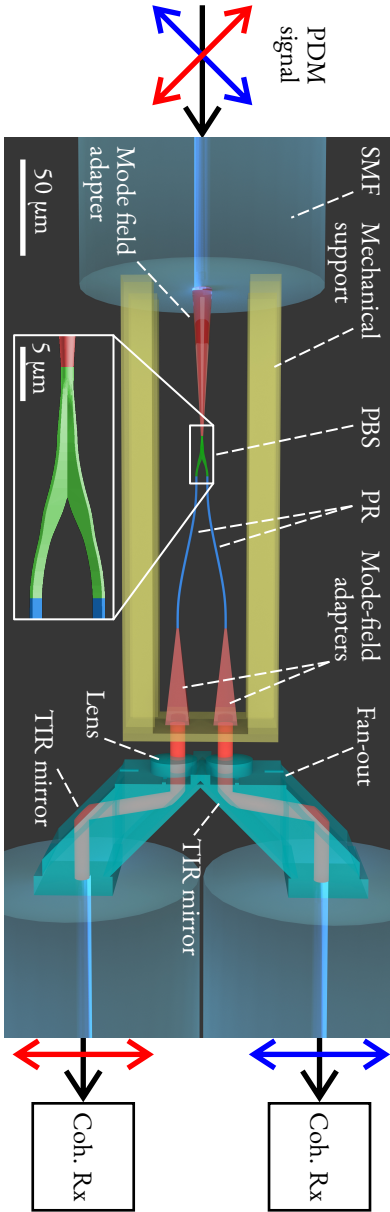
Fig. 4.7: Simplified experimental of proof-of-concept data transmission experiment setup. Simplified experimental setup: The polarization-division-multiplexed (PDM) 16QAM signal is fed to an SMF having a mode-field adapter and a 3D-printed polarization beam splitter (PBS) on its facet. The PBS is additionally equipped with 3D-printed polarization rotators (PR) in the form of twisted waveguides, which rotate the polarizations in both output ports to an identical direction. We simultaneously probe the two output signals by a fan-out structure that is 3D-printed on a second SMF array. The fan-out consists of two lenses and two pairs of total-internal-reflection (TIR) mirrors to adapt the 25 μm pitch of the PBS/PR outputs to the 127 μm pitch of the SMD in the array. The signals are subsequently decoded by a pair of commercial coherent receivers (Coh. Rx). To benchmark our device, we repeat the experiment by replacing the PBS/PR assembly and the fan-out by a commercial fibre-coupled PBS.
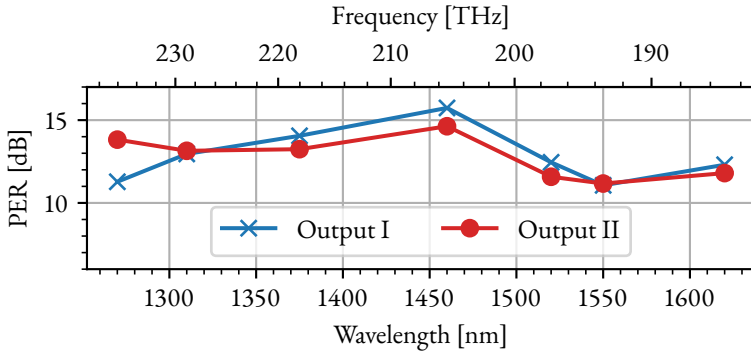
(a) Measurement of the PER for both outputs showing very broadband operation over 360 nm with PER in excess of 11 dB.
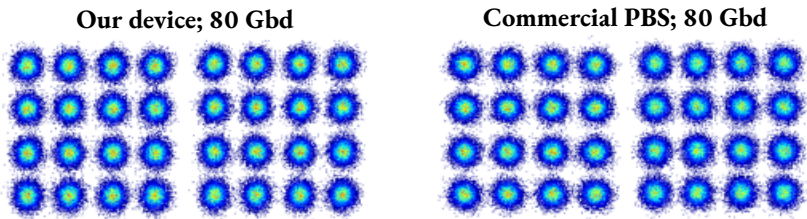
(b) Constellation diagrams of received 80 GBd 16QAM signals. First double column: experiment with our device. Second double column: experiment with the commercial PBS.
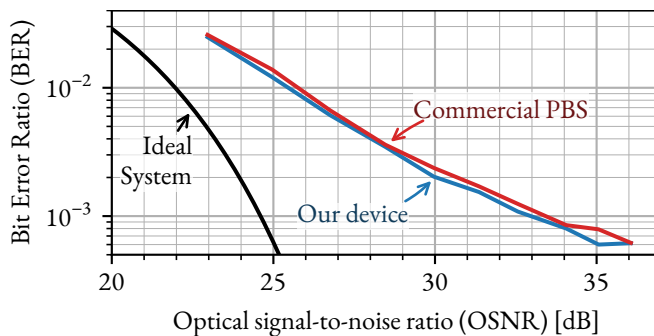
(c) Bit-error-ratio (BER) vs. optical signal-to-noise ratio (OSNR). **Black:** Theoretical curve for an ideal transmission system. **Blue:** Experiment with our 3D-printed PBS/PR assembly. **Red:** Experiment with the commercial PBS. Our device does not introduce an OSNR penalty with respect to the commercial PBS.

Fig. 4.8: Results of proof-of-concept data transmission experiment.

4.3 Summary

We demonstrated 3D-printed waveguide-based polarization beam splitters (PBS) that can be efficiently integrated into chip-chip and fibre-chip interfaces of optical assemblies. The devices rely on adiabatic Y-branches of geometrically birefringent waveguides with high-aspect-ratio cross sections and can be complemented by polarization rotators (PR) that exploit twisted 3D freeform waveguides. The PBS/PR can be efficiently fabricated by direct-write two-photon lithography together with other 3D-printed elements such as photonic wire bonds [5, 124], micro-lenses [18], or waveguide overpasses [51]. In our proof-of-concept experiments, we demonstrate broadband operation in the wavelength range of 1260 nm to 1660 nm, limited only by the available equipment. We further prove the practical viability of the concept in a high-speed data transmission experiment, where our 3D-printed PBS/PR assemblies are used for separating polarization-multiplexed data signals at the receiver. We find that the quality of the received signals is on par with that obtained by a conventional high-performance fibre-coupled PBS. While the concept leaves room for further optimization, we believe that 3D-printed PBS/PR can pave the path towards efficient polarization manipulation in integrated optical systems with unprecedented compactness and scalability.

4.4 Methods

Simulations: For the simulations shown in Figures 4.2, 4.3 and 4.4, the 3D structure of the PBS was modeled using a commercially available 3D numerical time-domain solver (CST Studio Suite, Dassault Systèmes, Vélizy-Villacoublay, France). The final design of the PBS was the result of a manual optimization based on several parameter sweeps.

Fabrication: All 3D-printed structures were fabricated using a home-built two-photon lithography system equipped with a 63× microscope objective lens (numerical aperture 1.4, field number 25 mm) and galvanometer mirrors for rapid beam movement in the lateral directions. As a lithography light source, we use a fs-laser with a pulse length of less than 80 fs (C-fiber 780 femtosecond fibre laser, Menlo, Systems GmbH, Planegg, Germany) and a repetition rate of 100 MHz. The lithography system is equipped with a dedicated control software that allows for precise localization of the optical fibre core as well as for automated fabrication of the PBS with high shape fidelity. The system is equipped with a confocal imaging unit using the lithography laser and its beam deflectors for the acquisition of 3D images that are perfectly aligned to the lithography coordinate system and hence to any lithographically fabricated structures. For confocal imaging, the laser power is reduced to avoid any unwanted polymerization in the photoresist. In the lithography process, the liquid negative-tone photoresist (Nanoscribe IP-Dip, refractive index $n = 1.52$ at 780 nm, unexposed; see also Ref. [60]) simultaneously acts as an immersion medium for the objective lens. Unexposed photoresist is removed in a two-step development process using propylene-glycol-methyl-ether-acetate (PGMEA) as a developer for 20 min, followed by rinsing in isopropyl alcohol (2-propanol).

Trajectory planning and fibre-to-PBS interface: For the polarization rotators and the output waveguides, careful planning of the 3D trajectory is important to ensure efficient coupling between the PBS and other optical structures. To this end, we use a parametrized trajectory and optimize it for low curvature and hence low radiation loss. Along this trajectory, the waveguide cross section is extruded to form a 3D model of the structure that is then lithographically fabricated. Low-loss coupling between PBS and the standard single-mode fibre (Corning SMF-28) at its input is achieved by a linearly tapered mode-field adapter, designed for a mode-field diameter (MFD) of $(10.3 \pm 0.4)\,\mu\text{m}$ at 1550 nm at the fibre side. The MFD is defined as the diameter at which the intensity has dropped to $1/e^2$ of its maximum value measured in the centre of the fibre core. The methods are derived from the photonic wire bonding process, details on which can be found in Ref. [5].

Characterization using an IR microscope: For characterization of the 3D-printed PBS in 4.5, we use an IR camera (Goldeye G-032 SWIR, Allied Vision) attached to a microscope (DMRXA with a variable zoom unit DMRD, Leica/Leitz) that is equipped with an IR objective (LMPlan IR 100×/0.80NA, Olympus). An optional rotatable linear polarizer (LPIREA100-C, Thorlabs, BER > 43 dB at 1550 nm) can be inserted into the infinity-optical beam path of the microscope. Laser light generated by a tunable external-cavity laser (IQS-2600B, EXFO) is injected into the SMF, and the polarization is adjusted by a standard fibre-based polarization controller. Each acquired image is corrected for the background signal that is seen with the laser turned off.

Polarization extinction ratio measurement: The Stokes vector response shown in Figure B.2 is measured by an optical component analyser (Keysight N7788B), which comprises an integrated fast polarization controller and a polarimeter. The polarization controller randomly scrambles the state of polarization, thereby uniformly covering the whole Poincaré sphere. The polarization state and the power at the output of the PBS structure are measured simultaneously by the polarimeter. The PER can be extracted from these measurements, see Appendix B.2 for details. The PER is measured at seven discrete wavelengths between 1270 nm and 1620 nm, using three different tunable laser sources (Ando AQ321D, TUNICS-T1005HP, Agilent 81600B).

Data transmission experiment: In our data transmission experiments, we used four output channels from an AWG (Keysight M8196A) to generate the drive signals for the dual-polarization IQ modulator, see Appendix B.3 for a sketch of the underlying experimental setup. The signals are derived from random bit patterns with different seeds, such that each polarization carries uncorrelated data, and are pre-distorted to compensate for the measured frequency response of the transmitter. For the optical signal-to-noise ratio (OSNR) sweep, band-limited amplified spontaneous-emission (ASE) noise is generated by an ASE source (Orion Laser Technology ASE-C/CL) and added to the data signal. The noise-loaded signal is then fed to the receiver, which comprises an erbium-doped fibre amplifier (EDFA)

for pre-amplification, followed by a bandpass filter (full width at half maximum 1 nm) to suppress out-of-band amplified spontaneous emission (ASE) noise. The signal is then fed to the 3D-printed PBS/PR shown in Figure 4.7, where the two orthogonal polarization states are split and rotated. The two partial signals are then detected using a coherent heterodyne scheme, where the optical local oscillator tone (LO, Keysight N7714A) tuned to the edge of the signal spectrum and where two balanced photodiodes (Finisar BPDV2150RQ) remove both signal-signal and LO-LO interference, see Supplementary Information Section S3 for details. The outputs of the photodiodes are digitized by a 256 GSa/s real-time oscilloscope (Keysight UXR1004A) and recorded for offline digital signal processing (DSP). In a first DSP step, the signals are shifted in frequency by the difference between the carrier and the LO tone. After timing recovery, a 2 × 2 MIMO equalizer is used for polarization de-multiplexing, followed by carrier recovery. Finally, the signals go through a least-mean-square equalizer before being finally decoded.

[End of paper [J3].]

5 3D-Printed Ultra-Broadband Highly Efficient Out-of-Plane Coupler for Photonic Integrated Circuits

This chapter explores the usage of PWB based devices beyond the original chip-to-chip concept. While PWB are traditionally attached to devices on both ends, this chapter explores PWB which are only attached to a photonic chip at one end, while the other end features a micro-lens printed in the same lithography step. This approach enables ultra-broadband coupling to optical fibres which can be positioned, after the structure was fabricated. In many applications, such a structure can replace and significantly outperform traditional planar grating couplers in efficiency and bandwidth. This chapter was first presented at the *CLEO 2018* conference. The material from the publication was adapted to comply with the layout and structure of this thesis.

The concept of a micro-lens attached to a PWB were initially proposed by the author of this dissertation in his master's thesis for the use with silicon nitride strip waveguides [130]. These experiments were finalized by Helge Gehring and resulted in the joint journal contribution [J13]. These earlier results employed a PWB without any cladding material which resulted in unpredictable excitation of higher-order modes. In addition, the lens surface was found experimentally and not optimized analytically. In the framework of this dissertation, the focus shifted to silicon wave-

guides, and simulation driven design of the micro-lens. In addition, the micro-lens and the PWB were embedded in a cladding matterialenabling reliable operation of the device. The interface to silicon inverse taper couplers was developed with the help of Muhammad Rodlin Billah and Tobias Hoose. Andreas Hofmann and the author developed a cladding process related to this structure. A patent application is currently pending and prevents inclusion of further details in this chapter. Philipp-Immanuel Dietrich designed the lens for the first prototype structure using a commercial lens design software, before the custom-made simulation tools, see Section 2.4, were available. The author wrote the manuscript of the paper with support by Christian Koos and Wolfgang Freude.

[Beginning of Conference Contribution [C16].]

3D-Printed Ultra-Broadband Highly Efficient Out-of-Plane Coupler for Photonic Integrated Circuits

Matthias Blaicher[1,2], **Muhammad Rodlin Billah**[1,2], **Tobias Hoose**[1,2], **Andreas Hofmann**[3], **Philipp-Immanuel Dietrich**[1,2,4], **Sebastian Randel**[1], **Wolfgang Freude**[1], **Christian Koos**[1,2,4]

[1] *Institute of Photonics and Quantum Electronics (IPQ), Karlsruhe Institute of Technology (KIT), 76131 Karlsruhe, Germany.*

[2] *Institute for Microstructure Technology (IMT), KIT, 76344 Eggenstein-Leopoldshafen, Germany.*

[3] *Institute for Automation and Applied Informatics (IAI), KIT, 76344 Eggenstein-Leopoldshafen, Germany.*

[4] *Vanguard Automation GmbH, 76185 Karlsruhe, Germany.*

[5] *Fraunhofer Institute for Telecommunications, Heinrich Hertz Institute (HHI), 10587 Berlin, Germany.*

[5] *Institute of Integrated Photonics (IPH), RWTH Aachen, 52074 Aachen, Germany.*

[†] *both authors contributed equally to this work*

5.1 Introduction

Coupling fibre-guided light from or to on-chip waveguides is a key challenge of photonic integration. Out-of-plane coupling via the chip surface represents a particularly attractive approach, offering relaxed alignment tolerances along with scalability to large port counts while greatly simplifying routing of on-chip waveguides. For large-scale silicon-based photonic integrated circuits (PIC), out-of-plane coupling

Schematic side view

SMF

Microlens

Support

Waveguide section

SiP

20 μm
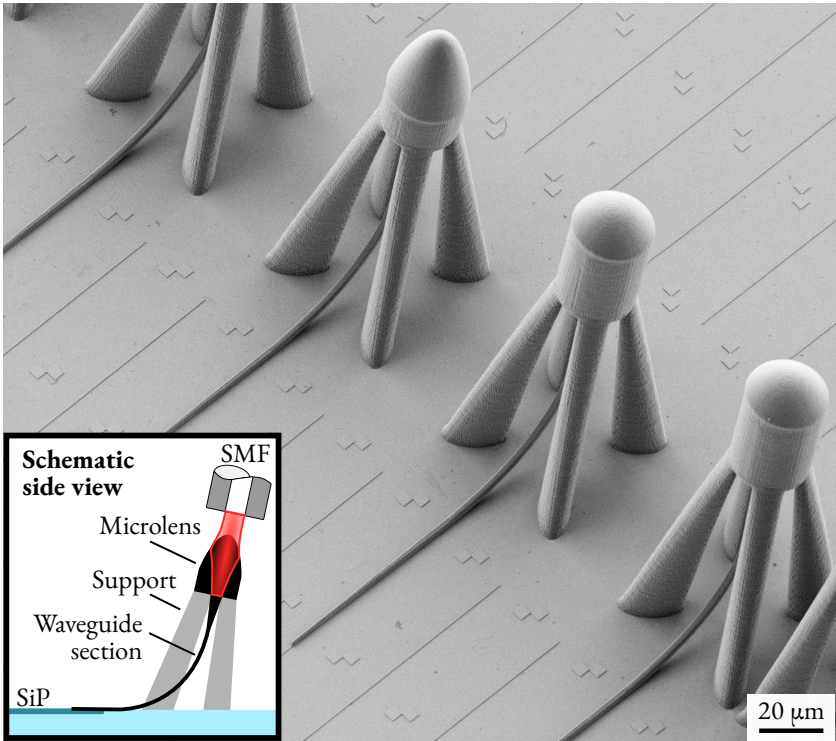
Fig. 5.1: Scanning electron micrograph of 3D micro-printed photonic wire bonds with attached microlenses (lensed PWB, LPWB) for out-of-plane coupling. These LPWB comprise a dielectric polymer waveguide connected to a silicon nanowire on one side, and a microlens on the other side. The full structure is fabricated in a single lithographic step within nine minutes. The coupler axis is tilted by 12° with respect to the chip normal in order to facilitate an easy comparison with GC which are also available on the chip. The concept can be readily adapted to vertically oriented coupler axes. The micro-lens surface can be optimized for coupling to a large range of target mode fields. The printed structure is embedded in a low-index cladding (not shown). This helps in achieving single-mode operation of the PWB and low fresnel loss due to reflection at the optical surfaces. The inset depicts a schematic drawing of such a structure coupling light from a SiP chip to a SMF.

largely relies on grating couplers (GC) as the prevailing technical implementation [131, 132]. However, despite tremendous progress in optimizing GC efficiency [133], the optical bandwidth is inherently limited to typical values between 40 nm and 50 nm due to the diffractive nature of the structures [134].

In this chapter, a novel approach to highly efficient ultra-broadband out-of-plane coupling is introduced. The concept relies on 3D printed freeform micro-lenses that are connected to on-chip waveguides by photonic wire bonds (PWB) [3]. These lensed PWB (LPWB) exploit the full flexibility of 3D printing and allow for efficient coupling of on-chip waveguides to a wide range of field profiles, thereby offering the possibility to significantly relax alignment tolerances. LPWB can be fabricated in fully automated processes at any position on the chip surface, and the propagation of the received or emitted light can have any orientation with respect to the surface normal. We prove the viability of the concept by coupling silicon strip waveguides to standard single-mode fibres (SSMF). At a centre wavelength of 1550 nm, we achieve a coupling efficiency of $-0.8\,\text{dB}$ along with a 1-dB bandwidth well above 100 nm.

5.2 Design and fabrication

The LPWB comprises a typical silicon-to-polymer waveguide transition in form of a double-taper [3], the photonic wire bond, another taper attached to the lens along with the support structure, see Figures 5.1 and 5.2. The polymer waveguide features a cross-section of $2\,\mu\text{m} \times 1.8\,\mu\text{m}$, combining mechanical stability with single-mode operation, and guides light from the on-chip strip waveguide close to the rear focal plane of the lens. The waveguide is tapered to a square cross-section of $5\,\mu\text{m} \times 5\,\mu\text{m}$ before entering the free-form lens, leading to a moderate beam divergence inside the lens. To achieve single-mode operation for the polymer waveguide and reduced Fresnel reflection at the lens and fibre surfaces, the whole setup is immersed in a low-refractive index oil with refractive index $n_{\text{cladding}} = 1.36$. In a technical application, the oil would be replaced by a low-index cladding material that protects the structure.
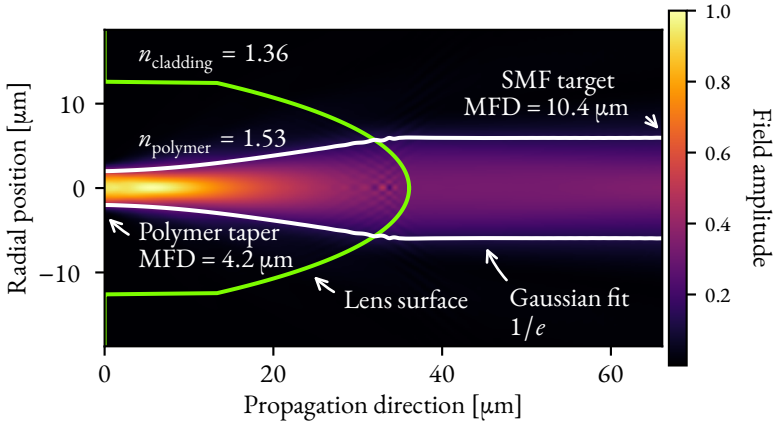
Fig. 5.2: WPM simulation of the propagated field from the polymer taper, through a polymer micro-lens to the target SSMF, placed at a distance of 30 μm from the lens appex. Taper and lens are immersed in oil, which can be replaced by a low-index cladding polymer for permanent mounting. The simulated coupling efficiency of the lens (excluding Fresnel reflections) amounts to $\eta_{\mathrm{Sim}} = -0.2\,\mathrm{dB}$ at 1550 nm. The white contour line marks the radial $1/e^2$ intensity drop of a Gaussian fit at the respective z position.

The axis orientation, working distance and target mode field size of the micro-lens can be freely chosen. We designed our lens for focusing into a SSMF placed at a distance of 30 μm from the lens apex, see Appendix C.1 for more details on how the mode field diameter effects positional and angular alignment tolerances. The rotationally symmetric lens surface is described by a fourth-order polynomial, the coefficients of which were numerically optimized with the help of a wide-angle, unidirectional wave propagation method [75]. A simulation of the electric field magnitude inside the lens section of the LPWB is depicted in Figure 5.2.

The polymer structures were fabricated *in situ* by a single two-photon lithography step in a negative-tone photoresist (IP-Dip, Nanoscribe GmbH). Fully automated fabrication is enabled by detecting position and orientation of the silicon taper. To this end, we combine the data output from an observation camera as well as the data

of a confocal detection unit of the 3D lithography system. The fabrication time of a single structure currently amounts to 7 min, with vast potential for speed improvement by more than an order of magnitude. The fabricated structure is developed in propylene-glycol-methyl-ether-acetate (PGMEA), flushed with isopropanol, and subsequently blow dried. For characterization, most LPWB were fabricated on a standard silicon chip processed in a CMOS line using 193 nm deep-ultraviolet lithography. The tip widths of the inverse tapers amount to typically 120 nm. An additional experiment was carried out using silicon devices structured by electron beam lithography. In both cases the silicon device layer thickness was 220 nm .

5.3 Device characterization

In a first set of experiments, the LPWB couplers were attached to Si strip waveguides, which were connected to standard GC at the other end, see inset of Figure 5.3, and the transmission is measured using a tunable laser source (TLS). The coupling efficiency of the LPWB coupler is then determined by using multiple on-chip GC-GC test structures as a reference. Figure 5.3 depicts the total measured Si-to-fibre coupling efficiency for four nominally identical LPWB, including both the lens-to-SMF interface and the transition of the PWB to the on-chip waveguide. Three of the four structures exhibit a coupling efficiency better than −1 dB. Note that the optical bandwidth of our measurements is limited by the GC as well as by the tuning range of the TLS. Extrapolating the measurement results, we expect that the 1-dB bandwidth is well above 193 nm, thereby outperforming even advanced GC designs. The optimum coupling distance between the LPWB lens apex and the SSMF agreed with simulations within ±5 µm.
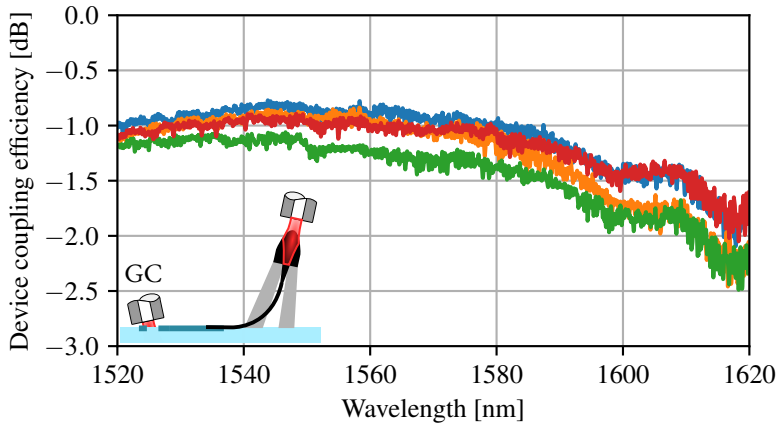
Fig. 5.3: Measured coupling efficiency of a LPWB structures on silicon photonic chips for four nominally identical LPWB connected via a Si strip waveguide coupled to a grating coupler. Together with the tuning range of the light source, measurable LPWB bandwidth is limited but the measurement equipment rather than the LPWB structure.

5.4 Summary

We demonstrate a 3D printed ultra-broadband and highly efficient out-of-plane coupler for photonic integrated circuits. The coupling efficiency at $\lambda_0 = 1550$ nm is -0.8 dB with a 1 dB bandwidth exceeding 200 nm.

[End of Conference Contribution [C16].]

6 Summary and Future Work

The packaging and assembly of photonic integrated systems is the dominant cost-factor of the commercial products. In this work, photonic wire bonds (PWB) are shown to be a viable solution to enable optical multi-chip modules (MCM). These modules combine indium phosphide (InP) light sources with silicon photonic (SiP) chips, and offer record high data rates. In particular, an eight-channel transmitter with an aggregate line rate of $448\,\mathrm{Gbit\,s^{-1}}$ using intensity modulation is shown. A second experiment demonstrates an MCM-based four-channel coherent transmitter, operating at a net data rate of $732.7\,\mathrm{Gbit\,s^{-1}}$ — a record for coherent silicon photonic transmitters with co-packaged lasers. Together, these modules feature 21 functional PWB connections, most of which were PWB that were fabricated in a fully automated fashion. Automation is also used to mass produce 100 photonic wire bonds on a single chip. These are the first photonic wire bonds that reliably demonstrate ultra-low insertion losses of 0.7 dB. In addition, they are covered by a solid cladding material for the first time, which is shown to protect the structures against environmental conditions with no observed failure of a PWB connection. These tests include temperature cycles between $40\,°\mathrm{C}$ and $85\,°\mathrm{C}$, long-term damp heat tests at $85\,°\mathrm{C}$ and 85% relative humidity for more than 3000 h, following the Telcordia standard [93].

Finally, two novel structures are developed and realized in this dissertation: The first structure realizes a broadband polarization beam splitter with integrated rotators using highly birefringent 3D-printed waveguides. The second structure enables efficient and broadband out-of-plane fibre-to-chip coupling by adding a micro-optical lens at the end of a PWB.

The experimental and theoretical findings of this work advance PWB from a pure research topic to a practical application. In fact, the maturity of the process may warrant future research in a more industrial setting, which is witnessed by the fact that many aspects and results of this dissertations have been transferred to a start-up company [135] which is commercializing the photonic wire bonding process.

One promising area of future research is super-resolution lithography and lower shrinkage of the polymerized material. This is of particular importance, since smaller PWB could greatly improve the performance of the PWB connection in an MCM assemblies by enabling truly single-mode or advanced polarization maintaining PWB connections. While current lithography systems are nominally already capable of achieving the required feature size, the polymerized material must be mechanically strong and show minimal shrinkage – both of which has proven difficult. Future material improvements are, however, very likely, considering the many different types of polymer precursors and photoinitiators, many of which can be used for multi-photon lithography.

Another common limitation which typically arises when MCM modules are assembled concerns the relatively short working distances of objectives with high numerical aperture (NA), approximately 300 µm. This small working distance is of particular importance when PWB are fabricated as the last assembly step on fully populated multi-chip modules that include the electronic components. In this case, electrical wire bonds or other electrical components such as bypass capacitors can protrude far enough from the surface of the board to interfere with the objective and its limited working distance. Multiple manufacturers of microscopy equipment are currently releasing high-NA objectives for multi-photon fluorescence imaging deep inside of intact brain tissue. By necessity, these objectives feature a large working distance which could be used to overcome the aforementioned limitation.

Future work will also certainly improve the cladding process, which was only demonstrated for on-chip PWB in this dissertation. Applying the cladding material to chip-to-chip PWB has proven difficult, since the cladding material is usually a liquid that is cross-linked in a subsequent process step. The liquid tends to flow into the gap between chips and subject the PWB to significant capillary forces, often damaging the PWB connection in the process. Solutions to this problems are subject of ongoing research activities [136].

Finally, while the demonstrators in this dissertation were clearly geared towards optical data communication, they may also be used in a wide variety of fields and enable MCM modules with completely new functionality. One field of particular interest is integrated quantum optics. Here, PWB can directly connect to single-photon sources, such as nitrogen-vacancy centres in diamond, to integrated quantum experiments on chips and off-chip single-photon detectors. The resulting module can be very compact and features low thermal mass, which is of particular importance for cryogenic environments.

Appendices

Appendix A

Hybrid Multi-Chip Assembly of Optical Communication Engines by In-Situ 3D Nano-Lithography

The text in this chapter has been published as an appendix of the publication [J7]. It was adapted to fit the layout, structure and notation of this dissertation.

[Start of Appendix of publication [J7].]

A.1 Scalability and stability of photonic wire bonds

For demonstrating environmental stability of photonic wire bonds, five samples were subjected to climate tests. Each chip consists of three independent fields, each field containing 33 PWB bridges, see Figures A.1 and 3.2 of the main manuscript. The cladding is locally deposited in each field. All five samples were tested at 85 °C and 85 % relative humidity according to the standard Telcordia test conditions [93]. One of the samples was additionally exposed to 500 cycles of −40 °C to 85 °C transitions at an average heating/cooling rate of $3\,\mathrm{K\,min^{-1}}$, limited by the performance

100 µm   SiP waveguide   PWB bridges   Low-index cladding   GC
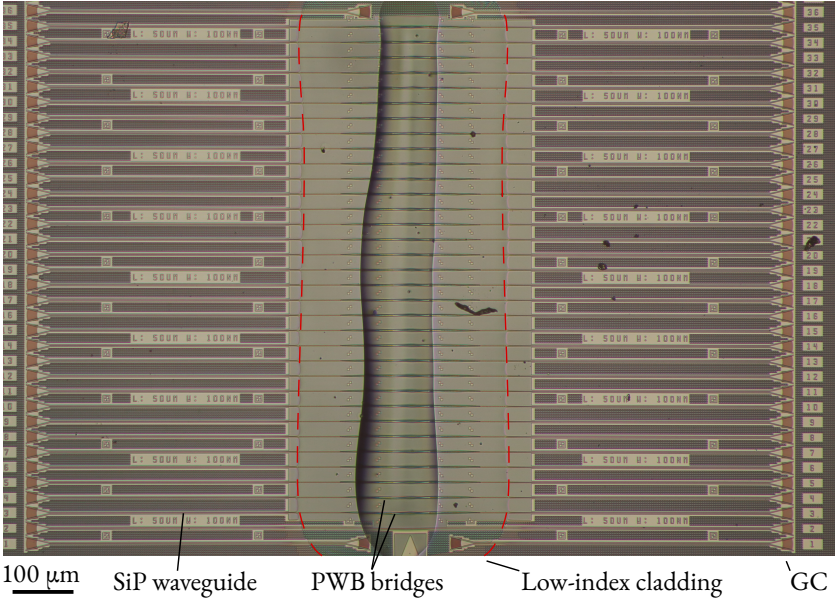
Fig. A.1: Micrograph of a field of densely spaced on-chip PWB bridges connecting down-tapered ends of SiP strip waveguides. The PWB are covered with a protective low-index cladding. Figure 3.2 of the main manuscript shows bare PWB bridge structures prior to applying the cladding material. The sample has been subjected to temperature 500 cycles of $-40\,°C/85\,°C$ in addition to 500 hours of damp heat test at $85\,°C$ and $85\,\%$ relative humidity. No change in transmission nor any physical changes such as delamination of the cladding material from the SiP chip was observed.
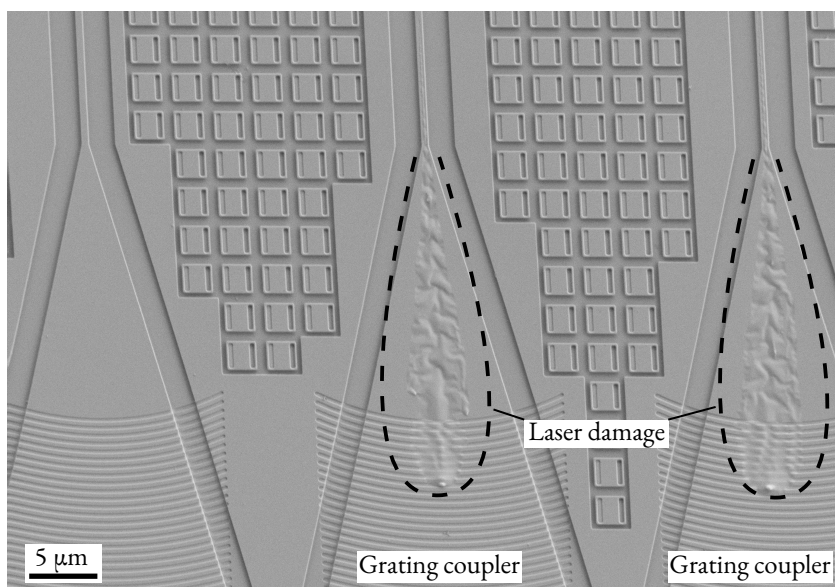
Fig. A.2: High-power testing. In the experiments, we tested the power handling capabilities of structures similar to the ones shown in Supplementary Figure A.1. To this end, CW light at a wavelength of 1550 nm was launched to the input grating coupler (GC) from a standard SMF. The depicted damages occurred at launch powers of approximately 24 dBm in the SMF, which would correspond to 19 dBm of on-chip power taking into account a GC loss of 5 dB. In all experiments, the input GC was destroyed before any damages to the PWB bridges were observed.

of our climate chamber. None of these samples showed any sign of fatigue, such as delamination of the cladding material from the SiP chip, or change in colour, and the PWB transmission remained unchanged. We further tested the power handling capabilities of PWB structures by subjecting them to high-power continuous laser radiation at 1550 nm. We observe that the SiP waveguides were destroyed by nonlinear absorption at approximately 19 dBm of on-chip power before any damage was observed at the PWB bridge, see Figure A.2.

A.2 Demonstration 1: Eight-channel multi-chip transmitter module for intensity modulation and direct detection

A.2.1 Electrical channel cross-talk for intensity modulated eight-channel transmitter

In the experiments described in the main text, the various channels were operated one by one due to the lack of an RF package and an adequate number of drive channels. To confirm that simultaneous operation of all channels is possible, we measure the electrical crosstalk between two neighbouring unterminated modulators using a vector network analyser (VNA), see Figure A.3. To this end, we apply a small-signal modulation to one of the RF input ports of the Mach-Zehnder modulator (MZM) belonging to Channel 7 (Ch 7), and we measure the cross-talk signals at the ends of the transmission lines of the neighbouring MZM belonging to Ch 8 and Ch 6, see green and red trace in Figure A.3. In addition, we determine the direct transmission through the MZM transmission lines of Ch 7 and Ch 8 in a separate measurement, see blue and orange trace in Figure A.3. We obtain an electrical crosstalk of approximately -20 dB or less for the relevant frequency range below 40 GHz. Note that this measurement corresponds to a conservative estimate in the sense that the MZM transmission line of Ch 7 was left unterminated while measuring
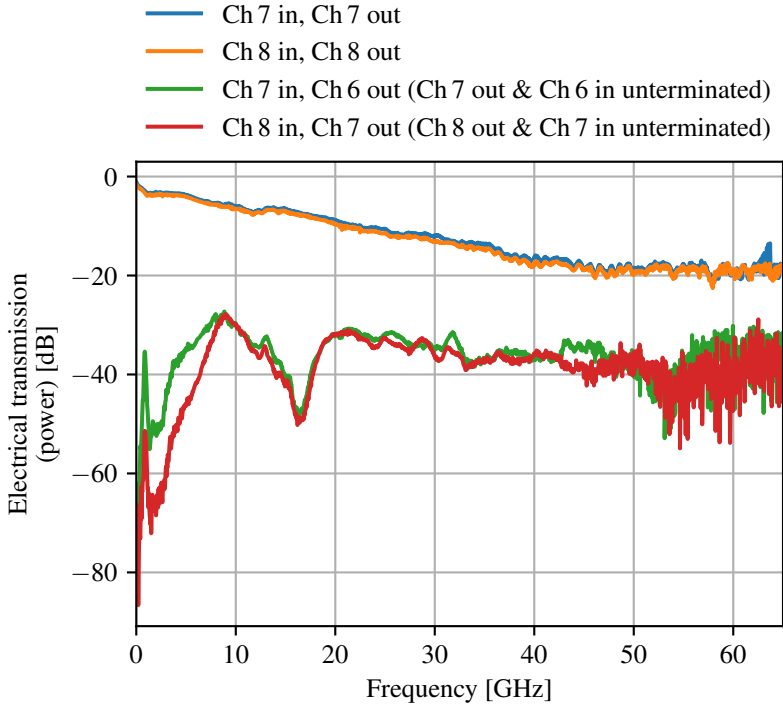
Fig. A.3: Electrical cross-talk of MZM. We measured the cross-talk from the unterminated Channel 2 (Ch 2) to adjacent channels (green and red traces), along with the RF transmission through the MZM transmission lines of Ch 1 and 2 (blue and orange trace).

the cross-talk to the adjacent channels. We expect that proper termination of all MZM transmission lines would further decrease the crosstalk. These experiments indicate that parallel operation on all channels should be possible once dedicated RF boards and driver electronics are available.

A.2.2 Bit-error ratio (BER) estimation of a PAM-4 intensity-modulated signal

Given the limited length of our recordings, we estimate the bit error ratio (BER) based on the measured probability density functions (PDF) at the optimal sampling point. Such approaches are well established for on-off-keying (OOK) signals [137], and models exist for PAM4-signalling [138]. In the following, we extend the existing models by introducing independent Gaussian probability density functions $w_i(u)$ for each level of index i with a mean of u_i and standard deviation of σ_i. In our experiments, the assumption of Gaussian distributions is justified since we did not use any optical amplifiers such that the noise originates predominantly from the electric amplifier at the receiver. In the following, we denote the probability of transmitting a one or a zero with $p(1\mathrm{t})$ or $p(0\mathrm{t})$, respectively. The optimum decision threshold u_{th} for a minimum BER is found by calculating a stationary point of the BER with respect to the decision threshold, i.e., $\mathrm{d}\,\mathrm{BER}/\mathrm{d}\,u_{th} = 0$, where

$$\mathrm{BER} = p\,(1\mathrm{t}) \int_{-\infty}^{u_{\mathrm{th}}} w_1\,(u)\,\,du + p\,(0\mathrm{t}) \int_{u_{\mathrm{th}}}^{+\infty} w_0\,(u)\,\,du \qquad (\mathrm{A.2.1})$$

$$p\,(1\mathrm{t})\,w_1\left(u_{\mathrm{th,opt}}\right) = p\,(0\mathrm{t})\,w_0\left(u_{\mathrm{th,opt}}\right) \qquad (\mathrm{A.2.2})$$

In case of OOK signals, the optimal decision threshold u_{th} is often calculated [137] based on the assumption that the ratio of occurrence probabilities of ones and zeros is equal to the ratio of the corresponding standard deviations, i.e.,

$$p\,(1\mathrm{t})\,/p\,(0\mathrm{t}) = \sigma_1/\sigma_0\,. \qquad (\mathrm{A.2.3})$$

In this case, the optimum decision threshold is found to be

$$u_{\text{th,opt},\sigma} = \frac{u_0 \sigma_1 + u_1 \sigma_0}{\sigma_0 + \sigma_1} . \tag{A.2.4}$$

In our experiments we do not adjust the transmit probabilities of ones and zeros to the associated standard deviations, but rather transmit all symbols with equal probability. The optimal decision threshold $u_{\text{th,opt}}$ and the resulting BER are then given by the optimal decision threshold

$$u_{\text{th,opt}} = \frac{\mu_1 \sigma_0^2 - \mu_0 \sigma_1^2 - \sigma_1 \sigma_0 \sqrt{\mu_0^2 - 2\mu_1\mu_0 + \mu_1^2 + \log\left(\sigma_0^{2\sigma_0^2 - 2\sigma_1^2} \sigma_1^{2\sigma_1^2 - 2\sigma_0^2}\right)}}{\sigma_0^2 - \sigma_1^2} , \tag{A.2.5}$$

and the resulting BER of $u_{\text{th,opt}}$ is found to be

$$\begin{aligned}
\text{BER} = \frac{1}{2} \\
- \frac{1}{4}\text{erf}\left(\frac{\sqrt{2}\mu_0\sigma_1 - \mu_1\sigma_1 + \sigma_0\sqrt{\mu_0^2 - 2\mu_1\mu_0 + \mu_1^2 + \ln(\sigma_0^{2\sigma_0^2 - 2\sigma_1^2} \sigma_1^{2\sigma_1^2 - 2\sigma_0^2})}}{2\sigma_0^2 - 2\sigma_1^2} \right) \\
+ \frac{1}{4}\text{erf}\left(\frac{\sqrt{2}\mu_0\sigma_0 - \mu_1\sigma_0 + \sigma_1\sqrt{\mu_0^2 - 2\mu_1\mu_0 + \mu_1^2 + \ln(\sigma_0^{2\sigma_0^2 - 2\sigma_1^2} \sigma_1^{2\sigma_1^2 - 2\sigma_0^2})}}{2\sigma_0^2 - 2\sigma_1^2} \right) .
\end{aligned} \tag{A.2.6}$$

In case of PAM4, the four signal levels u_i, $i = 1 \dots 4$, can analogously be described by four Gaussian probability density functions. Similarly to OOK, we choose the optimal decision $u_{\text{th,opt},i,j}$ threshold between two adjacent levels u_i and u_j by considering the associated Gaussian distributions of the two adjacent levels similarly to the procedure described in above. Note that this approach assumes negligible contributions of the Gaussian probability density functions that are associated with

additional signal levels u_k that are not adjacent to the considered decision threshold, i.e., for which $k \neq i$ and $k \neq j$. However, when calculating the overall BER, we do include the contribution of erroneously detected symbols that correspond to non-adjacent signal levels, i.e., we take into account the fact that large deviations from the transmitted signal level may result in more than one bit error per symbol. Since the full expression for the PAM-4 bit-error ratio BER_{PAM4} is too long for print, we provide a Python-based computer algebra derivation as a separate code listing A.1. The program allows analysing intensity modulation with an arbitrary number of levels for arbitrary bit-to-level mapping and symbol probabilities.

A.2.3 Data transmission results

For OOK encoded signals, no errors were recorded for all data rates and transmission distances irrespective of the use of post-equalization. The BER could hence only be estimated. For the estimation, we consider the post-equalized signals, since the non-equalized signals suffer from inter-symbol interference (ISI), which renders the assumption of additive white Gaussian noise invalid. For PAM-4 encoded signals, our recordings included errors for high symbol rates and longer distances, as shown in Figure A.4. Note that reliable measurement of the BER requires at least 13 bit errors [137], resulting in an upper boundary of $BER_{measured} \gtrsim 10^{-4}$ for our recordings, which is indicated as a grey bar in Figure A.4. All estimated and directly measured BER are below the of 3.8×10^{-3} limit of hard-decision forward-error correction (HD-FEC) with 7 % coding overhead [95, 104]. Note that the estimated and the measured BER coincide pretty well for the cases where direct BER measurements were possible, indicating the validity of the approach.

Listing A.1: Computer algebra derivation to calculate BER_{PAM4} and BER_{OOK} developed in Python. The program can be adapted to other encoding and symbol probabilities.

```python
from sympy import Symbol, Rational, Eq, solve, oo, integrate, simplify
from sympy.stats import std, density, Normal
from sympy.abc import x
import numpy as np
import collections

encoding_pam4 = [(False, False), (False, True),
                 (True, True), (True, False)]
encoding_ook = [(False, ), (True, )]
encoding = encoding_ook

# Assume all levels are equally likely
level_probabilities = [Rational(1, len(encoding)), ] * len(encoding)
transition_bit_errors = dict()
for level1, level1_bits in enumerate(encoding):
    for level2, level2_bits in enumerate(encoding):
        nr_errors = int(sum(np.logical_xor(level1_bits, level2_bits)))
        transition_bit_errors[(level1, level2)] = Rational(nr_errors,
            len(level1_bits))

# Assume fully independent gaussian distributions:
pdfs = [Normal(f'w_{i}', mean=Symbol(f'mu_{i}'),
               std=Symbol(f'sigma_{i}', positive=True))
        for i in range(len(encoding))]
level_thresholds = [solve(Eq(density(pdf_l)(x),
                            density(pdf_r)(x)), x)[0].simplify()
                    for p_l, pdf_l, p_r, pdf_r
                    in zip(level_probabilities[:-1], pdfs[:-1],
                           level_probabilities[1:], pdfs[1:])]
# Go through all bit error combinations and calculate the bit error
#   probability
# Level 1: Correct level
# Level 2: Wrong level
transition_ber = collections.OrderedDict()
for level1, level1_pdf in enumerate(pdfs):
    for level2, level2_pdf in enumerate(pdfs):
        if level1 == level2:
            continue

        start_integration = (level_thresholds[level2-1]
                              if level2 > 0 else -oo)
        stop_integration = (level_thresholds[level2]
                            if level2 < len(level_thresholds)
                            else oo)

        probability = integrate(density(level1_pdf)(x),
                                (x, start_integration,
                                 stop_integration))
        transition_ber[(level1, level2)] = \
            simplify(probability * level_probabilities[level1]
                     * transition_bit_errors[(level1, level2)])
total_ber = simplify(sum(transition_ber.values()))
print('Total BER', total_ber)
```
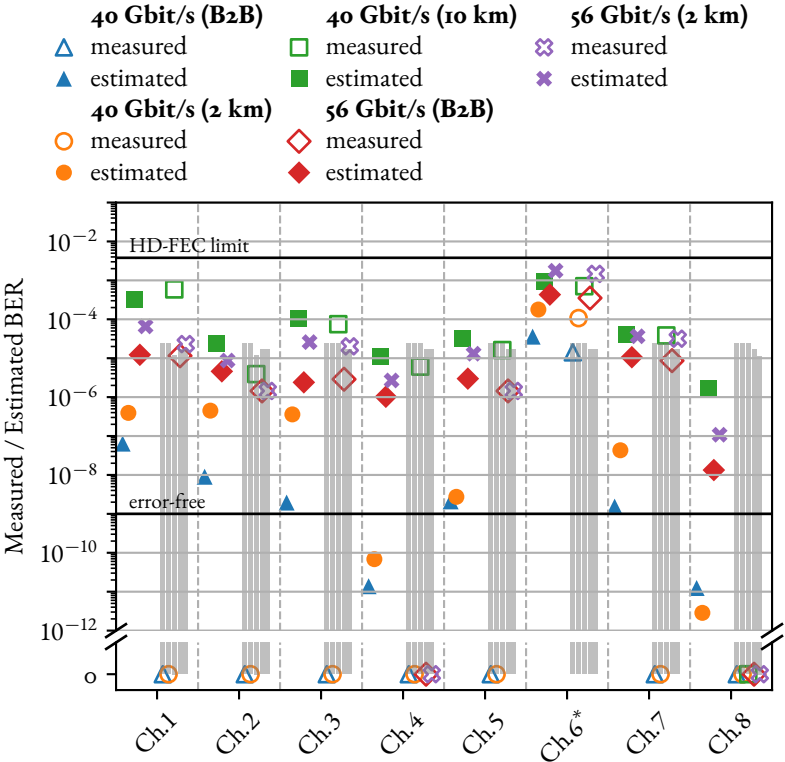
Fig. A.4: Measured (open symbols) and estimated (filled symbols) bit error ratios (BER) of the eight-channel multi-chip module transmitting PAM-4 signals at different symbol rates and over different distances. For all transmission demonstrations, the BER stays below the 7% HD-FEC threshold, including Channel 6, which suffers from additional losses due to an avoidable extra on-chip MMI. The aggregate line rate of the module amounts to 448 Gbit s^{-1}. For each transmission demonstration, the grey bars indicate the BER range for which the measured BER is not statistically relevant since less than 13 errors were detected within the limited recording length which varied between 4.94×10^5 bit and 1.08×10^6 bit. Measured BER values (open symbols) at the very bottom ('BER = 0') indicate measured recordings which did not contain any error.

A.3 Demonstration 2: Four-channel multi-chip transmitter module for coherent communications

The insertion losses (IL) of the PBW connections are obtained by measuring the power levels at various sampling points and by taking into account the grating coupler (GC) losses as well as the losses of the various on-chip components. The GC and component losses were derived from measurements of nominally identical reference structures produced in the same fabrication run as the transceiver chips. Specifically, we measure the power levels P_{launch} at the output SMF of each channel and compare them to the emission power P_{las} of the corresponding HCSEL prior to photonic wire bonding. In addition, we measure the power coupled out of additional on-chip taps at the output of the MZM of each channel. To obtain the emission power P_{las} of each HCSEL, we characterize the devices as described in [50] prior to photonic wire bonding, leading to power levels of 7.4 dBm, 8.4 dBm, 8.6 dBm and 9.0 dBm for Channel 1, 2, 3, and 4 and a drive current of 100 mA, respectively. The corresponding fibre-coupled module output powers P_{launch} amount to −19.9 dBm, −13.6 dBm, −12.9 dBm, and −11.6 dBm, respectively, all measured for maximum transmission of the SOH in-phase/quadrature (IQ) modulators. In this case, the on-chip loss of the SOH IQ amounts to (8.0 ± 0.3) dB, including bus waveguide losses of the order of 1.5 dB. The remaining losses are attributed to non-ideal power splitters, strip-to-slot transitions in the SOH MZM, and imperfectly etched slot waveguides. Based on these measurements, we estimate HCSEL-to-SOI PWB losses of 10.8 dB, 4.9 dB, 4.0 dB, and 6.9 dB for Channel 1, 2, 3, and 4, respectively. The high loss of Channel 1 is caused by a dirt particle sticking to the PWB. The chip-to-fibre PWB losses amount to 8.8 dB, 9.5 dB, 9.2 dB, and 5.5 dB, respectively. Note
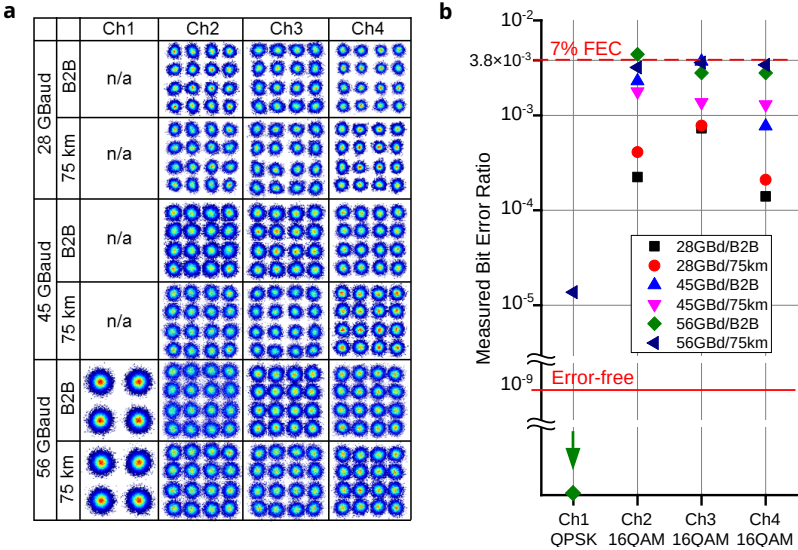
(a) Constellation diagrams for transmission of all channels at 28 GBd, 45 GBd, and 56 GBd. The performance of Ch 1 was impeded by a dirt particle on one of the PWB, leading to a lower launch power, such that only QPSK transmission was successful. For simplicity, we only confirmed error-free transmission performance at the highest symbol rate and did not perform any experiments at 28 GBd or 45 GBd.

(b) Measured bit error ratios (BER) for all channels. Channel 1 (Ch 1) was operated with QPSK only, whereas Ch 2...4 are tested with 16QAM signals. All BER values stay below the threshold for 7 % FEC except for the 56 GBd back-to-back operation (B2B) of Ch 2. Since the BER of the 75 km transmission is below the FEC limit, we attribute this result to a non-optimum adjustment of the modulator bias in the B2B experiment. The aggregate module line rate amounts to 784 Gbit s^{-1}.

Fig. A.5: Coherent transmission experiments, including back-to-back measurements as well as transmission at 45 GBd.

that the module output power used in the transmission experiment is smaller than the maximum achievable launch power P_{launch} due to the modulation loss of the individual MZM and due to the intrinsic 3 dB loss that occurs at the I/Q power combiner when adjusting for an ideal $\pi/2$ phase difference.

For simplicity, Figure 3.12 of the main manuscript only shows the results for 28 GBd and 56 GBd transmission over 75 km. We also performed measurements at 45 GBd as well as back-to-back reference experiments. The results are given in Figure A.5.

[End of Appendix of publication [J7]*.]*

Appendix B

Photonic polarization beam splitter and rotator

The text of this chapter was taken from the Supplementary material of manuscript [J3] that is being prepared for submission. It was adapted to fit the layout, structure and notation of this dissertation.

[Start of Appendix of publication [J3].]

B.1 Measurement of polarization extinction ratio (PER)

We test our PBS structures by measuring the PER over a broad range of wavelengths. To this end, the polarization at the input of the structure is varied randomly by a polarization scrambler, while the Stokes vector and the power at the device output are continuously recorded by a polarimeter, see Figure B.1a for a sketch of the associated setup. The measurement was performed with a commercially available optical component analyser (Keysight N7788B) and was repeated for each of the output ports, thereby revealing the output polarization state of maximum and minimum transmission as well as the associated PER. The PBS test structure used
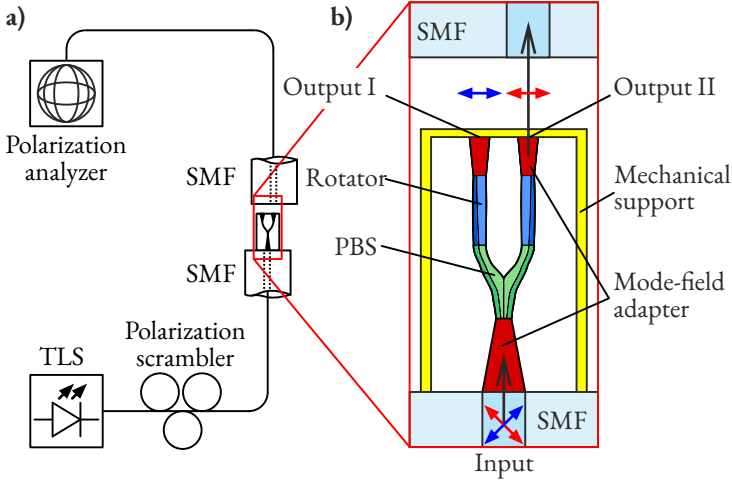
Fig. B.1: Measurement of the polarization extinction ratio (PER) of the PBS with attached polarization rotators (PR). (a) Experimental setup: The PBS is 3D-printed together with the PR and additional mode-field adapters on the facet of an SMF, which is connected to a polarization scrambler. The two output ports are probed by a movable SMF, which is attached to a polarization analyser. The polarization at the input is scrambled randomly, and the power and the Stokes vectors are measured at both outputs. **(b)** Schematic rendering of the PBS (green) with attached PR (blue) and mode-field adapters (red), which are attached to a table-like mechanical support structure (yellow). Orthogonal polarization states (blue and red arrows) at the input port are separated to identical polarization states at the output of the structure.

in this experiment is 3D-printed on the facet of an SMF array which is connected to the polarization scrambler. At the output, the structure is equipped with a pair of polarization rotators (PR), realized by rectangular waveguides that are twisted by 45° along the propagation direction [46, 139], thus providing identical polarizations at both ports, see Figure B.1b. For better probing of the output, the structure is equipped with adiabatic mode-field adapters that are held by a table-like mechanical support structure, see Figure 4.7 of the main manuscript, and that can be individually probed by moving an SMF to the respective port. Note that, due to the unknown
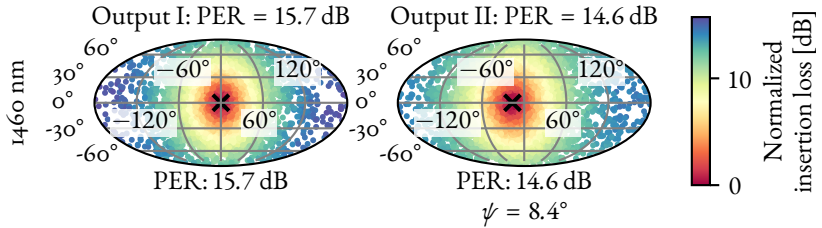
Fig. B.2: Measured output Stokes states of the PBS on the Poincaré sphere in Mollweide projection, coloured by normalized transmitted power. For simplicity, we rotate all measured Stokes vectors such that the polarization state with highest transmitted power at Output I, $\mathbf{s}_{\mathrm{out,pass,1}}$", is oriented along the s_1-direction of the Poincaré sphere (0° longitude and 0° latitude), which corresponds to a linear polarization in horizontal direction, while the predominant polarization state at Output II, $\mathbf{s}_{\mathrm{out,pass,2}}$, is on the equator of the Poincaré sphere, corresponding to a linear polarization at a certain angle ψ with respect to the horizontal direction. We extract only a slight angle deviation of $\psi = -8.4°$ of the two equivalent linear polarization states, indicating correct operation of the PR.

polarization rotation in the SMF, our measurement only allows to determine the exact polarization state at the input of the polarimeter, but not at the output ports of the PBS/PR. This needs to be considered when evaluating the measurement data, see Supplementary Section S3 for details. Note also that the two output ports of our structure are only separated by 25 μm, and we may hence assume that the polarization rotation in the SMF does not change significantly when moving the SMF between the ports. For an ideal device, the two ports should thus exhibit maximum transmission at identical output polarization states.

The measurement results obtained from our test structure at a vacuum wavelength of 1460 nm are depicted in Figure B.2. For this measurement, the input polarization state was scanned across 20 000 points uniformly distributed on the Poincaré sphere. The plot shows the measured Stokes states on the Poincaré sphere in Mollweide projection, coloured by normalized transmitted power. For each of the two device

outputs, we find a predominant polarization state, which we mark by $\mathbf{s}_{\text{out,pass,1}}$ and $\mathbf{s}_{\text{out,pass,2}}$ in Figure B.2. These states correspond to the polarization that would be transmitted to the respective output of a perfect PBS. For a real device with finite PER, the output polarization states $\mathbf{s}_{\text{out,pass,1}}$ and $\mathbf{s}_{\text{out,pass,2}}$ exhibit the highest power transmission. At the same time, the measured output polarization states are concentrated around $\mathbf{s}_{\text{out,pass,1}}$ and $\mathbf{s}_{\text{out,pass,2}}$ in case the input polarization is randomly varied. Note that, for simplicity, we rotated all measured Stokes vectors such that $\mathbf{s}_{\text{out,pass,1}}$ is oriented along the s_1-direction (0° longitude and 0° latitude), which corresponds to a linear polarization in horizontal direction, while $\mathbf{s}_{\text{out,pass,2}}$ is on the equator of the Poincaré sphere, corresponding to a linear polarization at a certain angle ψ with respect to the horizontal direction. Note also that the transformation of the measured output polarizations to linear polarization states is somewhat arbitrary since the true polarization transformation in the output fibre is unknown. Still, we extract only a slight angle deviation of $\psi = -8.4°$ of the two equivalent linear polarization states, indicating a fairly good performance of the polarization rotators.

For each of the output ports, we then extract the polarization extinction ratio (PER), which is here defined as the ratio of the maximum transmitted power at the target output polarization state to the minimum power at the antipodal point on the Poincaré sphere. For better reliability of the extracted results, we implemented a PER evaluation technique that considers all power levels recorded for the various input polarization states rather than just the maximum and the minimum power, see Appendix B.3 for details. The experiment was repeated for different wavelengths over a broad range from 1260 nm to 1620 nm, see Figure 4.8a of the main manuscript for a plot of the extracted PER vs. wavelength. We find that the PER is better than 11 dB over the whole wavelength range, which was only limited by the tuning range of the underlying external-cavity lasers, see Methods of the main manuscript for details. This is slightly worse than the performance expected by simulations, see 4.4 of the main manuscript. We also measured the insertion loss of the device using the polarization state of maximum transmission at each output port. At a wavelength of 1550 nm, we find losses of 4.4 dB and 3.8 dB for Output I and

Output II, respectively. Note that these values include the loss of the PBS, of the subsequent PR, and of the adiabatic mode-field adapters at the input and the output of the device. Still, there is room for improvement considering the sub-2 dB losses expected from simulations of the PBS structure only, see Figure 4.4 of the main manuscript. We attribute the deviations between measurements and simulations to imperfections of the 3D-printed structure, caused by limited resolution and shrinkage of the resist structure upon development. Exploiting super-resolution 3D-lithography inspired by the concept of stimulated-emission-depletion (STED) [64] microscopy might allow to better resolve fine details of the PBS structure and to further enhance the performance of the devices in the future.

B.2 Scattering parameters, Jones matrix, and polarization extinction ratio (PER)

Figure 4.4 of the main manuscript gives the simulated PBS performance in terms of transmission, crosstalk, leakage, unfilterable crosstalk, and PER. The first four parameters are directly extracted from the corresponding elements of the simulated scattering matrix, as indicated in Figure 4.4 and in the main text. For calculating the PER, we use the ratio of the squares of the singular values of the simulated Jones matrices of the PBS[140]. The Jones matrix associated with a certain output port describes the propagation of light from the PBS input port to this output port. In the following, the Jones matrix associated with output port H is denoted as $\mathbf{T}_{\mathrm{PBS},H}$, while $\mathbf{T}_{\mathrm{PBS},V}$ refers to output port V. The Jones vector at the input port is $\mathbf{J}_I = \begin{bmatrix} E_H^{(I)} & E_V^{(I)} \end{bmatrix}^T$, while the Jones vectors at the output ports H and V are $\mathbf{J}_H = \begin{bmatrix} E_H^{(H)} & E_V^{(H)} \end{bmatrix}^T$ and $\mathbf{J}_V = \begin{bmatrix} E_H^{(V)} & E_V^{(V)} \end{bmatrix}^T$. The Jones-matrix elements can be directly taken from the scattering matrix, such that the relations $\mathbf{J}_H = \mathbf{T}_{\mathrm{PBS},H}\mathbf{J}_I$ and $\mathbf{J}_V = \mathbf{T}_{\mathrm{PBS},V}\mathbf{J}_I$ between the Jones vectors and the input and at the output can be written as

$$\begin{bmatrix} E_H^{(H)} \\ E_V^{(H)} \end{bmatrix} = \begin{bmatrix} S_{E_H^{(H)} E_H^{(I)}} & S_{E_H^{(H)} E_V^{(I)}} \\ S_{E_V^{(H)} E_H^{(I)}} & S_{E_V^{(H)} E_V^{(I)}} \end{bmatrix} \begin{bmatrix} E_H^{(I)} \\ E_V^{(I)} \end{bmatrix} \tag{B.2.1}$$

$$\begin{bmatrix} E_H^{(V)} \\ E_V^{(V)} \end{bmatrix} = \begin{bmatrix} S_{E_H^{(V)} E_H^{(I)}} & S_{E_H^{(V)} E^{(I)}} \\ S_{E^{(V)} E^{(I)}} & S_{E^{(V)} E^{(I)}} \end{bmatrix} \begin{bmatrix} E_H^{(I)} \\ E_V^{(I)} \end{bmatrix}. \tag{B.2.2}$$

The PER is then calculated as the ratio of the squares of the singular values s_1 and s_2 of the corresponding Jones matrices [140],

$$\text{PER} = \frac{s_1^2 \left(\mathbf{T}_{\text{PBS},H} \right)}{s_2^2 \left(\mathbf{T}_{\text{PBS},H} \right)} = \frac{s_1^2 \left(\mathbf{T}_{\text{PBS},V} \right)}{s_2^2 \left(\mathbf{T}_{\text{PBS},V} \right)}, \tag{B.2.3}$$

where $s_1 \geq s_2$ without loss of generality.

B.3 PER extraction from the measurements

The PER of an optical device is generally defined as the ratio of maximum to minimum output power P_{out} that can be found when varying the input polarization over all possible states. In our experiments, the input polarization states were sampled randomly, and a straightforward way of calculating the PER is taking the ratio of the maximum to the minimum recorded output power. However, this approach takes into account only two measured power levels, which bears the risk that the result is subject to noise, which could lead to an overestimated PER. In addition, there is no guarantee that the sampled input states will fall close enough to the states of minimum and maximum transmitted power.

We therefore implemented a PER evaluation technique that considers all power levels recorded for the various input polarization states and relies on fitting a theoretical curve to the full set of measurement data. To explain this technique, we consider only one output port of the 3D-printed polarization-beam-splitter/polarization-rotator
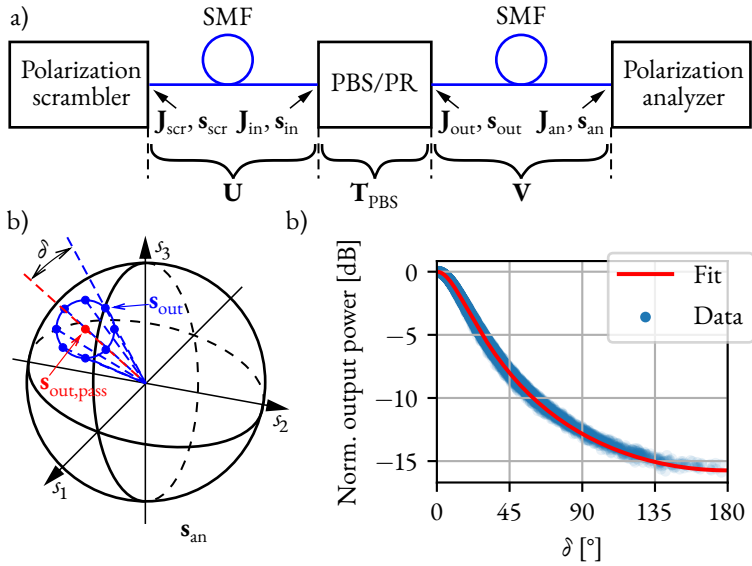
Fig. B.3: Measurement and evaluation of the polarization extinction ratio (PER) of the 3D-printed polarization-beam-splitter/polarization-rotator combination (PBS/PR), taking into account the full set of measured output powers and polarization states. a) Experimental setup: The 3D-printed PBS/PR is fed through a standard single-mode fibre (SMF) by light emitted from a polarization scrambler, and the output power and the output polarization state are measured by a polarization analyser connected to the PBS/PR by a second SMF. $\mathbf{J}_{scr}$, $\mathbf{J}_{in}$ and $\mathbf{J}_{out}$ denote the Jones vectors and the output of the polarization scrambler, the input and the output of the PBS/PR, and at the input of the polarization analyser, while $\mathbf{s}_{scr}$, $\mathbf{s}_{in}$, $\mathbf{s}_{out}$ and $\mathbf{s}_{an}$ denote the corresponding Stokes vectors. The non-ideal PBS/PR is modelled by a Jones matrix $\mathbf{T}_{PBS}$, while the two SMF at the input and the output side of the PBS/PR are represented by two unitary Jones matrices $\mathbf{U}$ and $\mathbf{V}$, respectively. **b)** Illustration of the Stokes vectors recorded by the polarization analyser. Since we assume fully polarized light, all Stokes vectors are on the surface of the Poincaré sphere. The output power should be the same for all polarization states that are located on a circle which is centred about the state of maximum transmission. The radius of this circle is quantified by the opening angle δ of the associated cone. **c)** Normalized output power P_{out} vs. angle δ, as recorded for the data point for Output 1 at a wavelength of 1460 nm, see Figure 4.8a of the main manuscript. By fitting a model function (red) to the measurement data (blue), we extract a field leakage of $\varepsilon = 0.1635$, corresponding to a PER of 15.7 dB.

combination (PBS/PR) – the other output port can be treated in an analogous way. For simplicity, we further assume that the maximum power transmission for the considered port occurs for a perfectly horizontal (x-polarized) polarization at both the input and the output of the PBS/PR, characterized by Stokes vectors $\mathbf{s}_{\mathrm{in,pass}} = \mathbf{s}_{\mathrm{out,pass}} = \begin{bmatrix} 1 & 0 & 0 \end{bmatrix}^{\mathrm{T}}$. Note that the input port can only be accessed through an optical fibre that is connected to the polarization scrambler, and that the measurement of the power and the polarization state at the PBS/PR output requires a second optical fibre leading to the polarization analyser, see Figure B.3a for a sketch of the experimental setup. In the following, we assume fully polarized light such that we can use either Stokes or Jones calculus, as appropriate. We describe the input fibre between the polarization scrambler and the PBS/PR by a Jones matrix $\mathbf{U}$, whereas the output fibre is described by a Jones matrix $\mathbf{V}$, see Figure B.3a. For a given polarization state with Jones vector $\mathbf{J}_{\mathrm{scr}}$ emitted by the polarization scrambler, the Jones vector of the polarization state $\mathbf{J}_{\mathrm{an}}$ received by the polarization analyser can then be written as

$$\mathbf{J}_{\mathrm{an}} = \mathbf{V}\mathbf{T}_{\mathrm{PBS}}\mathbf{U}\mathbf{J}_{\mathrm{scr}}, \tag{B.3.1}$$

where $\mathbf{T}_{\mathrm{PBS}}$ corresponds to the Jones matrix of the non-ideal PBS/PR, and where the Jones matrices $\mathbf{U}$ and $\mathbf{V}$ of the input fibre and the output fibre can be assumed to be unitary, see Figure B.3a. The light at the PBS/PR input can be expressed by an input Jones vector $\mathbf{J}_{\mathrm{in}} = \mathbf{U}\mathbf{J}_{\mathrm{scr}}$, which is characterized by an angle α_{in} that defines the ratio of the field amplitudes in the two polarizations and by a phase difference φ between the x- and the y-component,

$$\mathbf{J}_{\mathrm{in}} = |E_{\mathrm{in}}| \begin{bmatrix} \cos\left(\alpha_{\mathrm{in}}\right) \mathrm{e}^{\mathrm{i}\varphi/2} & \sin\left(\alpha_{\mathrm{in}}\right) \mathrm{e}^{-\mathrm{i}\varphi/2} \end{bmatrix}^{\mathrm{T}}. \tag{B.3.2}$$

In this relation, $|E_{in}|$ denotes the electric field that is associated with the signal at the input of the 3D-printed PBS/PR – the corresponding power is denoted by $P_{in} \sim |E_{in}|^2$. For the PBS/PR, we assume a simplified Jones matrix $\mathbf{T}_{PBS}$ that corresponds to that of a non-ideal linear polarizer oriented along the x-direction,

$$\mathbf{T}_{PBS} = \begin{bmatrix} 1 & 0 \\ 0 & \varepsilon \end{bmatrix}, \tag{B.3.3}$$

where ε, $0 \leq \varepsilon \leq 1$, is the magnitude of the polarization leakage. The corresponding PER is then found as the ratio of the squares of the singular values of $\mathbf{T}_{PBS}$ [140]

$$PER = \frac{1}{\varepsilon^2}. \tag{B.3.4}$$

Note that the model for the Jones matrix according to Eq. (B.3.3) represents an approximation: The Jones matrices $\mathbf{T}_{PBS,H}$ and $\mathbf{T}_{PBS,V}$ that are obtained from our simulations, Eqs. (B.2.1) and (B.2.2), do have non-zero off-diagonal elements and are generally not Hermitian. As a consequence, transformation into a diagonal matrix as assumed in Eq. (B.3.3) is not generally possible. Still, the magnitudes of the off-diagonal elements are small such that the associated error should not be severe, see discussion below.

Using the Jones-matrix model according to Eq. (B.3.3), the relation between a given polarization state, , $\mathbf{J}_{in}$ at the input of the PBS/PR and the corresponding output state $\mathbf{J}_{out}$ can be written as

$$\mathbf{J}_{out} = \mathbf{T}_{PBS}\mathbf{J}_{in} = |E_{in}| \begin{bmatrix} 1 & 0 \\ 0 & \varepsilon \end{bmatrix} \begin{bmatrix} \cos(\alpha_{in})\, e^{i\varphi/2} \\ \sin(\alpha_{in})\, e^{-i\varphi/2} \end{bmatrix}. \tag{B.3.5}$$

We can now express the ratio of the power P_{out} at the output of the PBS/PR to the input power P_{in} in terms of the magnitude of the polarization leakage ε and the angle α_{in},

$$\frac{P_{out}}{P_{in}} = \frac{|E_{out}|^2}{|E_{in}|^2} = |\mathbf{J}_{out}|^2 = \cos^2(\alpha_{in}) + \varepsilon^2 \sin(\alpha_{in}).\qquad(B.3.6)$$

Note that the ratio in Eq. (B.3.6) does not depend on the phase difference φ.

When evaluating the measurement, we face the problem that the angle α_{in} and thus the expression for the power transmission according to Eq. (B.3.6) are related to the Jones vector at the output of the PBS/PR, which cannot be accessed in the measurement. To establish a relationship to the known polarization state $\mathbf{J}_{an}$ at the input of the polarization analyser, we proceed in two steps. First, we switch to Stokes space and we find a relationship that connects the angle α_{in} and the magnitude of the polarization leakage ε in to the angle δ between the actual Stokes vector $\mathbf{s}_{out}$ at the PBS/PR output and the stokes vector $\mathbf{s}_{out,pass} = \begin{bmatrix} 1 & 0 & 0 \end{bmatrix}^T$ that corresponds to maximum transmission. To this end, we first calculate $\mathbf{s}_{out} = \begin{bmatrix} s_{out,1} & s_{out,2} & s_{out,3} \end{bmatrix}^T$ from the components of vector $\mathbf{J}_{out}$ using Equations. (6.1-9a)–(6.1-9d) in Ref. [141]. The angle $\delta \in [0, \pi]$ between the measured Stokes vector $\mathbf{s}_{out}$ and output Stokes vector $\mathbf{s}_{out,pass}$ of maximum transmission can then be calculated as

$$\cos(\delta) = \mathbf{s}_{out} \cdot \mathbf{s}_{out,pass} = \frac{\cos^2(\alpha_{in}) - \varepsilon^2 \sin(\alpha_{in})}{\cos^2(\alpha_{in}) + \varepsilon^2 \sin(\alpha_{in})}\qquad(B.3.7)$$

which can be simplified to

$$\tan\left(\frac{\delta}{2}\right) = \varepsilon \tan(\alpha_{in})\qquad(B.3.8)$$

In a second step, we then account for the propagation of the signal from the PBS/PR output to the polarization analyser. To this end, we exploit the fact that the corresponding Jones vectors $\mathbf{J}_{out}$ and $\mathbf{J}_{an}$ are related by a unitary transformation that is described by the Jones matrix $\mathbf{V}$ of the output fibre. In Stokes space, this

transformation simply corresponds to a rotation about the origin, which leaves the relative angle δ between the measured Stokes vectors $\mathbf{s}_{\text{out}}$ and $\mathbf{s}_{\text{out,pass}}$ unchanged. In other words: For a given polarization leakage magnitude ε, the output power P_{out} should be the same for all polarization states that are located on a circle on the surface of the Poincaré sphere which is centred about $\mathbf{s}_{\text{out,pass}}$, see Figure B.3b for an illustration. We may thus extract this angle directly from the polarization states recorded at the polarization analyser, where $\mathbf{s}_{\text{out,pass}}$ corresponds to polarization state for which the highest output power was measured. We then use Eq. (B.3.5) with ε as a parameter to extract α_{in} and predict the dependence of the power r P_{out} on δ via Eq. (B.3.6), assuming constant P_{in}. We finally vary the magnitude of the polarization leakage ε to find best coincidence between the measured δ-dependence of P_{out} and the associated model prediction, see Figure B.3c. Equation (B.3.4) then allows us to calculate the PER for this value of ε.

We show the results of this technique in Figure B.3c for the highest PER that we measured during our wavelength sweep, i.e., for Output 1 at a wavelength of 1460 nm, see Figure 4.8a. From the least-squares model fit shown in Figure B.3c, we estimate a field leakage ε of 0.1635, corresponding to a PER of 15.7 dB. To check the validity of the approach, we also extract the PER by simply taking the ratio of the maximum and the minimum transmitted power, which leads to value of 16.1 dB. The result is also in line with the expectation that the PER extracted from the ratio of the maximum and the minimum transmitted power might be slightly overestimated due to measurement noise.

B.4 Data transmission experiment

The setup used for data transmission experiment is depicted in Figure B.4 . To generate a 16QAM data stream at a symbol rate of 80 Gbd, a dual-polarization (DP) IQ modulator is driven by a high-speed arbitrary waveform generator (AWG, Keysight M8194A 120 GSa/s) using random bit sequences with different seeds for each polarization. The optical carrier at a wavelength of 1550 nm is provided by an
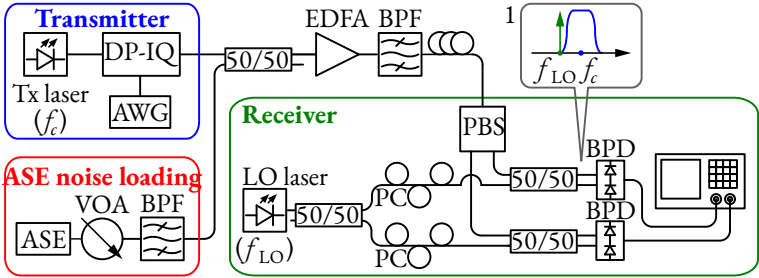
Fig. B.4: Experimental setup for the data-transmission demonstration: An optical carrier at λ_0 = 1550 nm (frequency f_c) is modulated by a dual polarization IQ (DP-IQ) modulator that is driven by an arbitrary waveform generator (AWG) to generate a 16QAM PDM signal at 8 80 GBd. The band-limited amplified-spontaneous-emission (ASE) source generates noise, whose power is varied by a variable optical attenuator (VOA), and added to the 16QAM signal. This noise-loaded data signal is amplified by an EDFA, filtered by a bandpass filter (BPF), and guided to the PBS input in the receiver block. A local oscillator (LO) signal (frequency fLO) is split, and the two split signals are sent through a pair of polarization controllers (PC) and superimposed with the two output signals of the PBS in a pair of balanced photodetectors (BPD). The electrical output signals are detected by a high-speed oscilloscope. Inset 1 illustrates the spectrum at the BPD inputs, with the LO tone tuned to the edge of the signal for heterodyne detection.

external-cavity laser (ECL, Keysight N7714A, emission frequency f_c in Inset 1 of Figure B.4. Root-raised-cosine pulse shaping at a roll-off factor of $\beta = 0.1$ is used for good spectral efficiency. At a BER of 1.25×10^{-2}, which corresponds to the threshold of forward error correction with 15 % coding overhead, see Table 7.5 in Ref. [142] our transmission setup exhibits an OSNR penalty of approximately 3 dB with respect to an ideal transmission system, see Figure 4.8c of the main manuscript. This is in accordance with values in literature for similar modulation formats and symbol rates [129] .

For the OSNR sweep at the receiver, band-limited amplified stimulated emission (ASE) noise is generated by a dedicated ASE noise source (Orion Laser Technology ASE-C/CL) and added to the optical signal (ASE noise loading). The noise-loaded signal is then amplified by an EDFA, filtered by a bandpass filter (BPF, full width at half maximum 1 nm) to suppress out-of-band amplified ASE noise, and sent to the PBS, which may be either a 3D-printed PBS/PR assembly or a commercial fibre-based PBS that we use as a reference. After the PBS, each polarization is detected using a coherent heterodyne scheme, where the local oscillator laser (LO, Keysight N7714A, emission frequency f_{LO} in Inset 1 of Figure B.4) is tuned to the edge of the signal spectrum. Two balanced photodetectors (BPD, Finisar BPDV2150RQ) are used to suppress both signal-signal and LO-LO mixing products. The outputs of the BPD are digitized by a 256 GSa/s real-time oscilloscope (Keysight UXR1004A) and recorded for offline digital signal processing (DSP). In a first DSP step, the signals are made analytic and are shifted in frequency by the difference between the carrier and the LO. After timing recovery, a 2 × 2 MIMO equalizer is used for polarization de-multiplexing, and afterward the carrier recovery is performed. The MIMO equalizer is an adaptive equalizer, whose coefficients are updated according to the radius directed equalization (RDE) [143]. Finally, the signals go through a least-mean-square equalizer before being decoded. To benchmark the performance of the PBS/PR assembly, the experiment is also performed with a commercially

available PBS (AFW Technologies, POBS-15). Since the commercially available PBS exhibits less insertion loss than the PBS/PR-fanout assembly, we adjust the amplification of the preamplifier to obtain equal powers at the inputs of the BPD in both cases.

[End of Appendix of publication [J3].]

Appendix C

Micro-Lenses

This chapter investigates the effect of beam diameters on coupling efficiency. This is of particular interest for micro-lens devices such as the micro-lens attached to a PWB, see Chapter 5. The second part of this chapter derives an analytical solution for constructing such single-surface micro-lenses.

C.1 Gaussian beams and alignment accuracy

In this section, the effect of misaligned optical components on the coupling efficiency are described. The derivation in this paragraph closely follows the results published in Ref. [144]. While the basic results are represented here, the full treatment is instructive and additionally introduces the trade-off of coupling efficiency for relaxed alignment parameters.

A Gaussian beam is often described by its beam waist diameter $2w_0$ at the point of collimation $z = 0$, where the waist radius w_0 describes the drop of the amplitude by a factor of e^{-1}, and a drop of the intensity by a factor of e^{-2}, with respect to its maximum value on the beam axis. At a distance z, the beam phase front acquires a spherical phase front of radius R and curvature $\kappa = 1/R$. Depending on the situation, it is convenient to describe the beam by different pairs of these parameters
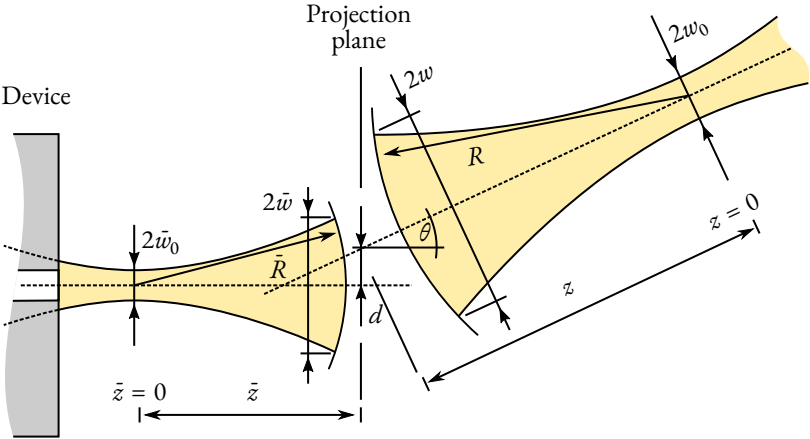
Fig. C.1: Sketch for the calculation of the inner product of two Gaussian beams exhibiting typical alignment errors such as a beam offset d and angular deviation θ at a projection plane. Note that the position of the projection plane can be freely chosen and does not affect the result of the inner product and hence the coupling efficiency. It is convenient to choose $d = 0$. In the case of a 3D treatment of the problem, the problem can only be reduced to the shown 2D representation if the x and y components of the fields can be factorized. In particular, this factorization is not possible for beams that are not coplanar.

$(z, w_0, w$ and $\kappa)$. In case w_0 and z are known, one finds

$$R = \frac{1}{\kappa} = z\left(1 + \left(\frac{kw_0^2}{2z}\right)^2\right) \qquad\qquad \text{(C.1.1)}$$

with

$$
\begin{aligned}
w &= w_0\sqrt{1 + \left(\frac{z}{z_R}\right)^2} & ; & \qquad z_R = \frac{\pi w_0^2}{\lambda} \\
&= w_0\sqrt{1 + \left(\frac{2z}{kw_0^2}\right)^2} & ; & \qquad k = \frac{2\pi}{\lambda}.
\end{aligned}
\qquad \text{(C.1.2)}
$$

Here λ refers to the wavelength inside the medium, and z_R indicates the Rayleigh length, which is the distance along the propagation direction of a beam from the waist at $z = 0$ to the position where the area of the cross section is doubled, and $2z_R$ can be thought of as the depth of focus of a focused beam.

Alternatively, in a local coordinate system at a plane of interest at position z, Eqs. (C.1.1) and (C.1.2) yield the waist radius w_0 for a pair of w and κ,

$$\frac{1}{w_0^2} = \frac{1}{w^2} + \frac{1}{4}\left(kw\kappa\right)^2 . \qquad\qquad \text{(C.1.3)}$$

For distances $z \gg z_R$ the increase in beam width becomes linear and increases at the divergence angle

$$\theta = \lim_{z\to\infty} \arctan\frac{dw}{dz} = \arctan\frac{2w_0}{kw_0^2} = \arctan\frac{\lambda}{\pi w_0} \approx \frac{\lambda}{\pi w_0} . \qquad \text{(C.1.4)}$$

When investigating the coupling efficiency between two devices, e.g., a solid-state laser coupled to an optical fibre, one common approach is to propagate the emitted light all the way to the target device and calculate the inner product with the waveguide mode of the target device. An alternative thought model is shown in

Figure C.1. A Gaussian beam exits the source and intersects at the projection plane with the back-propagated mode of the target device. The inner product of the two Gaussian beams only depends on their respective parameters and hence absorbs details of the source and the target device.

Often, the beam emitted from integrated devices is asymmetric. For the following analysis, one hence assumes the major and minor axis of the beam to be aligned to the x- and y-axis of the coordinate system. The two-dimensional Gaussian beam profile Ψ can then be factored,

$$\Psi\left(x,y\right) = \psi\left(x, w_x, \kappa_x\right)\psi\left(y, w_y, \kappa_y\right) \tag{C.1.5}$$

and the alignment properties of both axes can be treated separately. Without loss of generality, the field ψ, and thereby also $\bar{\Psi}$, is assumed to be normalized such that $\left|\langle\psi|\psi\rangle\right|^2 = 1$. The total coupling efficiency T is given by the squared absolute value of the inner products of the modes. Note however that such a factorization is not possible in general. In particular, this is not possible for beams that are not coplanar.. It that case a full 3D treatment of the coupling problem is required.

If the Gaussian field can be factored, the product of both individual coupling efficiencies (τ_x, τ_y) gives the overall transmission as

$$T = \left|\langle\bar{\Psi}|\Psi\rangle\right|^2 = \underbrace{\left|\langle\bar{\psi}_x|\psi_x\rangle\right|^2}_{\tau_x}\underbrace{\left|\langle\bar{\psi}_y|\psi_y\rangle\right|^2}_{\tau_y}. \tag{C.1.6}$$

C.1.1 Axis-aligned coupling

In case of axes-aligned beams with different waist size and positions, the field at the projection plane is readily described by the local beam waist w and curvature κ as

$$|w,\kappa\rangle = \psi\left(w, \kappa; x\right) = \sqrt[4]{\frac{2}{\pi}}\sqrt{\frac{1}{w}}e^{-\frac{x^2}{w^2}}e^{i\frac{k\kappa x^2}{2}}. \tag{C.1.7}$$

This condition corresponds to $d = 0$ and $\theta = 0$ in Figure C.1. If the coupling is factored into two components per axis, see Eq. (C.1.6), the individual axial contribution per axis is found [145] to be

$$\tau_a = |\langle \bar{w}, \bar{\kappa} | w, \kappa \rangle|^2 = \left| \int_{-\infty}^{+\infty} \psi^* (\bar{w}, \bar{\kappa}; x) \, \psi (w, \kappa; x) \, \mathrm{d}x \right|^2$$

$$= \frac{2}{\sqrt{(\bar{w}/w + w/\bar{w})^2 + \left(\frac{1}{2} k \bar{w} w\right)^2 (\bar{\kappa} - \kappa)^2}} \, . \qquad \text{(C.1.8)}$$

When expressed in minimal beam waists radius $(w_0, \bar{w}_0)$ and position $(z, \bar{z})$, together with Eqs. (C.1.1) and (C.1.2), Eq. (C.1.8) becomes

$$\tau_a = \frac{2}{\sqrt{(\bar{w}/w + w/\bar{w})^2 + (2/(k \bar{w}_0 w_0))^2 (z - \bar{z})^2}} \, . \qquad \text{(C.1.9)}$$

As physically expected, the coupling τ_a is maximized when the optical distance $z - \bar{z}$ between the Gaussian waists vanishes and becomes

$$\tau_a \leq \tau_a \big|_{|z-\bar{z}|=0} = \frac{2}{\bar{w}_0/w_0 + w_0/\bar{w}_0} \, . \qquad \text{(C.1.10)}$$

From Eq. (C.1.6) it is clear that elliptical beams will have a total coupling of $T_a = \tau_{a,x} \tau_{a,y}$, whereas a circular beam is simply given by $T_a = \tau_a^2$. The effect of axial misalignment in case of optical beams with identical waist radii $w_0 = \bar{w}_0$, see Eq. (C.1.9), simplifies to

$$\tau_a \big|_{w_0 = \bar{w}_0} = \frac{2}{\sqrt{4 + (z - \bar{z})^2 / z_R^2}} \, . \qquad \text{(C.1.11)}$$
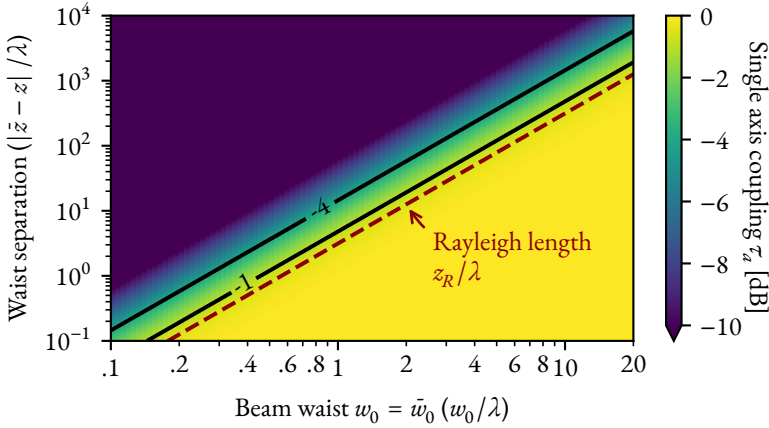
Fig. C.2: Plot of the single axis coupling efficiency τ_a, i.e., the power transferred between a one-dimensional axially aligned Gaussian beam, depending on the separation $|z - \bar{z}|$ of two beam waists of identical size beam waist $w_0 = \bar{w}_0$. All length scales were expressed in terms of wavelength inside the medium λ. The dashed line indicates a separation distance of one Rayleigh length z_R. At this distance the single axis coupling amounts to $10 \log \tau_a (s = z_R) \approx -0.5$ dB. In case of a radial symmetric two-dimensional beam profile, the full power transmission is $T_a = \tau_a^2$ and $10 \log T_a (s = z_R) \approx -1$ dB.

A convenient approximation is $\tau_a (s = z_R)\big|_{w_0 = \bar{w}_0} \approx 0.89$, approximately corresponding to -0.5 dB, when separated by the Rayleigh length $s = z - \bar{z} = z_R$. For axially aligned radially symmetric beams of identical waist, the transmitted power hence drops to -1 dB at a waist separation of the Rayleigh length. It is worth pointing out that τ_a does not follow a Gaussian decay, even though a Gaussian is often fit to measured axial coupling coefficient in literature.

C.1.2 Impact of tilt on coupling efficiency

Angular misalignment of the Gaussian beams can also negatively impact the optical coupling efficiency. Since the z position of the projection plane can be freely chosen without impacting the calculation result, a natural position is the position where $d = 0$. In small-angle approximation, the tilt angle only introduces an additional phase increment $k\theta x$. The mode at $d = 0$ is hence

$$|w, \kappa, \theta\rangle = \psi\left(w, \kappa, \theta; x\right) = \sqrt[4]{\frac{2}{\pi}}\sqrt{\frac{1}{w}}\mathrm{e}^{-\frac{x^2}{w^2}}\mathrm{e}^{\frac{ik\kappa x^2}{2}}\mathrm{e}^{ik\theta x}. \tag{C.1.12}$$

In presence of tilt, the transmittance is found [144] to be a modification of the aligned transmittance τ_a by an exponential decay to e^{-1} at θ_e.

$$\tau_\theta = |\langle \bar{w}, \bar{\kappa}, 0 | w, \kappa, \theta\rangle|^2$$
$$= \tau_a \mathrm{e}^{-(\theta/\theta_e)^2} \tag{C.1.13}$$

$$\theta_e = \frac{2^{3/2}}{k\tau_a\sqrt{\bar{w}^2 + w^2}} \tag{C.1.14}$$

$$= \frac{\sqrt{2}}{\pi\tau_a\sqrt{(\bar{w}/\lambda)^2 + (w/\lambda)^2}} \tag{C.1.15}$$

he result conforms with the intuitive expectation that smaller beams waists will allow larger absolute angular misalignment θ_e due to their larger beam divergence θ, see (C.1.4), and hence decreased relative misalignment.

C.1.3 Impact of lateral offset on coupling efficiency

Lateral offset d along an axis can be treated as a rotation as an infinitesimal rotation $\theta = d/z$ at $z = \infty$ [144]. In the limit $z \rightarrow \infty$, the beam width is dominated by the beam divergence. Using Eq. (C.1.2), gives the limits $\lim_{z \rightarrow \infty} w = 2z/kw_0$ and $\lim_{z \rightarrow \infty} \bar{w} = 2z/k\bar{w}_0$. When introduced in Eqs. (C.1.13) and (C.1.14), one obtains

$$\tau_d = \tau_a e^{-(d/d_e)^2} \tag{C.1.16}$$

with

$$d_e = \frac{\sqrt{2}}{\tau_a \sqrt{\bar{w}_0^{-2} + w_0^{-2}}} \tag{C.1.17}$$

$$= \frac{2^{1/2}}{\tau_a \sqrt{\bar{w}^{-2} + w^{-2} + (2k\bar{w}\bar{\kappa})^{-2} + (2kw\kappa)^{-2}}}, \tag{C.1.18}$$

where τ_d decays to e^{-1} at d_e lateral offset. Note that d_e is minimal when τ_a is maximal, which is the case for zero beam waist separation $|\bar{z} - z| = 0$, see also Eq. (C.1.10).

For the common case of two perfectly matched and radially symmetric Gaussian fields of mode field diameter MFD $= 2w_0 = 2\bar{w}_0$ with zero waist separation $z_0 - \bar{z}_0 = 0$, i.e., $\tau_a = 1$, Eq. (C.1.17) simplifies to $d_e = w_0$. In this specific case, the 1 dB coupling tolerance can be given as

$$d_{1\,\mathrm{dB}} = \sqrt{1/10 \times \ln 10} \times w_0 \approx 0.24 \times \mathrm{MFD}. \tag{C.1.19}$$

C.1.4 Angular-spatial alignment product

When designing optical coupling schemes, a trade-off between acceptable angular and spatial misalignment and beam waist mismatch has to be found. When looking at coupling of Gaussian beams with identical and initially aligned waist. From Eqs. (C.1.14) and (C.1.17) it is clear that a small beam waist will result in a small lateral misalignment distance d_e while featuring a large angular misalignment θ_e, while

the reverse holds true for large beam waists. In fact, d_e or θ_e can be independently arbitrarily large by changing the beam width and sacrificing on θ_e or d_e, respectively. It is also clear that by deliberately introducing a waist mismatch and therefore reducing the aligned coupling efficiency τ_a, the alignment requirements can be further reduced. It is hence convenient to define the alignment product

$$A = \tau_a \theta_e d_e \qquad \text{(C.1.20)}$$

and the normalized alignment product α as

$$\alpha = \frac{kA}{2} = \frac{k\tau_a \theta_e d_e}{2}. \qquad \text{(C.1.21)}$$

With Eqs. (C.1.14) and (C.1.17), the normalized alignment product can be written as

$$\alpha = \frac{\tau_a}{2}\sqrt{\bar{w}^2 + w^2}\sqrt{\bar{w}_0^{-2} + w_0^{-2}}. \qquad \text{(C.1.22)}$$

It can be shown [144] that α is bounded such that $0 < \alpha \le 1$. That is, all possible implementations fall into these bounds. The normalized alignment product α is only unity if one of the following statements holds true [144]:

$$\bar{w}^2 \bar{\kappa} + w^2 \kappa = 0 \stackrel{C.1.3}{\iff} \bar{w}/\bar{w}_0 = w/w_0 \stackrel{C.1.2}{\iff} \bar{w}_0^2/\bar{z} = w_0^2/z. \qquad \text{(C.1.23)}$$

Note that κ and $\bar{\kappa}$ need to be of opposite sign, which is an intuitive indication that the two coupling beams are being focused from both sides of the alignment plane. If unity coupling $\tau_a = 1$ is a design requirement, $\kappa = \bar{\kappa}$ is required. Simultaneously achieving $\alpha = 1$ and $\tau_a = 1$ is hence only possible for $\kappa = \bar{\kappa} = 0$, i.e., both waists fall onto the alignment plane and $\bar{w}_0 = w_0$. The normalized alignment product α is hence a measure for the efficiency of a optical coupling design from a tolerance point of view.
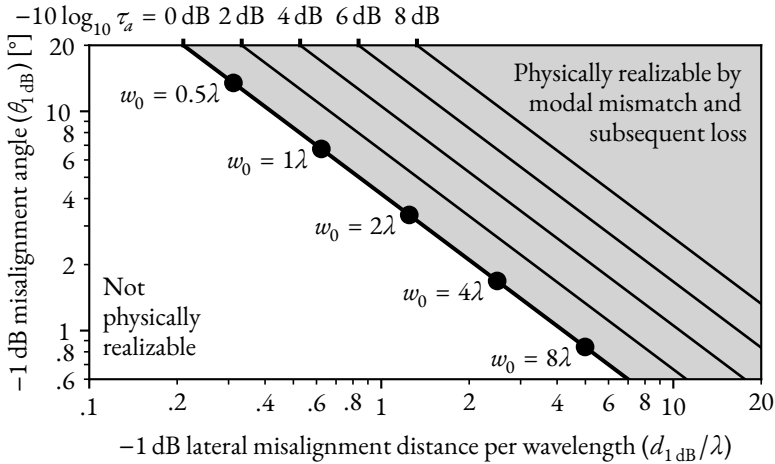
Fig. C.3: Plot of physically realizable 1 dB angular and lateral misalignment tolerance for combinations of coupling beam waists $\bar{w}$ and w, as published by [144]. Each combination will fall inside the grey shaded area. The coupling efficiency τ_a is unity (0 dB) for beam of identical waist $\bar{w} = w = w_0$ and indicated by the thick line at the edge of the shaded area. Several waist sizes w_0 and their associated angular and lateral misalignment tolerance are indicated by black dots.

Knowing the bounds on α, one can now state

$$0 < \frac{\tau_a \theta_e d_e}{\lambda} \leq \frac{1}{\pi} \tag{C.1.24}$$

and specifically for the case $\alpha = 1$ and $\tau_a = 1$, i.e., $w_0 = \bar{w}_0$ and $z = \bar{z}$,

$$\theta_e d_e = \lambda/\pi \,. \tag{C.1.25}$$

Since d_e and θ_e give the reduction in coupling by a factor of e^{-1}, it is often useful to rephrase Eq. (C.1.25) in terms of reduction by a factor corresponding to $-\xi$dB. In that case, d_e and θ_e can be expressed in $d_{\xi\mathrm{dB}}$ and $\theta_{\xi\mathrm{dB}}$ as

$$d_e = \sqrt{\frac{10}{\xi \ln 10}} d_{\xi\mathrm{dB}} \tag{C.1.26}$$

$$\theta_e = \sqrt{\frac{10}{\xi \ln 10}} \theta_{\xi\mathrm{dB}} \, , \tag{C.1.27}$$

respectively.

A plot of the alignment product $d_{1\,\mathrm{dB}}$ and $\theta_{1\,\mathrm{dB}}$ is shown in Figure C.3. All possible implementations fall inside the grey shaded area. The coupling efficiency τ_a is unity (0 dB) for beams of identical waist $\bar{w} = w = w_0$, and it is indicated by the thick line at the edge of the shaded area. Several waist sizes w_0 and their associated angular and lateral misalignment tolerance are indicated by black dots. Note that all spatial distances are scaled in terms of the wavelength in the medium λ. The introduction of a medium will therefore decrease the angular alignment angle θ_e. If an excess loss is acceptable, the coupling beam waists $\bar{w}$ and w may be mismatched, resulting in a lower τ_a but increased tolerances, here indicated by thinner lines in the grey shaded area.
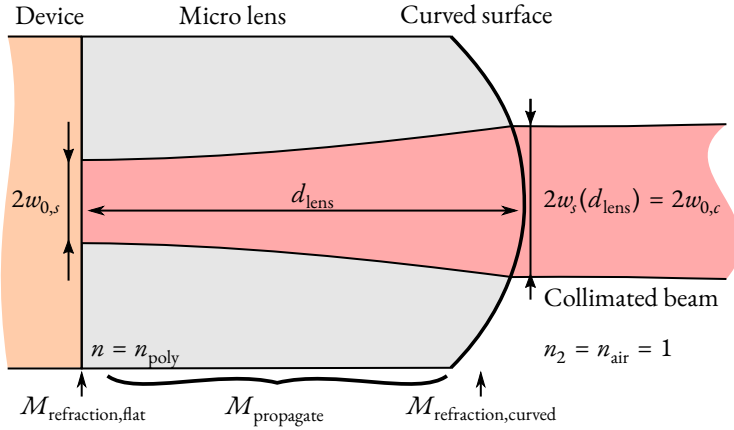
Fig. C.4: Simplified model of a micro-lens attached directly to a chip facet, which collimates the light emitted by chip to a beam of wider diameter. A Gaussian beam with narrow beam waist radius $w_{0,s}$ is emitted by the integrated waveguide. The beam propagates through the polymer with refractive index n_{poly} over a length of d_{lens}. It is collimated by a lens surface. After collimation, the waist of the emitted of radius $w_{0,c}$ is located on the surface of the micro-lens. The micro-lens can be described by a series of transport matrices M. Assuming a beam emitted in air, the light first enters the micro-lens $M_{refraction,flat}$, is transported by a length d_{lens} represented by the transport matrix $M_{propagate}$, after which the light is collimated by the curved surface $M_{refraction,curved}$ of radius R.

C.2 Focal length and size of a micro-lens with a single surface

Light emanating from photonic integrated devices is often highly divergent due to the strong mode confinement inside the device. The resulting mode field of waist radius $w_{0,s}$ requires extreme positional alignment accuracies. By 3D micro-fabrication, micro-lenses can be precisely attached to the device facet and collimate the emitted beam, thereby increasing the effective mode field diameter of the device to manageable sizes. In this paragraph, the typical properties and requirements of such facet-attached micro-lenses is investigated.

In many circumstances, a single optical surface is enough to facilitate efficient coupling between optical devices. Here we investigate the properties of such a single surface micro-lens. Note that this simple model uses paraxial optics, and is only used as a rough starting point for a full wave-optical simulation as demonstrated in Section 2.4. This is of particular importance in case of small beam waists which will result in highly divergent beams exceeding a divergence angle of 11°.

Such a simplified model of a lens is depicted in Figure C.4. The on-axis propagation through such a system can readily be expressed by the commonly used ABCD transfer matrix analysis [72] for optical rays and Gaussian beams. In this example, a Gaussian beam of narrow beam waist radius $w_{0,s}$ is emitted at the facet of a PIC, fibre or even the end of a PWB waveguide. The source beam waist is located directly at the interface to the lens body. Without loss of generality, the beam can be assumed to originate in air and enter the enters directly into the polymer body of the lens, represented by $M_{\text{refraction,flat}}(1, n)$. The beam propagates through the polymer with refractive index n_{poly} over a length of d_{lens}, represented by $M_{\text{propagate}}(d_{\text{lens}})$. It is subsequently collimated by the curved lens surface of radius R, represented by $M_{\text{refraction,curved}}(R, n, n_2)$.

$$
\begin{aligned}
M_{\mu-\text{lens}} &= M_{\text{refraction,curved}}(R, n, n_2) \, M_{\text{propagate}}(d_{\text{lens}}) \, M_{\text{refraction,flat}}(1, n) \quad \text{(C.2.1)} \\
&= \left.\begin{bmatrix} 1 & 0 \\ \frac{(n-n_2)}{n_2 R} & \frac{n}{n_2} \end{bmatrix}\right|_{n_2=1} \cdot \begin{bmatrix} 1 & d_{\text{lens}} \\ 0 & 1 \end{bmatrix} \cdot \begin{bmatrix} 1 & 0 \\ 0 & \frac{1}{n} \end{bmatrix}.
\end{aligned}
$$

In this simplified model, we are interested in the lens length d_{lens} and surface radius R, assuming that the beam waist of the emitted and collimated beam is located directly on the curved lens surface.

The required distance to the lens surface d_{lens} can be readily determined from the propagation of the source laser beam and its increase of $w(z)$ along the propagation in the micro-lens body. The desired target beam radius $w_{0,c}$ is reached at

$$d_{\text{lens}} = z_R \sqrt{\frac{w_{0,c}^2}{w_{0,s}^2} - 1} \quad \text{with } z_R = \frac{\pi w_{0,s}^2 n}{\lambda_0} \, . \tag{C.2.2}$$

A plot of typical lens lengths d_{lens} depending on source and target beam waists according to Eq. (C.2.2) can be found in Figure C.5 for $\lambda_0 = 1550\,\text{nm}$ and $n = n_{\text{poly}} = 1.53$.

An estimate for the lens surface radius of the micro-lens can be derived using the Gaussian beam transfer matrix through the optical system $M_{\mu\text{-lens}}$ under the constraint that the beam waist of the propagated beam is at the position of the lens surface d_{lens}. The resulting curvature is then found to be

$$R = (n-1)\left(\frac{d_{\text{lens}}}{n} + \frac{\pi^2 n}{\lambda_0^2}\frac{w_{0,s}^4}{d_{\text{lens}}}\right) \tag{C.2.3}$$

$$= (n-1)\left(\frac{d_{\text{lens}}}{n} + \frac{z_R^2}{n d_{\text{lens}}}\right) \quad \text{with } z_R = \frac{\pi w_{0,s}^2 n}{\lambda_0} \, .$$

We can derive the focal length of the curved surface from Eq. (C.2.3) using the lensmaker's equation [146]

$$\frac{1}{f} = (n_{\text{lens}} - n_{\text{outside}})\left[\frac{1}{R_1} - \frac{1}{R_2} + \frac{(n_{\text{lens}} - n_{\text{outside}})\, d}{n R_1 R_2}\right], \tag{C.2.4}$$

where d is the thickness of the lens and R_1 and R_2 are the radii of the lens surfaces. Using a single surface R_1 in the thin lens limit, Eq. (C.2.4) becomes

$$f = \frac{1}{(n-1)}R \, . \tag{C.2.5}$$
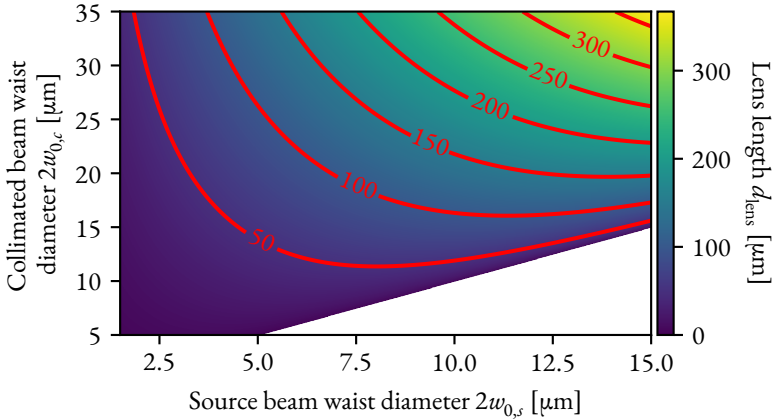
Fig. C.5: Lens length d_{lens} depending on the source beam waist diameter $2w_{0,s}$ and collimated beam waist diameter $2w_{0,c}$ for λ = 1550 nm and $n = n_{\text{poly}}$ = 1.53. In case of medium size source beam waists, such as 10 μm modes of standard C-band single mode fibres, single surface lenses can become longer than 250 μm and subsequently exceedingly difficult to manufacture by multi-photon lithography. In these cases, a multi-surface beam expander may prove a viable alternative. Also note that small beam waists will result in a high divergence angle exceeding 11°. At such high divergence, the paraxial approximation is not a good match. It is therefore advisable to further optimize such lenses based on numerical simulations using the wide-angle wave propagation method (WPM) introduced in Section 2.4.
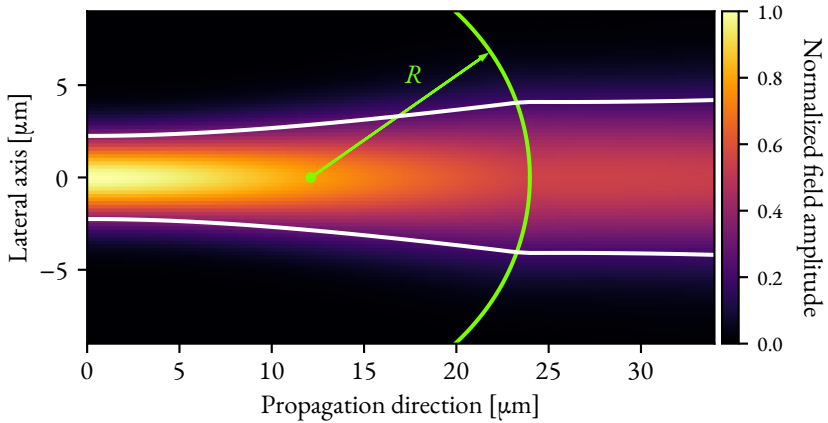
Fig. C.6: Simulated field plot of a collimating micro-lens. The lens is indicated by a green line and collimates a $2w_{0,s}$ = 4.5 μm beam to a $2w_{0,c}$ = 15.5 μm. The lens length is d_{lens} = 23.98 μm with a surface radius of R = 11.86 μm, corresponding to a focal length of f = 22.39 μm in n_{poly} = 1.53 at λ_0 = 1550 nm. In the simulation, 99.7 % of the collimated light is coupled to the target mode field excluding Fresnel reflection on the lens surface. No further optimization to the lens surface were applied. The white line indicates the contour at which the field has dropped by a factor of e^{-1} compared to its peak value along the lateral direction.

The focal length of the micro-lens of surface radius R following C.2.3 is hence

$$f = \frac{d_{\text{lens}}}{n} + \frac{z_R^2}{n d_{\text{lens}}}.$$ (C.2.6)

In case of pure ray optics, the focal length f of a collimating lens would equal to the scaled propagation length inside the thin lens d_{lens}/n. In case of Gaussian beams, focal length is modify by a correction term $z_R^2/(n d_{\text{lens}})$ which depends on the Rayleigh length z_R of the source beam relative to the distance of the length d_{lens}. As expected, the ray optical solution is reproduced in the limit $z_R \ll d_{\text{lens}}$.

Figure C.6 depicts the simulated field plot of a collimating micro-lens designed according to Eqs. (C.2.2) and (C.2.3) using the WPM for wide-angle beam propagation. The lens is indicated by a green line and collimates a $2w_{0,s} = 4.5\,\mu\text{m}$ beam to a $2w_{0,c} = 15.5\,\mu\text{m}$. The lens length is $d_{\text{lens}} = 23.98\,\mu\text{m}$ with a surface radius of $R = 11.86\,\mu\text{m}$, corresponding to a focal length of $f = 22.39\,\mu\text{m}$ in $n_{\text{poly}} = 1.53$ at $\lambda_0 = 1550\,\text{nm}$. In the simulation, 99.7 % of the collimated light is coupled to the target mode field, excluding Fresnel reflection on the lens surface. No further optimization to the lens surface were applied. The white line indicates the contour at which the field has dropped by a factor of e^{-1} compared to its peak value along the lateral direction for each z position.

Appendix D

Lithography processes and hardware

D.1 Multi-photon fluorescence-based process feedback

Multi-photon induced fluorescence can provide a valuable feedback channel for multi-photon lithography. The number of photons required for the generation of a fluorescence photon is usually referred to as the nonlinearity order N. The observed fluorescence intensity is then proportional to the excitation intensity I^N. Multi-photon fluorescence is typically used in the observation of biological samples, where structures of interest are marked by a dye which can be excited multi-photon absorption. In case of multi-photon lithography, where the femtosecond laser is focused into a resist material, there are usually no such dyes. However, the intrinsic fluorescence of the photoinitiator is bright enough in many cases. Multi-photon fluorescence therefore occurs whenever the focus spot is inside the resist material.
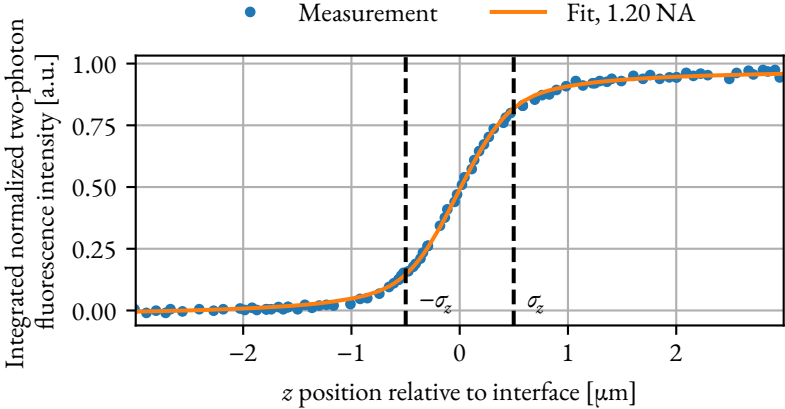
Fig. D.1: Measured and simulated fit of integrated nonlinear fluorescence used for automated detection of a planar interface between glass and a photoresist with matched refractive index ($n_{\text{resist}} \approx 1.518$, fluorescence nonlinearity $N = 2$) using a high-NA microscope objective (64×, NA = 1.4).

D.1.1 Axial voxel resolution estimation and optical interface finding

Since multi-photon fluorescence is generated only locally inside the focal region, sweeping the focus spot and thereby the fluorescence volume axially through a transparent and non-fluorescent planar interface and recording the received fluorescence power as a function of position generates a distinct sigmoid like response. When the focus spot is inside a transparent but non-fluorescent media, such no light is generated, while strong fluorescence is generated inside the resist material. When the voxel is positioned exactly on the interface between the transparent medium and the

resist material, only half the voxel volume fluoresces resulting in exactly half of the maximal observed fluorescence. This technique can be used to implement a method to find the medium-resist interface and is often called 'autofocus'. It is of particular use when aligning to the top surface of PIC or fibres.

The sharpness of the fluorescence change over the axial position of the voxel relative to the optical interface depends heavily on the axial resolution of the objective. The observed fluorescence power $P_{\text{fluo}}(z)$ when positioned at distance z from the optical interface, can be described as

$$P_{\text{fluo}}(z) \propto \int_z^\infty \int_0^\infty \int_0^\pi r^2 \text{IPSF}^N(z, r, \phi) \, \mathrm{d}\phi \, \mathrm{d}r \, \mathrm{d}z', \tag{D.1.1}$$

where $\text{IPSF}(z, r, \phi)$ is the 3D intensity point spread function of the objective in cylindrical coordinates centred at the origin. Unfortunately, there is no closed form expression of IPSF for high numerical aperture objectives, and a numerical simulation of the 3D point spread function is required to calculate the fluorescence response. By fitting the simulated axial fluorescence $P_{\text{fluo}}(z)$ of a perfect objective with varying numerical aperture to the measured data, an effective NA can be determined. Figure D.1 depicts such a measured response with a numeric fit. The experiment was carried out using a photoresist with matched refractive index ($n_{\text{resist}} \approx 1.518$, fluorescence nonlinearity $N = 2$) for a high-NA microscope objective (64×, NA = 1.4). The fit results in an effective axial performance equal to an objective of NA = 1.20, indicating reduced performance of the objective likely caused by a slight remaining refractive index mismatch. The standard deviation of the axial Gaussian intensity distribution of an equivalent objective is indicated by σ_z.
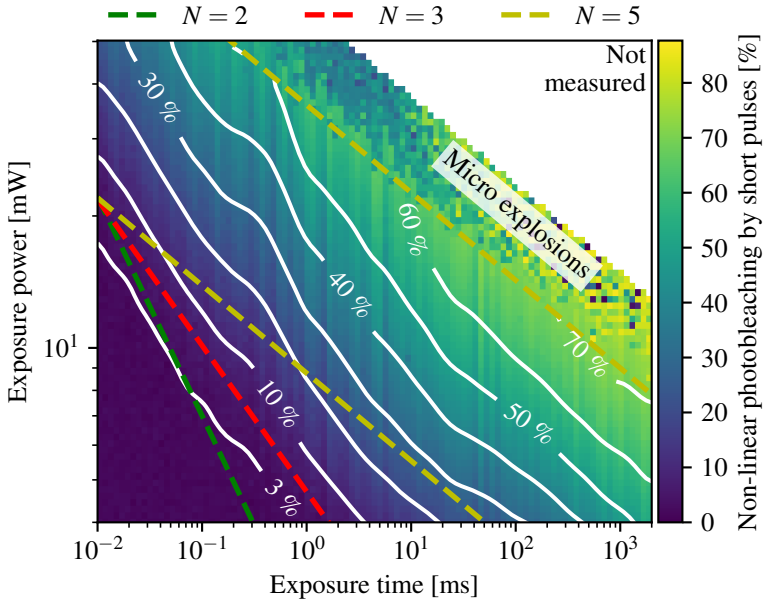
Fig. D.2: Nonlinear photo bleaching of the multi-photon fluorescence of the resist depending of the exposure power and the exposure time of IP-Dip photoresist. The nonlinearity of the process should manifest as straight lines with different slopes in a double logarithmic plot. Contrary to initial expectations, the photo bleaching does not follow a $N = 2$ characteristics of the fluorescence but rather conforms to $N = 3$. The strong variations in the upper right quadrant is caused by the onset of micro-explosions of the photoresist, when the deposited dose exceeds the damage threshold and follows an $N = 5$ nonlinear process.

D.1.2 Investigation of resist destruction threshold and photo bleaching

Multi-photon fluorescence may also be used to characterize the properties of a photoresist. One possible experiment is to investigate photo bleaching by subjecting the sample to a short 'pump' pulse of a variable duration and power. This will cause the photoinitiator to be excited and preferably initiate a polarization process. Either this process or traditional photo bleaching by oxygen termination results in conformal changes to the initiator and loss of nonlinear fluorescence. The luminescence can be measured by a weak 'probe' pulse before and after the 'pump' pulse, and the loss of fluorescence can be determined. Figure D.2 depicts such a measurement for the commercial *IP-Dip* resist. A loss of fluorescence of up to 70 % is observed. It is reasonable to assume that the amount of photo bleaching is proportional to the exited photo-initiators and hence to the deposited dose. For *IP-Dip* the measurements of the polymerization threshold indicate a third order initiation process.

For every photoresist there is a damage threshold above which permanent damage to the resist occurs. In the case of the liquid commercial *IP-Dip* resist, micro-explosions start occurring when the damage threshold of the resist is exceeded. Surprisingly, this damage threshold follows an $N = 5$ process, indicating a five-photon process for a range of four orders of magnitude in exposure time. Since *IP-Dip* is a proprietary resist of *Nanoscribe GmbH & Co. KG* and the composition is hence not publicly known, the origin of this process is not completely clear. However, the ionization of a biphenyl functional group of the resist material exhibits the appropriate ionization energy, and is a likely candidate for the resulting avalanche ionization and the subsequent thermal damage.

D.2 Research DLW lithography system hardware

Data acquisition (NI 6323) from National Instruments

Channel sample rate	250 kHz
Output channels	Galvanometer X&Y; AOM
Input channels	Laser power; Confocal; Fluorescence
Timing resolution	10 ns

Femtosecond fibre laser (C-Fibre 780 HP) from Menlo Systems GmbH

Centre wavelength	$\lambda_{\text{centre}} = (780 \pm 10)\,\text{nm}$
Maximum average output power	$\langle P \rangle_{\text{max}} = 208\,\text{mW}$
Spectral width	17.81 nm
Pulse width	58 fs
Repetition rate	99.81 MHz

Prism femtosecond pulse compressor (FSPC) from Thorlabs

Wavelength range	780 nm to 1050 nm
Group delay dispersion correction at 800 nm	$-12\,500\,\text{fs}^2$ to $0\,\text{fs}^2$
Throughput	$> 75\,\%$

Acousto-optic modulator (MTS40-A3-750.850) from A.A. Sa Opto-Electronic Division

Material	Tellurium dioxide (TeO_2)
Carrier drive frequency	40 MHz
Optical transmission	$> 99\,\%$

Galvanometric scanner (Yanus IV Digital Scan Head) from Thermo Fisher Scientific (former FEI)

Scan field diameter after scan lens	22 mm with $f\theta$-lens with $f = 50$ mm
Full scan field speed ($\pm 8°$)	2000 lines/s
Small scan field speed ($\pm 1°$)	5000 lines/s

Objective scanning system (P-725KHDS) from Physik Instrumente GmbH

Closed-loop travel	400 µm
Closed-loop resolution	2.5 nm
Step-and-settle	20 ms for 400 g objective.

Inverted microscope Axio Observer.Z1 from Carl Zeiss MicroImaging GmbH

Automation	All actuators (filters, motors, port switchers) motorized.
Camera imaging	Side port
Illumination	Through front port, traditionally used for oculars.
Lithography	Through back port, traditionally used for illumination.

Objective Plan-Apochromat 40×/1,4 Oil DIC from Carl Zeiss MicroImaging GmbH

Magnification	40×
Numerical aperture	1.4 in immersion oil Immersol 518F, $n = 1.518$
Working distance	300 nm
Lithography	Through back port, traditionally used for illumination.

Photomultiplier (H10426) from Hamamatsu Photonics

Cathode radiant sensitivity	90 mA W^{-1}
Gain	10^4 to 10^8
High voltage source	internal

Dichroic mirror (DMLP650R) from Thorlabs

Used as a beam splitter to the multi-photon fluorescence detector.

Filter wavelength	λ_{cut} = 650 nm
Type	Long pass

Dichroic mirror (T700DCSPXRUV) from AHF analysentechnik AG

Used after the objective to split illumination and laser path.

Filter wavelength	λ_{cut} = 700 nm
Type	Short pass

Short pass filter (633 SP edge basic) from AHF analysentechnik AG

Used as an addition laser filter in front of the multi-photon fluorescence detector.

Filter wavelength	λ_{cut} = 633 nm
Transmission 400 nm to 615 nm	> 93 %
Suppression 633 nm to 776.5 nm	> 6 optical density (OD), equivalent to a transmission of $T < 10^{-\mathrm{OD}} \times 100\,\% < 0.001\,\%_0$ or < -60 dB

Appendix E

Glossary

E.1 List of abbreviations

16QAM   16-state quadrature amplitude modulation

3D   Three-dimensional

ADC   Analog-to-digital converter

AOM   Acousto-optic modulator

ArF   Argon fluoride

ASE   Amplified spontaneous emission

AWG   Arbitrary waveform generator

BER   Bit-error ratio

BOX   Burried oxide

BPD   Balanced photodetector

BPF   Bandpass filter

BPM   Beam propagation method

BPSK   Binary phase shift keying

CMOS   Complementary metal-oxide-semiconductor

CPU   Central processing unit

DAC	Digital-to-analog converter
DD	Direct detection
DFB	Distributed feedback
DLW	Direct laser writing
DSP	Digital signal processing
ECL	External cavity laser
EDFA	Erbium doped fibre amplifier
EO	Electro-optic
EVM	Error vector magnitude
FDTD	Finite-difference time domain
FEC	Forward error correction
FWHM	Full width at half maximum
GC	Grating coupler
GDD	Group delay dispersion
GPU	Graphics processing unit
GSG	Ground – signal – ground
HCSEL	Horizontal-cavity surface-emitting laser
HD-FEC	Hard decision forward error correction
IL	Insertion loss
IM	Intensity modulation
InGaAsP	Indium gallium arsenide phosphide
InP	Indium phosphide
IQ	In-phase / quadrature phase
IR	Infra-red
ISI	Inter-symbol interference
KrF	Krypton fluoride

LO	Local oscillator
LPWB	Lensed photonic wire bond
MCM	Multi-chip module
MEMS	Microelectromechanical system
MFD	Mode field diameter
MIMO	Multiple Input Multiple Output
MMF	Multimode fibre
MMI	Multimode interference coupler
MPL	Multi-photon lithography
MZM	Mach-Zehnder modulator
NA	Numerical aperture
NIR	Near infrared
NRZ	Non-return to zero
OD	Optical density
OMA	Optical modulation analyser
OOK	On-off keying
OSNR	Optical signal-to-noise ratio
PAM-4	Four-level pulse amplitude modulation
PBS	Polarization beam splitter
PC	Polarization controller
PD	Photodiode
PDL	Polarization dependent loss
PDM	Polarization-division multiplexing
PER	Polarization extinction ratio
PF	Polarization filter
PGMEA	Propylenglycolmonomethyletheracetat

PHOIBOS	Photonic wire bonding for optical multi-chip systems (a BMWF funded project)
PIC	Photonic integrated circuit
PM	Polarization maintaining
PMT	Photomultiplier tube
PR	Polarization rotator
PRBS	Pseudo-random bit sequence
PSF	Point-spread-function
PWB	Photonic wire bond
QAM	Quadrature amplitude modulation
QPSK	Quadrature phase shift keying
RF	Radio frequency
Rx	Receiver
SEM	Scanning electron microscopy
Si	Silicon
SiP	Silicon photonics
SM	Single-mode
SMF	Single-mode fibre
SOH	Silicon-organic hybrid
SOI	Silicon-on-Insulator
SSC	Spot size converter
SSMF	Standard single-mode fibre
STED	Stimulated emission depletion
TE	Transverse electric
TeO_2	Tellurium dioxide
TIR	Total-internal-reflection

TLS	Tunable laser source
TM	Transverse magnetic
Tx	Transmitter
TPA	Two-photon absorption
VNA	Vector network analyser
VOA	Variable optical attenuator
voxel	Volume element
WDM	Wavelength-division multiplexing
WG	Waveguide
WPM	Wave propagation method

E.2 List of mathematical symbols

E.2.1 Greek symbols

α_{in}	Polarization angle of an input Jones vector
ε_0	Dielectric constant
η	Modal mode overlap
$\Theta_{m,z}\left(x,y\right)$	Stencil refractive index function, unity if the refractive index n_m of subregion m in slice at position z is present at lateral position $\left(x,y\right)$, zero in all other cases. See Section 2.4 for details.
κ	Curvature
λ	Wavelength in medium
λ_0	Vacuum wavelength
σ_{xy}	Lateral standard deviation of the 3D Gaussian dose point spread function

σ_z	Axial standard deviation of the 3D Gaussian dose point spread function
φ_{in}	Phase of an input Jones vector

E.2.2 Latin symbols

c	Vacuum speed of light
d_{1dB}	1-dB lateral alignment tolerance
D	Dispersion coefficient
$\mathcal{D}$	Deposited lithographic dose
$\mathcal{D}_{\mathrm{th}}$	Threshold deposited lithographic dose above which the resist becomes insoluble.
E	Field
f	Focal length
h	Planck's constant
P	Power
h_{tip}	Silicon taper tip height
n	Refractive index
n_{clad}	Refractive index of the PWB cladding material
n_{core}	Refractive index of the PWB core material
n_{oil}	Refractive index of oil used as PWB cladding material
n_{eff}	Effective refractive index
R	Radius
$\mathbf{S}$	Stokes vector
$\mathbf{s}$	Normalized Stokes vector
s	Geodesic distance
$s_i\,(\mathbf{A})$	Singular value of matrix $\mathbf{A}$; i-th value sorted by decreasing value

U_π	π-voltage
u_{th}	decision threshold
w_{tip}	Silicon taper tip width
w_0	Beam waist radius of a Gaussian beam
Δz	Simulation step distance in z direction
z_R	Rayleigh length; the distance from the beam waist along the propagation direction of a Gaussian beam to where the waist radius increased by a factor of $\sqrt{2}$

Anhang F

Danksagung

Die vorliegende Dissertation entstand während meiner Tätigkeit am Institut für Photonik und Quantenelektronik (IPQ), sowie dem Institut für Mikrostrukturtechnik, am Karlsruher Institut für Technologie (KIT). Die wissenschaftliche Arbeit war eingebettet in die Forschungsprojekte PHOIBOS und PRIMA, beide gefördert vom Bundesministerium für Bildung und Forschung (BMBF), sowie PIXAPP und BigPipes, welche beide von der Europäischen Union (EU) gefördert wurden. Ausdrücklich bedanken möchte ich mich für das Stipendium der Helmholtz International Research School for Teratronics.

Eine Vielzahl an Personen haben mich in der Entstehung der vorliegenden Arbeit unterstützt und diese ermöglicht. Ihnen allen gilt mein herzlicher Dank. Einigen möchte ich an dieser Stelle meinen ganz besonderen Dank entgegenbringen.

Meinem Doktorvater Professor Christian Koos möchte ich besonders für das mir entgegengebrachte Vertrauen und hohe Interesse an meiner Arbeit danken. Seine Ideen, Vorschläge und Ratschläge haben wesentlich zur Entstehung dieser Arbeit beigetragen. Außerordentlich dankbar bin ich für das mir entgegengebrachte Vertrauen, das es mir ermöglicht hat ohne komplizierte Beschaffungsprozesse ein eigenes Lithographiesystem zu entwickeln – was bis heute meinen beruflichen Werdegang prägt.

Herrn Professor Wolfgang Freude gilt mein herzlicher Dank für die Betreuung als Korreferent, die offenen und fruchtbaren Diskussionen, sowie die gründlichen und sehr konstruktiven Korrekturen der Ausarbeitungen.

Bei Prof. Sebastian Randel möchte ich mich insbesondere für die praktische Unterstützung bedanken. Seine Programmsammlungen waren bei der Auswertung von Datenübertragungsexperimenten von immenser Hilfe.

Meine Arbeiten am PHOIBOS Projekt ermöglichten mir auch einen mehrwöchigen Aufenthalt in der zentralen Forschung bei der Carl Zeiss AG in Jena. Für diese spannende Zeit im Laserlabor in einem kollegialen Umfeld möchte ich mich Philipp Hübner, Stefan Richter, sowie Gerhard Krampert bedanken.

Weiterhin gilt mein Dank Herrn Prof. Jeremy Witzens und Florian Merget von der RWTH Aachen für die Organisation der Chipfertigung bei IME im Rahmen des BigPipes Projektes.

Von ganz besonderer Bedeutung ist Raum 2.22, welcher über fast ein Jahrzehnt drei Generationen aus Doktoranden eine Heimat rund um das Thema Mikrostrukturtechnik bot. Diese sind insbesondere Nicole Lindenmann, Tobias Hoose, Muhammad Rodlin 'Oding' Billah, Yilin Xu und Pascal Maier. Ohne das absolute gegenseitige Vertrauen und die weitreichende Kooperation wäre dieser Staffellauf nicht möglich gewesen. Ich freue mich sehr, euch alle auch privat Freunde zu nennen. Uns alle verbindet eine lebenslange Liebe für Kamele.

Hat man die 3D Mikrostrukturierung einmal gemeistert, so lässt sich diese Technik sehr breit einsetzen. Für die konstruktive Zusammenarbeit in den vielen gemeinsamen Forschungsprojekten möchte ich mich auch bei Theodoros Anagnos, Philipp-Immanuel Dietrich, Denis Ganin, Gerald Göring, Sebastiaan Haffert, Robert Harris, Tobias Harter, Wladislaw Hartmann, Juned Kemal, Clemens Kieninger, Daria Kohler, Yasar Kutuvantavida, Pablo Marin-Palomo, Sascha Mühlbrandt, Fernando Negredo, Aleksandar Nesic, Mareike Trappen, Sandeep Ummethala bedanken. Nur in der Promotion bekommt man die Gelegenheit, zu einer Vielzahl von Themen beizutragen, darunter photonische Strahlteiler, Mikrooptiken, optisches

Danken möchte ich auch meinem Arbeitgeber Nanoscribe für das Verständnis und die fortwährende Unterstützung beim Fertigstellen dieser Arbeit. Umso mehr freut es mich, hier wieder meine ehemaligen Kollegen Nicole, Tobias und Mareike zu treffen. Ein gutes Team bleibt einfach zusammen!

Vielen Dank an alle meine Freunde – ihr seit die Besten! Besonderen Dank geht an Julia, die immer ein offenes Ohr hatte und mir die Erfahrung ihrer eigenen Promotion berichten konnte.

Ein großer Dank gilt meinen Eltern Andrea und Martin sowie meinem Bruder Christian Blaicher. Egal, was auch kam, ich konnte mir immer sicher sein, dass ihr mich unterstützt und hinter mir steht. Vielen Dank dafür.

Meinem Schatz Mareike Seitz danke ich für die fortwährende Unterstützung, ihre Liebe und ihr Verständnis für die Zeit, die dieses Dokument in Anspruch genommen hat.

Appendix G

List of publications

G.1 Articles

The [†] symbol indicates equal contribution by the authors.

J1. Xu, Y., Kuzmin, A., Knehr, E., **Blaicher, M.**, Ilin, K., Dietrich, P.-I., Freude, W., Siegel, M. & Koos, C. 'Superconducting Nanowire Single-Photon Detector with 3D-printed Free-Form Microlenses'. *Optics Express* **29,** 27708–27731 (16th Aug. 2021).

J2. Anagnos, T., Trappen, M., Tiong, B. C. K., Feger, T., Yerolatsitis, S., Harris, R. J., Lozi, J., Jovanovic, N., Birks, T. A., Vievard, S., Guyon, O., Gris-Sánchez, I., Leon-Saval, S. G., Norris, B., Haffert, S. Y., Hottinger, P., **Blaicher, M.**, Xu, Y., Betters, C. H., Koos, C., Coutts, D. W., Schwab, C. & Quirrenbach, A. '3D-M3: High-spatial Resolution Spectroscopy with Extreme AO and 3D Printed Micro-Lenslets'. *Applied Optics* **60,** D108–D121 (1st July 2021).

J3. Nesic[†], A., **Blaicher[†], M.**, Pablo Marin-Palomo, Freude, W. & Koos, C. 'Ultra-Broadband Polarization Beam Splitter and Rotator Based on 3D-printed Waveguides'. *(submitted)* (9th June 2021).

J4.   Sebastiaan Y. Haffert, Harris, R. J., Zanutta, A., Pike, F. A., Bianco, A., Redaelli, E. M. A., Benoît, A., MacLachlan, D. G., Ross, C. A., Gris-Sánchez, I., Trappen, M. D., Xu, Y., **Blaicher, M.**, Maier, P., Riva, G., Sinquin, B., Kulcsár, C., Bharmal, N. A., Gendron, É., Staykov, L., Morris, T. J., Barboza, S., Münch, N., Bardou, L. F., Prengère, L., Raynaud, H.-F. G., Hottinger, P., Anagnos, T., Osborn, J., Koos, C., Thomson, R. R., Birks, T. A., Snellen, I. A. G. & Keller, C. U. 'Diffraction-Limited Integral-Field Spectroscopy for Extreme Adaptive Optics Systems with the Multicore Fiber-Fed Integral-Field Unit'. *Journal of Astronomical Telescopes, Instruments, and Systems* **6,** 045007 (23rd Dec. 2020).

J5.   Trappen, M., **Blaicher, M.**, Philipp-Immanuel Dietrich, Dankwart, C., Xu, Y., Hoose, T., Billah, M. R., Abbasi, A., Baets, R., Troppenz, U., Theurer, M., Wörhoff, K., Seyfried, M., Freude, W. & Koos, C. '3D-printed Optical Probes for Wafer-Level Testing of Photonic Integrated Circuits'. *Optics Express* **28,** 37996–38007 (7th Dec. 2020).

J6.   Helge Gehring[†], **Blaicher[†], M.**, Grottke, T. & Pernice, W. 'Reconfigurable Nanophotonic Circuitry Enabled by Direct-Laser-Writing'. *IEEE Journal of Selected Topics in Quantum Electronics* **26,** 4400905 (25th June 2020).

J7.   **Blaicher[†], M.**, Billah[†], M. R., Juned Kemal, Hoose, T., Marin-Palomo, P., Hofmann, A., Kutuvantavida, Y., Kieninger, C., Dietrich, P.-I., Lauermann, M., Wolf, S., Troppenz, U., Möhrle, M., Merget, F., Skacel, S., Witzens, J., Randel, S., Freude, W. & Koos, C. 'Hybrid Multi-Chip Assembly of Optical Communication Engines by in Situ 3D Nano-Lithography'. *Light: Science & Applications* **9,** 71 (27th Apr. 2020).

J8.   Hoose, T., **Blaicher, M.**, Kemal, J. N., Zwickel, H., Billah, M. R., Dietrich, P.-I., Andreas Hofmann, Freude, W., Randel, S. & Koos, C. *Hardwire-Configurable Photonic Integrated Circuits Enabled by 3D Nano-Printing*. 19th Dec. 2019. arXiv: 1912.09942 [physics].

J9.   Dietrich[†], P.-I., Gerald Göring[†], Trappen[†], M., **Blaicher, M.**, Freude, W., Schimmel, T., Hölscher, H. & Koos, C. '3D-Printed Scanning-Probe Microscopes with Integrated Optical Actuation and Read-Out'. *Small* **16,** 1904695 (5th Dec. 2019).

J10.   Gehring[†], H., **Blaicher[†], M.**, Hartmann, W. & Pernice, W. H. P. 'Python Based Open Source Design Framework for Integrated Nanophotonic and Superconducting Circuitry with 2D-3D-hybrid Integration'. *OSA Continuum* **2,** 3091–3101 (15th Nov. 2019).

J11.   Tobias Harter, Sandeep Ummethala, **Blaicher, M.**, Sascha Mühlbrandt, Wolf, S., Weber, M., Adib, M. M. H., Kemal, J. N., Merboldt, M., Boes, F., Nellen, S., Tessmann, A., Walther, M., Globisch, B., Zwick, T., Freude, W., Randel, S. & Koos, C. 'Wireless THz Link with Optoelectronic Transmitter and Receiver'. *Optica* **6,** 1063–1070 (20th Aug. 2019).

J12.   Nesic, A., **Blaicher, M.**, Hoose, T., Hofmann, A., Lauermann, M., Kutuvantavida, Y., Nöllenburg, M., Randel, S., Freude, W. & Koos, C. 'Photonic-Integrated Circuits with Non-Planar Topologies Realized by 3D-printed Waveguide Overpasses'. *Optics Express* **27,** 17402–17425 (10th June 2019).

J13.   Gehring[†], H., **Blaicher[†], M.**, Hartmann, W., Varytis, P., Busch, K., Wegener, M. & Pernice, W. H. P. 'Low-Loss Fiber-to-Chip Couplers with Ultrawide Optical Bandwidth'. *APL Photonics* **4,** 010801 (1st Jan. 2019).

J14.   Billah, M. R., **Blaicher, M.**, Hoose, T., Dietrich, P.-I., Marin-Palomo, P., Lindenmann, N., Nesic, A., Hofmann, A., Troppenz, U., Möhrle, M., Randel, S., Freude, W. & Koos, C. 'Hybrid Integration of Silicon Photonics Circuits and InP Lasers by Photonic Wire Bonding'. *Optica* **5,** 876 (20th July 2018).

J15. Clemens Kieninger, Yasar Kutuvantavida, Elder, D. L., Wolf, S., Zwickel, H., **Blaicher, M.**, Kemal, J. N., Lauermann, M., Randel, S., Freude, W., Dalton, L. R. & Koos, C. 'Ultra-High Electro-Optic Activity Demonstrated in a Silicon-Organic Hybrid Modulator'. *Optica* **5,** 739 (20th June 2018).

J16. F. Negredo, **Blaicher, M.**, Nesic, A., Kraft, P., Ott, J., Dörfler, W., Koos, C. & Rockstuhl, C. 'Fast and Reliable Method to Estimate Losses of Single-Mode Waveguides with an Arbitrary 2D Trajectory'. *JOSA A* **35,** 1063–1073 (1st June 2018).

J17. Dietrich, P.-I., **Blaicher, M.**, I. Reuter, Billah, M., Hoose, T., Hofmann, A., Caer, C., Dangel, R., Offrein, B., Troppenz, U., Möhrle, M., Freude, W. & Koos, C. 'In Situ 3D Nanoprinting of Free-Form Coupling Elements for Hybrid Photonic Integration'. *Nature Photonics* **12,** 241–247 (26th Apr. 2018).

J18. Dietrich[†], P.-I., Harris[†], R. J., **Blaicher, M.**, Corrigan, M. K., Morris, T. J., Freude, W., Quirrenbach, A. & Koos, C. 'Printed Freeform Lens Arrays on Multi-Core Fibers for Highly Efficient Coupling in Astrophotonic Systems'. *Optics Express* **25,** 18288–18295 (24th July 2017).

J19. Göring, G., Dietrich, P.-I., **Blaicher, M.**, Sharma, S., Korvink, J. G., Schimmel, T., Koos, C. & Hölscher, H. 'Tailored Probes for Atomic Force Microscopy Fabricated by Two-Photon Polymerization'. *Applied Physics Letters* **109,** 063101 (8th Aug. 2016).

G.2 Conference proceedings

The [†] symbol indicates equal contribution by the authors.

C1.   Anagnos, T., Maier, P., Hottinger, P., Betters, C. H., Feger, T., Leon-Saval, S. G., Gris-Sánchez, I., Yerolatsitis, S., Lozi, J., Birks, T. A., Vievard, S., Jovanovic, N., Rains, A. D., Ireland, M. J., Harris, R. J., Tiong, B. C. K., Guyon, O., Norris, B., Haffert, S. Y., **Blaicher, M.**, Xu, Y., Straub, M., Pott, J.-U., Sawodny, O., Neureuther, P. L., Coutts, D. W., Schwab, C., Koos, C. & Quirrenbach, A. 'An Innovative Integral Field Unit Upgrade with 3D-printed Micro-Lenses for the RHEA at Subaru'. in *Advances in Optical and Mechanical Technologies for Telescopes and Instrumentation IV* Advances in Optical and Mechanical Technologies for Telescopes and Instrumentation IV. **11451** (International Society for Optics and Photonics, 13th Dec. 2020), 114516Y.

C2.   Haffert, S. Y., Harris, R. J., Zanutta, A., Pike, F. A., Bianco, A., Redaelli, E., Benoît, A., MacLachlan, D. G., Ross, C. A., Gris-Sánchez, I., Trappen, M. D., Xu, Y., **Blaicher, M.**, Maier, P., Riva, G., Sinquin, B., Kulcsár, C., Bharmal, N. A., Gendron, E., Staykov, L., Morris, T. J., Barboza, S., Muench, N., Bardour, L., Prengère, L., Raynaud, H.-F., Hottinger, P., Anagnos, T., Osborn, J., Koos, C., Thompson, R. R., Birks, T. A., Snellen, I. A. G., Keller, C. U., Close, L. & Males, J. R. 'Multi-Core Fibre-Fed Integral-Field Unit (MCIFU): Overview and First-Light'. in *Adaptive Optics Systems VII* Adaptive Optics Systems VII. **11448** (International Society for Optics and Photonics, 13th Dec. 2020), 114484M.

C3.   Trappen, M., Dietrich, P.-I., Burger, P., **Blaicher, M.**, Göring, G., Schimmel, T., Freude, W., Hölscher, H. & Koos, C. 'AFM Engine with Optical Actuation and Readout Printed on the Facet of a Multi-Core Fiber'. in. Conference on Lasers and Electro-Optics (CLEO) (OSA, May 2020), SM2N.7.

C4.   Gehring, H.**, Blaicher, M.,** Eich, A., Hartmann, W., Varytis, P., Varytis, P., Busch, K., Busch, K., Schuck, C., Wegener, M., Wegener, M. & Pernice, W. H. P. 'Broadband Fiber-to-Chip Coupling in Different Wavelength Regimes Realized by 3D-structures'. in *Conference on Lasers and Electro-Optics (2020), Paper JTh2B.22* CLEO: Science and Innovations (Optical Society of America, 10th May 2020), JTh2B.22.

C5.   Xu[†], Y., Maier[†], P., **Blaicher, M.**, Dietrich, P.-I., Marin-Palomo, P., Hartmann, W., Billah, M. R., Troppenz, U., Möhrle, M., Randel, S., Freude, W. & Koos, C. 'InP/Silicon Hybrid External-Cavity Lasers (ECL) Using Photonic Wirebonds as Coupling Elements'. in. Optical Fiber Communication Conference (OSA, 8th Mar. 2020), M4H.6.

C6.   Su, Y., Trappen, M.**, Blaicher, M.**, Koos, C. & Nahm, W. 'A 3D Resolution and Aberration Test Target for Confocal Laser Endomicroscopy'. in. SPIE BiOS within Photonics West. **11229** (International Society for Optics and Photonics, 21st Feb. 2020), 1122919.

C7.   Thiel, M., Tanguy, Y., Lindenmann, N., Tungal, A., Reiner, R.**, Blaicher, M.,** Hoffmann, J., Sauter, T., Niesler, F., Gissibl, T. & Radke, A. 'Two-Photon Grayscale Lithography'. in *Laser 3D Manufacturing VII* Photonics West (International Society for Optics and Photonics, 4th Feb. 2020).

C8.   Freude, W., Harter, T., Ummethala, S., Mühlbrandt, S.**, Blaicher, M.**, Wolf, S., Weber, M., Boes, F., Massler, H., Tessmann, A., Kutuvantavida, Y., Kemal, J. N., Nellen, S., Hahn, L., Globisch, B., Walther, M., Zwick, T., Randel, S. & Koos, C. 'Wireless Terahertz Communications'. in. Conference on Lasers and Electro-Optics Europe European Quantum Electronics Conference (CLEO/Europe-EQEC) (IEEE, June 2019).

C9. Hoose, T., **Blaicher, M.**, Kemal, J. N., Zwickel, H., Billah, M. R., Dietrich, P.-I., Hofmann, A., Freude, W., Randel, S. & Koos, C. 'Hardwired Configurable Photonic Integrated Circuits Enabled by 3D Nanoprinting'. in. European Conference on Optical Communication (ECOC) (IEEE, Rome, Sept. 2018).

C10. Koos, C., Freude, W., Randel, S., Billah, M. R., **Blaicher, M.**, Dietrich, P.-I., Hoose, T., Xu, Y., Kemal, J. N., Nesic, A. & Hofmann, A. 'Photonic Wire Bonding and 3D Nanoprinting in Photonic Integration – from Lab Demonstrations to Production'. in. European Conference on Optical Communication (ECOC) (IEEE, Sept. 2018).

C11. Trappen, M., **Blaicher, M.**, Dietrich, P.-I., Hoose, T., Xu, Y., Billah, M. R., Freude, W. & Koos, C. '3D-Printed Optics for Wafer-Scale Probing'. in. European Conference on Optical Communication (ECOC) (IEEE, Rome, Sept. 2018).

C12. Harter, T., Ummethala, S., Mühlbrandt, S., **Blaicher, M.**, Köhnle, K., Adib, M. M. H., Weber, M., Wolf, S., Kutuvantavida, Y., Kemal, J. N., Nellen, S., Hahn, L., Tessmann, A., Walther, M., Zwick, T., Randel, S., Freude, W. & Koos, C. 'Wireless Terahertz Communications Using Optoelectronic Techniques'. in *Progress in Electromagnetic Research Symposium (PIERS), 2018* (IEEE, Toyama, Aug. 2018).

C13. Koos, C., Freude, W., Randel, S., Dietrich, P.-I., **Blaicher, M.**, Xu, Y., Billah, M. R., Hoose, T., Trappen, M. & Hofmann, A. 'Efficient Coupling Interfaces in Photonic Systems Enabled by Printed Freeform Micro-Optics'. in. 20th International Conference on Transparent Optical Networks (ICTON) (IEEE, Bucharest, July 2018).

C14.   Koos, C., Randel, S., Freude, W., Dalton, L. R., Wolf, S., Kieninger, C., Ku-
        tuvantavida, Y., Lauerrnann, M., Elder, D. L., Mühlbrandt, S., Zwickel,
        H., Melikyan, A., Harter, T., Ummethala, S., Billah, M. R., **Blaicher,
        M.**, Dietrich, P.-I. & Hoose, T. 'Hybrid Photonic Integration and Plas-
        monic Devices: New Perspectives for High-Speed Communications and
        Ultra-Fast Signal Processing'. in. Conference on Lasers and Electro-Optics
        Pacific Rim (CLEO-PR) (IEEE, Hong Kong, July 2018).

C15.   Hottinger, P., Harris, R. J., Dietrich, P.-I., **Blaicher, M.**, Glück, M.,
        Bechter, A., Crass, J., Pott, J.-U., Koos, C., Sawodny, O. & Quirrenbach,
        A. 'Micro-Lens Arrays as Tip-Tilt Sensor for Single Mode Fiber Coupling'.
        in. SPIE Astronomical Telescopes + Instrumentation. **10706** (Interna-
        tional Society for Optics and Photonics, 10th July 2018), 1070629.

C16.   **Blaicher, M.**, Billah, M. R., Hoose, T., Dietrich, P.-I., Hofmann, A.,
        Randel, S., Freude, W. & Koos, C. '3D-Printed Ultra-Broadband Highly
        Efficient Out-of-Plane Coupler for Photonic Integrated Circuits'. in.
        Conference on Lasers and Electro-Optics (CLEO) (OSA, May 2018),
        STh1A.1.

C17.   Daria Kohler, Wondimu, S. F., Hahn, L., Allegro, I., **Blaicher, M.**, Freude,
        W. & Koos, C. 'Lasing in Si_3N_4-Organic Hybrid (SiNOH) Spiral Reson-
        ators'. in. Conference on Lasers and Electro-Optics (Optical Society of
        America, 13th May 2018), SM4I.6.

C18.   Billah[†], M. R., **Blaicher[†], M.**, Kemal, J. N., Hoose, T., Zwickel, H., Diet-
        rich, P.-I., Troppenz, U., Möhrle, M., Merget, F., Hofmann, A., Witzens,
        J., Randel, S., Freude, W. & Koos, C. '8-Channel 448 Gbit/s Silicon
        Photonic Transmitter Enabled by Photonic Wire Bonding'. in *Postdead-
        line Papers* Optical Fiber Communication Conference (OFC) (OSA,
        2017), Th5D.6.

C19.   Harter, T., Adib, M. M. H., Wolf, S., Mühlbrandt, S., Weber, M**., Blaicher, M.**, Bös, F., Massler, H., Tessmann, A., Nellen, S., Göbel, T., Giesekus, J., Walther, M., Zwick, T., Freude, W., Randel, S. & Koos, C. 'Wireless Multi-Subcarrier THz Communications Using Mixing in a Photoconductor for Coherent Reception'. in. IEEE Photonics Conference (IPC) (IEEE, Oct. 2017), 147–148.

C20.   Koos, C., Freude, W., Randel, S., Billah, M**., Blaicher, M.**, Hoose, T., Dietrich, P., Nesic, A. & Hofmann, A. 'Hybrid Photonic Multi-Chip Integration Enabled by 3D Nano-Printing'. in. IEEE Photonics Conference (IPC) Part II (IEEE, Orlando, Oct. 2017).

C21.   Billah, M. R., Kemal, J. N., Marin-Palomo, P**., Blaicher, M.**, Kutuvantavida, Y., Kieninger, C., Zwickel, H., Dietrich, P.-I., Wolf, S., Hoose, T., Xu, Y., Troppenz, U., Möhrle, M., Randel, S., Freude, W. & Koos, C. 'Four-Channel 784 Gbit/s Transmitter Module Enabled by Photonic Wire Bonding and Silicon-Organic Hybrid Modulators'. in *Postdeadline Papers* European Conference on Optical Communication (ECOC) (IEEE, Gothenburg, Sept. 2017).

C22.   Dietrich, P.-I., Reuter, I**., Blaicher, M.**, Schneider, S., Billah, M. R., Hoose, T., Hofmann, A., Caer, C., Dangel, R., Offrein, B., Möhrle, M., Troppenz, U., Zander, M., Freude, W. & Koos, C. 'Lenses for Low-Loss Chip-to-Fiber and Fiber-to-Fiber Coupling Fabricated by 3D Direct-Write Lithography'. in. Conference on Lasers and Electro-Optics (CLEO) (OSA, 2016), SM1G.4.

C23.   Hoose, T., Billah, M., Marin, P**., Blaicher, M.**, Dietrich, P. I., Hofmann, A., Troppenz, U., Möhrle, M., Lindenmann, N., Thiel, M., Simon, P., Hoffmann, J., Goedecke, M. L., Freude, W. & Koos, C. 'Multi-Chip Integration by Photonic Wire Bonding: Connecting Surface and Edge Emitting Lasers to Silicon Chips'. in. Optical Fiber Communication Conference (OFC) (OSA, 2016), M2I.7.

C24.   Nesic, A., **Blaicher, M.**, Hoose, T., Lauermann, M., Kutuvantavida, Y., Freude, W. & Koos, C. 'Hybrid 2D/3D Photonic Integration for Non-Planar Circuit Topologies'. in. 42nd European Conference on Optical Communication (ECOC) (Düsseldorf, Sept. 2016).

C25.   Dietrich, P., Wondimu, S., Wienhold, T., Steidle, M., Hofmann, A., Lindenmann, N., Billah, M. R., Hoose, T., **Blaicher, M.**, Freude, W. & Koos, C. 'Herstellung Mikrooptischer Komponenten Durch Zwei-Photonen-Polymerisation'. in. MikroSystemTechnik-Kongress „Von Bauelementen Zu Systemen" (26th Nov. 2015).

C26.   **Blaicher, M.**, Billah, M. R., Hoose, T., Hofmann, A., Freude, W. & Koos, C. 'Multi-Chip Integration by Photonic Wire Bonding'. in. 634. WE-Heraeus-Seminar "Merging Micro- and Nano-Optics: 3D Printing for Advanced and Functional Optics" (Bad Honnef, 9th Jan. 17), (best poster price).

G.3 Patents

The following list only includes published patents. At the time of publication, there are at least three unpublished patent applications.

P1.   **Blaicher, M.**, Nesic, A., Maier, P., Hofmann, A., Xu, Y. & Koos, C. *German Pat.* 102020212112A1 (2022).

P2.   Nesic, A., **Blaicher, M.** & Koos, C. *German Pat.* 102020204641A1 (2021).

P3.   **Blaicher, M.**, Dietrich, P.-I. & Koos, C. *Pat.* WO2021175967A1 (WO) (2021).

P4.   Dietrich, P.-I., Goering, G., **Blaicher, M.**, Trappen, M., Hölscher, H. & Koos, C. *German Pat.* 102017221952B3 (2019).

P5.   Dietrich, P.-I., Koos, C., **Blaicher, M.** & Reuter, I. *Pat.* WO2018083191A1 (WO) (2018).

P6.   Koos, C., Hoose, T., Dietrich, P.-I., **Blaicher, M.**, Gödecke, M. L. & Lindenmann, N. *Pat.* WO2018024872A1 (WO) (2018).

P7.   **Blaicher, M.**, Pernice, W. & Wegener, M. *U.S. Pat.* 9678278B2 (2017).

Appendix H

Bibliography

1. *Cisco Visual Networking Index: Forecast and Trends, 2017- 2022, (White Paper)* (Cisco, 2019).

2. Pavarelli, N. *et al.* 'Optical and Electronic Packaging Processes for Silicon Photonic Systems'. *Journal of Lightwave Technology* **33,** 991–997 (1st Mar. 2015).

3. Lindenmann, N. *et al.* 'Connecting Silicon Photonic Circuits to Multicore Fibers by Photonic Wire Bonding'. *Journal of Lightwave Technology* **33,** 755–760 (15th Feb. 2015).

4. Hoose, T. *et al.* 'Multi-Chip Integration by Photonic Wire Bonding: Connecting Surface and Edge Emitting Lasers to Silicon Chips'. in. Optical Fiber Communication Conference (OFC) (OSA, 2016), M2I.7.

5. Blaicher, M. *et al.* 'Hybrid Multi-Chip Assembly of Optical Communication Engines by in Situ 3D Nano-Lithography'. *Light: Science & Applications* **9,** 71 (27th Apr. 2020).

6. Blaicher, M. *et al.* '3D-Printed Ultra-Broadband Highly Efficient Out-of-Plane Coupler for Photonic Integrated Circuits'. in. Conference on Lasers and Electro-Optics (CLEO) (OSA, May 2018), STh1A.1.

7. Nesic, A., Blaicher, M., Pablo Marin-Palomo, Freude, W. & Koos, C. 'Ultra-Broadband Polarization Beam Splitter and Rotator Based on 3D-printed Waveguides'. *(submitted)* (9th June 2021).

8. Yu, H. *et al.* '400Gbps Fully Integrated DR4 Silicon Photonics Transmitter for Data Center Applications'. in. Optical Fiber Communication Conference (OFC) (OSA, 8th Mar. 2020), T3H.6.

9. Wörhoff, K., Heideman, R. G., Leinse, A. & Hoekman, M. 'TriPleX: A Versatile Dielectric Photonic Platform'. *Advanced Optical Technologies* **4,** 189–207 (1st Apr. 2015).

10. Rahim, A. *et al.* 'Expanding the Silicon Photonics Portfolio With Silicon Nitride Photonic Integrated Circuits'. *Journal of Lightwave Technology* **35,** 639–649 (15th Feb. 2017).

11. Desiatov, B., Shams-Ansari, A., Zhang, M., Wang, C. & Lončar, M. 'Ultra-Low-Loss Integrated Visible Photonics Using Thin-Film Lithium Niobate'. *Optica* **6,** 380–384 (20th Mar. 2019).

12. Rath, P., Khasminskaya, S., Nebel, C., Wild, C. & Pernice, W. H. P. 'Diamond-Integrated Optomechanical Circuits'. *Nature Communications* **4,** 1690 (1 9th Apr. 2013).

13. Carroll, L. *et al.* 'Photonic Packaging: Transforming Silicon Photonic Integrated Circuits into Photonic Devices'. *Applied Sciences* **6,** 426 (15th Dec. 2016).

14. Shubin, I. *et al.* 'Alignment and Integration of a Hybrid, External-Cavity InP-SOI Laser'. in. Optical Fiber Communication Conference (OSA, 20th Mar. 2016), M2C.2.

15. Marchetti, R., Lacava, C., Carroll, L., Gradkowski, K. & Minzioni, P. 'Coupling Strategies for Silicon Photonics Integrated Chip'. *Photonics Research* **7,** 201–239 (1st Feb. 2019).

16. Fuchs, E., Bruce, E., Ram, R. & Kirchain, R. 'Process-Based Cost Modeling of Photonics Manufacture: The Cost Competitiveness of Monolithic Integration of a 1550-Nm DFB Laser and an Electroabsorptive Modulator on an InP Platform'. *Journal of Lightwave Technology* **24,** 3175–3186 (7th Aug. 2006).

17. Thiel, M., Rill, M. S., Freymann, G. von & Wegener, M. 'Three-Dimensional Bi-Chiral Photonic Crystals'. *Advanced Materials* **21,** 4680–4682 (2009).

18. Dietrich, P.-I. *et al.* 'In Situ 3D Nanoprinting of Free-Form Coupling Elements for Hybrid Photonic Integration'. *Nature Photonics* **12,** 241–247 (26th Apr. 2018).

19. Gissibl, T., Thiele, S., Herkommer, A. & Giessen, H. 'Two-Photon Direct Laser Writing of Ultracompact Multi-Lens Objectives'. *Nature Photonics* **10,** 554–560 (27th Aug. 2016).

20. Schmidt, S. *et al.* 'Wave-Optical Modeling beyond the Thin-Element-Approximation'. *Optics Express* **24,** 30188 (26th Dec. 2016).

21. He, C. *et al.* 'Chiral Metalens of Circular Polarization Dichroism with Helical Surface Arrays in Mid-Infrared Region'. *Advanced Optical Materials* **7,** 1901129 (19th Sept. 2019).

22. Hao, C. *et al.* 'Single-Layer Aberration-Compensated Flat Lens for Robust Wide-Angle Imaging'. *Laser & Photonics Reviews* **14,** 2000017 (27th Apr. 2020).

23. Thompson, J. R. *et al.* 'Two-Photon Polymerized Poly(Caprolactone) Retinal Cell Delivery Scaffolds and Their Systemic and Retinal Biocompatibility'. *Acta Biomaterialia* **94,** 204–218 (1st Aug. 2019).

24. Koepele, C. A., Guix, M., Bi, C., Adam, G. & Cappelleri, D. J. '3D-Printed Microrobots with Integrated Structural Color for Identification and Tracking'. *Advanced Intelligent Systems* **2,** 1900147 (5th Mar. 2020).

25. Striggow, F. *et al.* 'Sperm-Driven Micromotors Moving in Oviduct Fluid and Viscoelastic Media'. *Small* **16,** 2000213 (19th May 2020).

26. Thiele, S., Arzenbacher, K., Gissibl, T., Giessen, H. & Herkommer, A. M. '3D-printed Eagle Eye: Compound Microlens System for Foveated Imaging'. *Science Advances* **3,** e1602655 (1st Feb. 2017).

27. Weber, K., Wang, Z., Thiele, S., Herkommer, A. & Giessen, H. 'Distortion-Free Multi-Element Hypergon Wide-Angle Micro-Objective Obtained by Femtosecond 3D Printing'. *Optics Letters* **45,** 2784–2787 (15th May 2020).

28. Göppert-Mayer, M. 'Über Elementarakte mit zwei Quantensprüngen'. *Annalen der Physik* **401,** 273–294 (1931).

29. Kaiser, W. & Garrett, C. 'Two-Photon Excitation in Two-Photon Excitation in CaF_2: Eu^{2+}'. *Physical Review Letters* **7,** 229–231 (15th Sept. 1961).

30. Freund, I. & Deutsch, M. 'Second-Harmonic Microscopy of Biological Tissue'. *Optics Letters* **11,** 94 (Feb. 1986).

31. Zipfel, W. R., Williams, R. M. & Webb, W. W. 'Nonlinear Magic: Multiphoton Microscopy in the Biosciences'. *Nature Biotechnology* **21,** 1369–1377. pmid: 14595365 (31st Oct. 2003).

32. Maruo, S., Nakamura, O. & Kawata, S. 'Three-Dimensional Microfabrication with Two-Photon-Absorbed Photopolymerization'. *Optics Letters* **22,** 132–134 (15th Jan. 1997).

33. Malinauskas, M. *et al.* 'Ultrafast Laser Processing of Materials: From Science to Industry'. *Light: Science & Applications* **5,** e16133. pmid: 28636993 (14th Aug. 2016).

34. Teh, W. H., Dürig, U., Drechsler, U., Smith, C. G. & Güntherodt, H.-J. 'Effect of Low Numerical-Aperture Femtosecond Two-Photon Absorption on (SU-8) Resist for Ultrahigh-Aspect-Ratio Microstereolithography'. *Journal of Applied Physics* **97,** 054907 (15th Feb. 2005).

35. Quick, A. S. *et al.* 'Preparation of Reactive Three-Dimensional Microstructures via Direct Laser Writing and Thiol-ene Chemistry'. *Macromolecular Rapid Communications* **34,** 335–340 (2013).

36. Fischer, J. *et al.* 'Three-Dimensional Multi-Photon Direct Laser Writing with Variable Repetition Rate'. *Optics Express* **21,** 26244–26260 (4th Nov. 2013).

37. Decker, C. 'Photoinitiated Curing of Multifunctional Monomers'. *Acta Polymerica* **45,** 333–347 (1994).

38. Park, J.-W. *et al.* 'Characteristic Shrinkage Evaluation of Photocurable Materials'. *Polymer Testing* **56,** 344–353 (1st Dec. 2016).

39. LaFratta, C. N. & Baldacchini, T. 'Two-Photon Polymerization Metrology: Characterization Methods of Mechanisms and Microstructures'. *Micromachines* **8,** 101 (4 Apr. 2017).

40. Mueller, J. B., Fischer, J., Mayer, F., Kadic, M. & Wegener, M. 'Polymerization Kinetics in Three-Dimensional Direct Laser Writing'. *Advanced Materials* **26,** 6566–6571 (2014).

41. Fischer, J. & Wegener, M. 'Three-Dimensional Optical Laser Lithography beyond the Diffraction Limit'. *Laser and Photonics Reviews* **7,** 22–44 (2013).

42. Sparrow, C. M. 'On Spectroscopic Resolving Power'. *The Astrophysical Journal* **44,** 76 (1st Sept. 1916).

43. Nes, A. S. van de, Billy, L., Pereira, S. F. & Braat, J. J. M. 'Calculation of the Vectorial Field Distribution in a Stratified Focal Region of a High Numerical Aperture Imaging System'. *Optics Express* **12,** 1281–1293 (5th Apr. 2004).

44. Tičkūnas, T., Purlys, V. & Gadonas, R. 'Axial Resolution Improvement in Multiphoton Polymerization by 4Pi Excitation'. in *Laser 3D Manufacturing VI* Laser 3D Manufacturing VI. **10909** (International Society for Optics and Photonics, 4th Mar. 2019), 1090903.

45. Jayne, R. K., Stark, T. J., Reeves, J. B., Bishop, D. J. & White, A. E. 'Dynamic Actuation of Soft 3D Micromechanical Structures Using Micro-Electromechanical Systems (MEMS)'. *Advanced Materials Technologies* **3,** 1700293 (Mar. 2018).

46. Schumann, M., Bückmann, T., Gruhler, N., Wegener, M. & Pernice, W. 'Hybrid 2D-3D Optical Devices for Integrated Optics by Direct Laser Writing'. *Light: Science & Applications* **3,** e175 (6th June 2014).

47. Davidovits, P. & Egger, M. D. 'Scanning Laser Microscope'. *Nature* **223,** 831–831 (5208 Aug. 1969).

48. Smith, J. L. 'The Inverted Microscope; (a New Form of Microscope.) With the Description of a New Eye-Piece Micrometer, and a New Form of Goniometer for Measuring the Angles of Crystals under the Microscope.' *American Journal of Science and Arts. Second* **14,** 233–241 (Nov. 1852).

49. Negrean, A. & Mansvelder, H. D. 'Optimal Lens Design and Use in Laser-Scanning Microscopy'. *Biomedical Optics Express* **5,** 1588–1609 (1st May 2014).

50. Billah, M. R. *et al.* 'Hybrid Integration of Silicon Photonics Circuits and InP Lasers by Photonic Wire Bonding'. *Optica* **5,** 876 (20th July 2018).

51. Nesic, A. *et al.* 'Photonic-Integrated Circuits with Non-Planar Topologies Realized by 3D-printed Waveguide Overpasses'. *Optics Express* **27,** 17402–17425 (10th June 2019).

52. Helge Gehring, Blaicher, M., Grottke, T. & Pernice, W. 'Reconfigurable Nanophotonic Circuitry Enabled by Direct-Laser-Writing'. *IEEE Journal of Selected Topics in Quantum Electronics* **26,** 4400905 (25th June 2020).

53. Hoose, T. *et al. Hardwire-Configurable Photonic Integrated Circuits Enabled by 3D Nano-Printing*. 19th Dec. 2019. arXiv: 1912.09942 [physics].

54. Blaicher, M., Pernice, W. & Wegener, M. *U.S. Pat.* 9678278B2 (2017).

55. Gehring, H. *et al.* 'Low-Loss Fiber-to-Chip Couplers with Ultrawide Optical Bandwidth'. *APL Photonics* **4,** 010801 (1st Jan. 2019).

56. Luo, H. *et al.* 'Low-Loss and Broadband Fiber-to-Chip Coupler by 3D Fabrication on a Silicon Photonic Platform'. *Optics Letters* **45,** 1236–1239 (1st Mar. 2020).

57. Koos, C. *et al.* *Photonische Wirebonds für optische Multi-Chip-Systeme - Phoibos.* Final project report (Karlsruher Institut für Technologie (KIT), Karlsruhe, 2016).

58. Darcie, A. *et al.* 'SiEPICfab: The Canadian Silicon Photonics Rapid-Prototyping Foundry for Integrated Optics and Quantum Computing'. in *Silicon Photonics XVI* Silicon Photonics XVI. **11691** (International Society for Optics and Photonics, 5th Mar. 2021), 116910C.

59. Krause, M. 'Finite-Difference Mode Solver for Curved Waveguides With Angled and Curved Dielectric Interfaces'. *Journal of Lightwave Technology* **29,** 691–699 (Mar. 2011).

60. Dottermusch, S., Busko, D., Langenhorst, M., Paetzold, U. W. & Richards, B. S. 'Exposure-Dependent Refractive Index of Nanoscribe IP-Dip Photoresist Layers'. *Optics Letters* **44,** 29 (17th Dec. 2018).

61. Zvagelsky, R. D. *et al.* 'Three-Dimensional Polymer Wire Bonds on a Chip: Morphology and Functionality'. *Journal of Physics D: Applied Physics* **53,** 355102 (June 2020).

62. Gao, H. *et al.* 'High-Resolution 3D Printed Photonic Waveguide Devices'. *Advanced Optical Materials* **8,** 2000613 (2020).

63. Darcie, A. *et al.* 'SiEPICfab: The Canadian Silicon Photonics Rapid-Prototyping Foundry for Integrated Optics and Quantum Computing'. in *Silicon Photonics XVI* Silicon Photonics XVI. **11691** (International Society for Optics and Photonics, 5th Mar. 2021), 116910C.

64. Müller, P. *et al.* 'STED-Inspired Laser Lithography Based on Photoswitchable Spirothiopyran Moieties'. *Chemistry of Materials* **31,** 1966–1972 (26th Mar. 2019).

65. De Boor, C. 'On Calculating with B-splines'. *Journal of Approximation Theory* **6,** 50–62 (1st July 1972).

66. Lindenmann, N. *Photonic Wire Bonding as a Novel Technology for Photonic Chip Interfaces / by Nicole Lindenmann* (Karlsruhe Institute of Technology, Karlsruhe, 2018). 222 pp.

67. Wang, W., Jüttler, B., Zheng, D. & Liu, Y. 'Computation of Rotation Minimizing Frames'. *ACM Transactions on Graphics* **27,** 2:1–2:18 (20th Mar. 2008).

68. Khan, M. U., Xing, Y., Ye, Y. & Bogaerts, W. 'Photonic Integrated Circuit Design in a Foundry+Fabless Ecosystem'. *IEEE Journal of Selected Topics in Quantum Electronics* **25,** 1–14 (Sept. 2019).

69. Lindenmann, N. *et al.* 'Photonic Wire Bonding: A Novel Concept for Chip-Scale Interconnects'. *Optics Express* **20,** 17667–17677 (30th July 2012).

70. Singh, P., Harbola, M. K. & Johnson, D. D. 'Better Band Gaps for Wide-Gap Semiconductors from a Locally Corrected Exchange-Correlation Potential That Nearly Eliminates Self-Interaction Errors'. *Journal of Physics: Condensed Matter* **29,** 424001 (Sept. 2017).

71. *CST Studio Suite 3D EM Simulation and Analysis Software.* https://www.3ds.com/products-services/simulia/products/cst-studio-suite/ (2020).

72. Hornberg, A. & Martin, R. 'Propagation of Gaussian Beams'. *Laser Technik Journal* **2,** 75–80 (12th Feb. 2007).

73. Brenner, K.-H. & Singer, W. 'Light Propagation through Microlenses: A New Simulation Method'. *Applied Optics* **32,** 4984–4988 (10th Sept. 1993).

74. Fertig, M. & Brenner, K.-H. 'Vector Wave Propagation Method'. *JOSA A* **27,** 709–717 (1st Apr. 2010).

75. Schmidt, S. *et al.* 'Wave-Optical Modeling beyond the Thin-Element-Approximation'. *Optics Express* **24,** 30188 (2016).

76. Schmidt, S. *Efficient Wave-Optical Simulations for Themodeling of Micro-Optical Elements.* PhD thesis (Jena, 28th June 2018).

77. Moreland, K. & Angel, E. 'The FFT on a GPU'. in *Proceedings of the ACM SIGGRAPH/EUROGRAPHICS Conference on Graphics Hardware* (2003), 112–119.

78. Malcolm, J. *et al.* 'ArrayFire: A GPU Acceleration Platform'. in *Modeling and Simulation for Defense Systems and Applications VII* Modeling and Simulation for Defense Systems and Applications VII. **8403** (International Society for Optics and Photonics, 4th May 2012), 84030A.

79. Sibson, P. *et al.* 'Integrated Silicon Photonics for High-Speed Quantum Key Distribution'. *Optica* **4,** 172–177 (20th Feb. 2017).

80. Nagatsuma, T., Ducournau, G. & Renaud, C. C. 'Advances in Terahertz Communications Accelerated by Photonics'. *Nature Photonics* **10,** 371–379. pmid: 23938796 (1st June 2016).

81. Trocha, P. *et al.* 'Ultrafast Optical Ranging Using Microresonator Soliton Frequency Combs'. *Science* **359,** 887–891. pmid: 29472477 (23rd Feb. 2018).

82. Münzberg, J. *et al.* 'Superconducting Nanowire Single-Photon Detector Implemented in a 2D Photonic Crystal Cavity'. *Optica* **5,** 658–665 (20th May 2018).

83. Wang, J. *et al.* 'Multidimensional Quantum Entanglement with Large-Scale Integrated Optics'. *Science* **360,** 285–291. pmid: 29519918 (20th Apr. 2018).

84. Hatori, N. *et al.* 'A Hybrid Integrated Light Source on a Silicon Platform Using a Trident Spot-Size Converter'. *Journal of Lightwave Technology* **32,** 1329–1336 (Apr. 2014).

85. Snyder, B., Corbett, B. & O'Brien, P. 'Hybrid Integration of the Wavelength-Tunable Laser With a Silicon Photonic Integrated Circuit'. *Journal of Lightwave Technology* **31,** 3934–3942 (Dec. 2013).

86. O'Brien, P., Carrol, L., Eason, C. & Lee, J. S. in *Silicon Photonics III.* (eds Pavesi, L. & Lockwood, D. J.) 217–236 (Springer, Berlin, Heidelberg, 2016).

87. Van der Tol, J. J. G. M., Oei, Y. S., Khalique, U., Nötzel, R. & Smit, M. K. 'InP-based Photonic Circuits: Comparison of Monolithic Integration Techniques'. *Progress in Quantum Electronics* **34,** 135–172 (July 2010).

88. Atabaki, A. H. *et al.* 'Integrating Photonics with Silicon Nanoelectronics for the next Generation of Systems on a Chip'. *Nature* **556,** 349–354 (18th Apr. 2018).

89. Mordor Intelligence. *Photonic Integrated Circuit Market - Growth, Trends, and Forecast* (2018).

90. Billah, M. R. *et al.* '8-Channel 448 Gbit/s Silicon Photonic Transmitter Enabled by Photonic Wire Bonding'. in *Postdeadline Papers* Optical Fiber Communication Conference (OFC) (OSA, 2017), Th5D.6.

91. Billah, M. R. *et al.* 'Four-Channel 784 Gbit/s Transmitter Module Enabled by Photonic Wire Bonding and Silicon-Organic Hybrid Modulators'. in *Postdeadline Papers* European Conference on Optical Communication (ECOC) (IEEE, Gothenburg, Sept. 2017).

92. Möhrle, M. *et al.* 'Ultra-Low Threshold 1490 nm Surface-Emitting BH-DFB Laser Diode with Integrated Monitor Photodiode'. in. 22nd International Conference on Indium Phosphide and Related Materials (IPRM) (IEEE, Kagawa, May 2010).

93. Telcordia. *GR-468-CORE: Reliability Assurance for Optoelectronic Devices.* 2004.

94. Moscoso-Mártir, A. *et al.* 'Silicon Photonics Transmitter with SOA and Semiconductor Mode-Locked Laser'. *Scientific Reports* **7,** 13857 (24th Dec. 2017).

95. Chang, F., Onohara, K. & Mizuochi, T. 'Forward Error Correction for 100 G Transport Networks'. *IEEE Communications Magazine* **48,** 48–55 (2010).

96. IEEE. *IEEE P802.3bs.* 2018.

97. CWDM8 MSA Group. *400G CWDM8 MSA 2 Km Optical Interface Technical Specifications.* 2018.

98. Wolf, S. *et al.* 'Silicon-Organic Hybrid (SOH) Mach-Zehnder Modulators for 100 Gbit/s on-off Keying'. *Scientific Reports* **8,** 2598 (3rd Dec. 2018).

99. Zwickel, H. *et al.* 'Silicon-Organic Hybrid (SOH) Modulators for Intensity-Modulation / Direct-Detection Links with Line Rates of up to 120 Gbit/s'. *Optics Express* **25,** 23784 (2nd Oct. 2017).

100. Lauermann, M. *et al.* 'Low-Power Silicon-Organic Hybrid (SOH) Modulators for Advanced Modulation Formats'. *Optics Express* **22,** 29927 (1st Dec. 2014).

101. Koos, C. *et al.* 'Silicon-Organic Hybrid (SOH) and Plasmonic-Organic Hybrid (POH) Integration'. *Journal of Lightwave Technology* **34,** 256–268 (15th Jan. 2016).

102. Clemens Kieninger *et al.* 'Ultra-High Electro-Optic Activity Demonstrated in a Silicon-Organic Hybrid Modulator'. *Optica* **5,** 739 (20th June 2018).

103. Absil, P. P. *et al.* 'Imec iSiPP25G Silicon Photonics: A Robust CMOS-based Photonics Technology Platform'. in. SPIE OPTO (eds Reed, G. T. & Watts, M. R.) (San Francisco, 27th Feb. 2015), 93670V.

104. International Telecommunication Union - ITU-T. *Forward Error Correction for High Bit-Rate DWDM Submarine Systems.* 2005.

105. Contestabile, G. *et al.* 'InP Monolithically Integrated Coherent Transmitter'. *Optics Express* **23,** 10741 (20th Apr. 2015).

106. Lange, S. *et al.* '100 GBd Intensity Modulation and Direct Detection With an InP-Based Monolithic DFB Laser Mach–Zehnder Modulator'. *Journal of Lightwave Technology* **36,** 97–102 (1st Jan. 2018).

107. Jonušauskas, L. *et al.* 'Mesoscale Laser 3D Printing'. *Optics Express* **27,** 15205 (27th May 2019).

108. Kawata, S., Sun, H.-B., Tanaka, T. & Takada, K. 'Finer Features for Functional Microdevices'. *Nature* **412,** 697–698 (6848 Aug. 2001).

109. Deubel, M. *et al.* 'Direct Laser Writing of Three-Dimensional Photonic-Crystal Templates for Telecommunications'. *Nature Materials* **3,** 444–447 (7 13th June 2004).

110. Carroll, L. *et al.* 'Photonic Packaging: Transforming Silicon Photonic Integrated Circuits into Photonic Devices'. *Applied Sciences* **6,** 426 (12 Dec. 2016).

111. Dai, D. & Bowers, J. E. 'Novel Ultra-Short and Ultra-Broadband Polarization Beam Splitter Based on a Bent Directional Coupler'. *Optics Express* **19,** 18614 (12th Sept. 2011).

112. Lu, Z., Wang, Y., Zhang, F., Jaeger, N. A. F. & Chrostowski, L. 'Wideband Silicon Photonic Polarization Beamsplitter Based on Point-Symmetric Cascaded Broadband Couplers'. *Optics Express* **23,** 29413–29422 (16th Nov. 2015).

113. Kim, D. W., Lee, M. H., Kim, Y. & Kim, K. H. 'Planar-Type Polarization Beam Splitter Based on a Bridged Silicon Waveguide Coupler'. *Optics Express* **23,** 998 (26th Jan. 2015).

114. Yin, M., Yang, W., Li, Y., Wang, X. & Li, H. 'CMOS-compatible and Fabrication-Tolerant MMI-based Polarization Beam Splitter'. *Optics Communications* **335,** 48–52 (Jan. 2015).

115. Keyvaninia, S. *et al.* 'Highly Efficient Passive InP Polarization Rotator-Splitter'. *Optics Express* **27,** 25872–25881 (2nd Sept. 2019).

116. Sacher, W. D., Barwicz, T., Taylor, B. J. F. & Poon, J. K. S. 'Polarization Rotator-Splitters in Standard Active Silicon Photonics Platforms'. *Optics Express* **22,** 3777–3786 (24th Feb. 2014).

117. Zhang, F. *et al.* 'Ultra-Broadband and Compact Polarizing Beam Splitter in Silicon Photonics'. *OSA Continuum* **3,** 560 (15th Mar. 2020).

118. Watts, M. R., Haus, H. A. & Ippen, E. P. 'Integrated Mode-Evolution-Based Polarization Splitter'. *Optics Letters* **30,** 967 (1st May 2005).

119. Chiles, J., Sjaardema, T., Rao, A. & Fathpour, S. *Topographically Anisotropic Photonics for Broadband Integrated Polarization Diversity.* 19th Feb. 2017. arXiv: 1702.05806 [physics].

120. Shen, B., Wang, P., Polson, R. & Menon, R. 'An Integrated-Nanophotonics Polarization Beamsplitter with $2.4 \times 2.4 \ \mu m^2$ Footprint'. *Nature Photonics* **9,** 378–382 (18th May 2015).

121. Zaoui, W. S., Kunze, A., Vogel, W. & Berroth, M. 'CMOS-Compatible Polarization Splitting Grating Couplers With a Backside Metal Mirror'. *IEEE Photonics Technology Letters* **25,** 1395–1397 (4th June 2013).

122. Hahn, V., Kalt, S., Sridharan, G. M., Wegener, M. & Bhattacharya, S. 'Polarizing Beam Splitter Integrated onto an Optical Fiber Facet'. *Optics Express* **26,** 33148–33157 (10th Dec. 2018).

123. Bertoncini, A., Liberale, C. & Liberale, C. '3D Printed Waveguides Based on Photonic Crystal Fiber Designs for Complex Fiber-End Photonic Devices'. *Optica* **7,** 1487–1494 (20th Nov. 2020).

124. Billah, M. R. *et al.* 'Hybrid Integration of Silicon Photonics Circuits and InP Lasers by Photonic Wire Bonding'. *Optica* **5,** 876–883 (20th July 2018).

125. Dong, P., Chen, Y.-K., Duan, G.-H. & Neilson, D. T. 'Silicon Photonic Devices and Integrated Circuits'. *Nanophotonics* **3,** 215–228 (1st Aug. 2014).

126. Barwicz, T. *et al.* 'Polarization-Transparent Microphotonic Devices in the Strong Confinement Limit'. *Nature Photonics* **1,** 57–60 (21st Dec. 2006).

127. Wang, Z. *et al.* 'Silicon Photonic Integrated Circuit Swept-Source Optical Coherence Tomography Receiver with Dual Polarization, Dual Balanced, in-Phase and Quadrature Detection'. *Biomedical Optics Express* **6,** 2562–2574 (1st July 2015).

128. Babinec, T. M. *et al.* 'A Diamond Nanowire Single-Photon Source'. *Nature Nanotechnology* **5,** 195–199 (3 14th Feb. 2010).

129. Raybon, G. *et al.* 'All-ETDM 80-Gbaud (640-Gb/s) PDM 16-QAM Generation and Coherent Detection'. *IEEE Photonics Technology Letters* **24,** 1328–1330 (8th June 2012).

130. Blaicher, M. *Towards Scalable Hybrid 2D-3D Nanophotonic Circuits.* MA thesis (Karlsruhe Institute of Technology, Karlsruhe, 8th Oct. 2014). 135 pp.

131. Taillaert, D. *et al.* 'Grating Couplers for Coupling between Optical Fibers and Nanophotonic Waveguides'. *Japanese Journal of Applied Physics* **45,** 6071–6077. pmid: 240512800004 (8A 4th Aug. 2006).

132. Ding, Y., Peucheret, C. & Ou, H. 'Ultra-High-Efficiency Apodized Grating Coupler Using a Fully Etched Photonic Crystal'. in *Conference on Lasers and Electro-Optics Pacific Rim (CLEO-PR)* **38** (IEEE, June 2013), 1–2. pmid: 23903126.

133. Scheerlinck, S., Schrauwen, J., Taillaert, D., Van Thourhout, D. & Baets, R. 'Efficient, Broadband and Compact Metal Grating Couplers for Silicon-on-Insulator Waveguides'. in *Conference on Lasers and Electro-Optics (CLEO)* **15** (IEEE, May 2007), 1–2. pmid: 19547311.

134. Xiao, Z., Liow, T.-Y., Zhang, J., Shum, P. & Luan, F. 'Bandwidth Analysis of Waveguide Grating Coupler'. *Optics Express* **21,** 5688. pmid: 23482142 (11th Mar. 2013).

135. *Photonic Multi-Chip Integration from Vanguard Automation.* Vanguard Automation. https://www.vanguard-automation.com/ (2020).

136. Blaicher, M., Dietrich, P.-I. & Koos, C. *Pat.* WO2021175967A1 (WO) (2021).

137. Freude, W. *et al.* 'Quality Metrics for Optical Signals: Eye Diagram, Q-factor, OSNR, EVM and BER'. in *14th International Conference on Transparent Optical Networks (ICTON)* (IEEE, July 2012), Mo.B1.5.

138. Proakis, J. *Digital Communications* 4th Editio (McGrawHill, 2000).

139. Watts, M. R. & Haus, H. A. 'Integrated Mode-Evolution-Based Polarization Rotators'. *Optics Letters* **30,** 138 (15th Jan. 2005).

140. Heffner, B. 'Deterministic, Analytically Complete Measurement of Polarization-Dependent Transmission through Optical Devices'. *IEEE Photonics Technology Letters* **4,** 451–454 (May 1992).

141. Saleh, B. E. A. & Teich, M. C. *Fundamentals of Photonics* 2. Edition. 1200 pp. (Wiley-Interscience, Hoboken, N.J, 13th Apr. 2007).

142. *Springer Handbook of Optical Networks* (eds Mukherjee, B., Tomkos, I., Tornatore, M., Winzer, P. & Zhao, Y.) (Springer International Publishing, 2020).

143. Fatadin, I., Ives, D. & Savory, S. J. 'Blind Equalization and Carrier Phase Recovery in a 16-QAM Optical Coherent System'. *Journal of Lightwave Technology* **27,** 3042–3049 (Aug. 2009).

144. Joyce, W. B. & DeLoach, B. C. 'Alignment of Gaussian Beams'. *Applied Optics* **23,** 4187 (1st Dec. 1984).

145. Kogelnik, H. 'Coupling and Conversion Coefficients for Optical Modes'. in *Quasi-Optics* (June 1964), 333.

146. Greivenkamp, J. *Field Guide to Geometrical Optics* (SPIE Press, Bellingham, 2004).